LBL-36632
UC-408

Lawrence Berkeley Laboratory
UNIVERSITY OF CALIFORNIA

STRUCTURAL BIOLOGY DIVISION

Structural and Oxidation State Studies of the Manganese Cluster in the Oxygen Evolving Complex of Photosystem II

W. Liang
(Ph.D. Thesis)

November 1994

Prepared for the U.S. Department of Energy under Contract Number DE-AC03-76SF00098

LBL-36632
UC-408

Structural and Oxidation State Studies of the Manganese Cluster in the Oxygen Evolving Complex of Photosystem II

Wenchuan Liang
Ph.D. Thesis

Department of Chemistry
University of California

and

Structural Biology Division
Lawrence Berkeley Laboratory
University of California
Berkeley, CA 94720

November 1994

This work was supported by the Director, Office of Energy Research, Office of Energy Biosciences Division, of the U.S. Department of Energy under Contract No. DE-AC03-76SF00098.

Abstract

Structural and Oxidation State Studies of the Manganese Cluster in the Oxygen Evolving Complex of Photosystem II

by

Wenchuan Liang

Doctor of Philosophy in Chemistry

University of California at Berkeley

Professor Kenneth Sauer, Chair

X-ray absorption spectroscopy (XAS) was performed on Photosystem II (PSII)-enriched membranes prepared from spinach to explore: 1) the correlation between structure and magnetic spin state of the Mn cluster in the oxygen evolving complex (OEC) in the S_2 state; and 2) the oxidation state changes of the Mn cluster in the flash-induced S-states.

The structure of the Mn cluster in the S_2 state with the $g \approx 4$ electron paramagnetic resonance (EPR) signal (S_2-g4 state) was compared with that in the S_2 state with multiline signal (S_2-MLS state) and the S_1 state . The S_2-g4 state has a higher XAS inflection point energy than that of the S_1 state, indicating the oxidation of Mn in the advance from the S_1 to the S_2-g4 state. Differences in the edge shape and in the extended X-ray absorption fine structure (EXAFS) show that the structure of the Mn cluster in the S_2-g4 state is different from that in the S_2-MLS or the S_1 state. In the S_2-g4 state, the second shell of backscatterers from the Mn absorber contains two Mn-Mn distances of 2.73 Å and 2.85 Å. Very little distance disorder exists in the second shell of the S_1 or S_2-MLS states. The third shell of the S_2-g4 state at about 3.3 Å also contains increased heterogeneity relative to that of the S_2-MLS or the S_1 state.

Various S-states were prepared at room-temperature by saturating, single-turnover flashes. The flash-dependent oscillation in the amplitude of the MLS was used to characterize the S-state composition and to construct "pure" S-state Mn K-edge spectra. The edge position shifts to higher energy by 1.8 eV upon the $S_1 \rightarrow S_2$ transition. We observe a reproducible shift of only ~0.3 eV during the $S_2 \rightarrow S_3$ transition, however. A feature at ~6553.0 eV in the second derivatives of the spectra disappears during the $S_1 \rightarrow S_2$ transition. By contrast, no significant difference of the edge shape between the S_2 and S_3 states is found, which supports the absence of Mn oxidation during the $S_2 \rightarrow S_3$ transition. Both the lower edge energy and the distinctive shape of the S_0-state spectra are suggestive of one Mn(II) in the Mn cluster in the S_0 state.

In memory of my father

Acknowledgments

I am grateful to have the chance to acknowledge those who have helped me and worked with me in the past few years.

I would like to thank Professor Kenneth Sauer and Dr. Melvin Klein who led me into a brand new field and guided me through the transition period. I am lucky to have been granted the most freedom I can imagine by them to pursue my curiosity in all kinds of subjects. I appreciate the incredible patience both of them possess. They always choose to show me, instead of telling me, how to think more and be patient at science or anything else, whenever I go too far or too fast. On the other hand, when the road seems to be blocked, they show me all the trails that I overlook. They have built up a lab with an atmosphere of freedom and respect, in which everyone learns to optimize their performance independently. Inspired by their broad knowledge and immense experience, I have been able to reach out and explore the extremes of my learning ability.

I thank Dr. Melvin Klein, Profs. Kenneth Sauer, John Hearst and Richard Malkin for reading this thesis and for their valuable suggestions.

I am indebted to Dr. Vittal Yachandra for his valuable advice. Because of his encouragement and trust, the activation energy required to start the XAS projects is greatly reduced. Much of the work in this thesis would not have been completed without Vittal's help and support. Besides, our questions are usually answered quickly, because Vittal remembers almost all the details of the XAS and OEC, and is so organized in all related references.

I am happy that I have had a chance to work with lots of generous people who are willing to spend time and effort to work with me. Dr. Vickie DeRose, with her pleasant personality, was a great help for me to start both my research and life in Calvin lab. Prof. Bill Armstrong and Dr. Joel Gohdes were generous to share their space and time with me in Latimer Hall. Dr. David Britt worked with me on the ESEEM project. Captain Matthew J. Latimer has helped me in many ways, especially with his excellent knowledge of XAS. I also thank him for his friendship and patience to answer endless questions ranging from science to slang I spot from TV programs. Mary has also been great in answering all kinds of inquiry a curious foreigner could have. Dennis Kim and Melissa Grush offered great help and also made my starting days in the lab more interesting.

This work would not be completed without the XAS crew. Dr. Holger Dau, Matthew J. Latimer, Dr. Theo Roelofs, and Dr. Vittal Yachandra offered great help on data collection and scientific discussions on the g4 project. It was certainly a nice experience to collaborate with Dr. Theo Roelofs on the flash project. Recent crew members including Rohel Cinco, Joy Andrews, and Dr. Annette Rompel also assisted in data collection on the flash project.

I thank all the past and present group members, including Vittal, Matthew, Martin, Yvonne, Mary, Jana, Theo, Joy, Annette, Henk and Shelly, for sharing their thoughts with me under the blue sky during our "group lunch" outside the Wurster Hall. I thank Dr. Ann McDermott for her encouragement and sharing her experiences as a female scientist with me. Our European postdocs definitely generate a colorful atmosphere in the lab. I enjoy various conversations and lunches with Drs. Annette Rompel, Theo Roelofs, Olaf Burghaus and Holger Dau.

I would like to thank people who have given me spiritual support to finish writing. I thank Drs. Jeff Pelton, Ed Barry and Li-Shar Huang for their encouragement. I thank Susan Torrano for her friendship. Gary Smith is always helpful when I need more space for data analysis in our computer lcbvax.

I am blessed to have mom and Jason with me. I thank them for all their efforts to let me pursue my degree as my first priority without distraction. At this point it is very clear that without their continuous encouragement and support, I would not be writing this thesis.

Abbreviations

AMP	amplifier
ATP	adenosine triphosphate
BBY	PS II-enriched membrane preparation (Berthold et al., 1981)
BSA	bovine serum albumin
Chl	chlorophyll
cps	counts per second
cyt	cytochrome
DCBQ	2,6-dichloro-*p*-benzoquinone
DCMU	3-(3,4-dichlorophenyl)-1,1-dimethylurea
DMSO	dimethyl sulfoxide
EDTA	ethylenediamine tetraacetic acid
EPR	electron paramagnetic resonance
ESEEM	electron spin echo envelope modulation
EXAFS	extended x-ray absorption fine structure
FT	Fourier transform
HEPES	4-(2-hydroxyethyl)-1-piperazineethanesulfonic acid
ICR	incident count rate
kDa	kiloDalton
KM	PSII-enriched membrane preparation (Kuwabara & Murata, 1982)
MES	2-[N-morpholino]ethanesulfonic acid
MLS	multiline EPR signal
NADP	nicotinamide adenine dinucleotide phosphate
NMR	nuclear magnetic resonance

NSLS	National Synchrotron Light Source
OEC	oxygen evolving complex
P_{680}	primary electron donor of Photosystem II
P_{700}	primary electron donor of Photosystem I
Pheo	pheophytin
PC	plastocyanin
PMT	photomultiplier tube
PPBQ	phenyl-*p*-benzoquinone
PSI	Photosystem I
PSII	Photosystem II
Q	plastoquinone
Q_A & Q_B	plastoquinone electron acceptors in the reaction center of PSII
SCA	single-channel analyzer
S_2-g4 state	the S_2 state with the g=4 EPR signal
S_2-MLS state	the S_2 state with the MLS signal
S_2-ann. sample	annealed S_2-g4 sample
SSRL	Stanford Synchrotron Radiation Laboratory
XANES	X-ray absorption near edge structure
XAS	X-ray absorption spectroscopy

Table of Contents

Chapter I. Introduction.

Chapter II. Material and Methods.

Chapter III. Correlation between Structure and Magnetic Spin State of the Mn Cluster in the Oxygen-Evolving Complex of Photosystem II in the S_2 State: Determination by X-ray Absorption Spectroscopy.

Chapter IV. Oxidation State Changes of the Mn Cluster in the Flash-Induced S-states of Photosystem II: Determination by X-ray Absorption Spectroscopy.

Chapter V. Conclusions and Future Work.

Chapter I. Introduction.

I.A General Introduction to Photosynthesis in Green Plants.

Sunlight provides the energy to support all life on the earth. It maintains the earth at a hospitable temperature. Moreover, it is the ultimate source of all biological energy. Photosynthesizing organisms capture and convert sunlight into necessary energy in the form of bonds between carbon molecules that feeds not only themselves but also all the organisms up the food chain. On the earth approximately 2 x 10^{11} tons of carbon are fixed from atmospheric CO_2 by photosynthetic processes each year. Life on earth continues to be dependent on photosynthesis, both for the oxygen and for the carbon-containing fuel molecules produced as a result of photosynthetic reactions. The overall photosynthetic reaction can be written as follows:

$$6CO_2 + 6H_2O \rightarrow 6O_2 + C_6H_{12}O_6 \qquad (1)$$

I.A.1. The Z-Scheme.

Sunlight absorbed by photosynthetic organisms drives electron transfer reactions. In thylakoid membranes of green plants, the initial reactions of photosynthesis are mediated by two distinct pigment-protein complexes called photosystem I (PSI) and photosystem II (PSII). Hill and Bendall first proposed that a cytochrome complex is placed between the two photosystems, and it is reduced when electrons are received from PSII and oxidized when they are passed on to PSI (Hill and Bendall, 1960). This model, in which PSI and PSII work in sequence, is called the Z-scheme. The electron transfer components in the Z-scheme are shown in Fig. I-1. Each

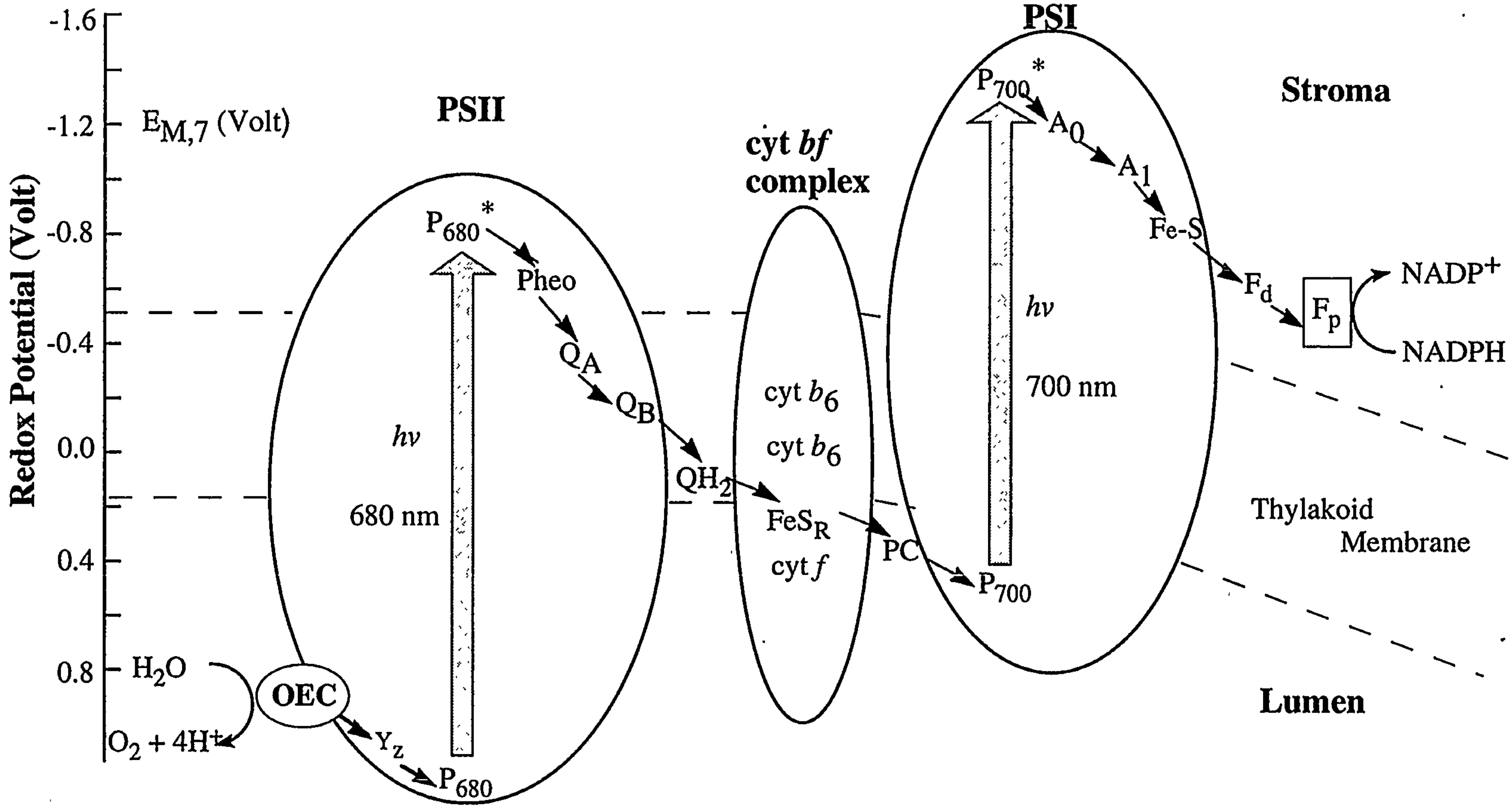

Fig. I-1. The Z-scheme of photosynthetic electron flow from H_2O to $NADP^+$ in higher plants and cyanobacteria. The vertical position of each electron transfer component corresponds to its redox potential at pH 7. PSI, PSII, and cyt *bf* complex are membrane-bound protein complexes and are shown in ovals. Abbreviations used: OEC, oxygen-evolving complex; Y_z, a redox-active tyrosine residue; Pheo, pheophytin; Q, plastoquinone; QH_2, reduced plastoquinone; cyt, cytochrome; FeS_R, Rieske iron sulfur center; PC, plastocyanin; A, acceptors of electrons from P_{700}*; Fd, ferredoxin; $NADP^+$, nicotinamide adenine dinucleotide phosphate; Fp, flavoprotein (ferredoxin-$NADP^+$ oxidoreductase). Adapted from Miller & Brudvig, (1991) *Biochim. Biophys. Acta. 1056*, 1.

photosystem contains from 250 to 400 molecules of chlorophyll, which serve as light-trapping antennae. Photons absorbed by these antenna molecules transfer their excitation energy to a special site (denoted P_{680} and P_{700} for PSII and PSI, respectively) where primary electron transfer reactions occur.

Photosynthesis starts when excitation energy from the light-harvesting antennae arrives at P_{680}. An endergonic charge separation occurs between P_{680} and a pheophytin (Pheo) molecule. Charge recombination of the $P_{680}^{+}\cdot Pheo^{-}$ pair is prevented by the following two reactions: 1) a rapid (250-550 ps, Nuijs et al., 1986; Leibl et al., 1989) electron transfer from $Pheo^{-}$ to a nearby plastoquinone molecule known as Q_A; and 2) the reduction of $P680^{+}$ by a redox-active tyrosine residue (Y_Z) within 40-280 ns (Hoganson et al., 1988; Gerken et al., 1988). Reduced plastoquinone (QH_2) carries electrons from PSII into the cytochrome *bf* complex which then reduces plastocyanin (PC).

Similarly, absorption of light by PSI produces a charge separation pair -- $P_{700}^{+}\cdot A_0^{-}$. P_{700}^{+} obtains an electron from PC and is ready for the next photoreaction. Meanwhile, the electron released following light absorption by P_{700} travels from A_0^{-} through the electron acceptors of PSI to ferredoxin (Fd). The resulting Fd is a strongly reducing species which can donate electrons to $NADP^{+}$ to form NADPH. The electron flow between the two photosystems generates a transmembrane proton gradient that is used to synthesize ATP molecules. The resulting ATP molecules will eventually be used along with NADPH to reduce CO_2 in the Calvin cycle to perform biosynthesis of carbohydrates represented as $C_6H_{12}O_6$ in Eq. (1). At the other charge separation site, PSII produces a very strong oxidant, capable of extracting the electrons from water to evolve molecular oxygen. The oxygen-evolving complex (OEC), the enzyme that facilitates oxidation of water in PSII of green plants, will be discussed in section I.B.

I.A.2. The Polypeptides in PSII.

Our understanding of PSII has benefited greatly from the study of purple non-sulfur bacteria. The three-dimensional structure of the purple bacterial reaction center (Deisenhofer et al., 1984) could be used directly as a model for PSII, both in terms of the polypeptides arrangement and the electron transfer components. Portions of the core complexes (D_1, D_2) have been shown to have significant homology with corresponding portions of the L- and M-subunits of reaction centers from purple bacteria (Hearst, 1986; Michel & Deisenhofer, 1988). In addition to the structural similarities, the kinetics, and the EPR signals of the electron acceptance pathways have been shown to be similar between the bacterial reaction centers and PSII (Okamura et al., 1982; Rutherford, 1987). This resemblance led to a construction of a working model for the polypeptide organization in PSII. Fig. I-2 presents this model together with the related redox components in the Z-scheme. The apparent molecular masses (in kDa) are marked on top of each polypeptide.

The two 32 kDa polypeptides, denoted D_1 and D_2, contain the electron transfer components. These two polypeptides form the photochemical core to perform the light-driven charge separation reaction. CP47 and CP43 are believed to serve as tightly-bond light-harvesting antennae (Bricker, 1990). Oxygen-evolving PSII complexes also contain one or two molecules of cytochrome *b*-559 per reaction center (Buser et al., 1992), although its function is still unknown. An additional chlorophyll-containing polypeptide of 28 kDa is also shown in Fig.I-2. This polypeptide has been reported to be required for Q_B to function normally (Bowlby et al., 1988; 1990). There are three extrinsic polypeptides at the lumenal side. The 33 kDa polypeptide protects the Mn complex of the OEC and optimizes the catalysis efficiency of water oxidation. The 24-

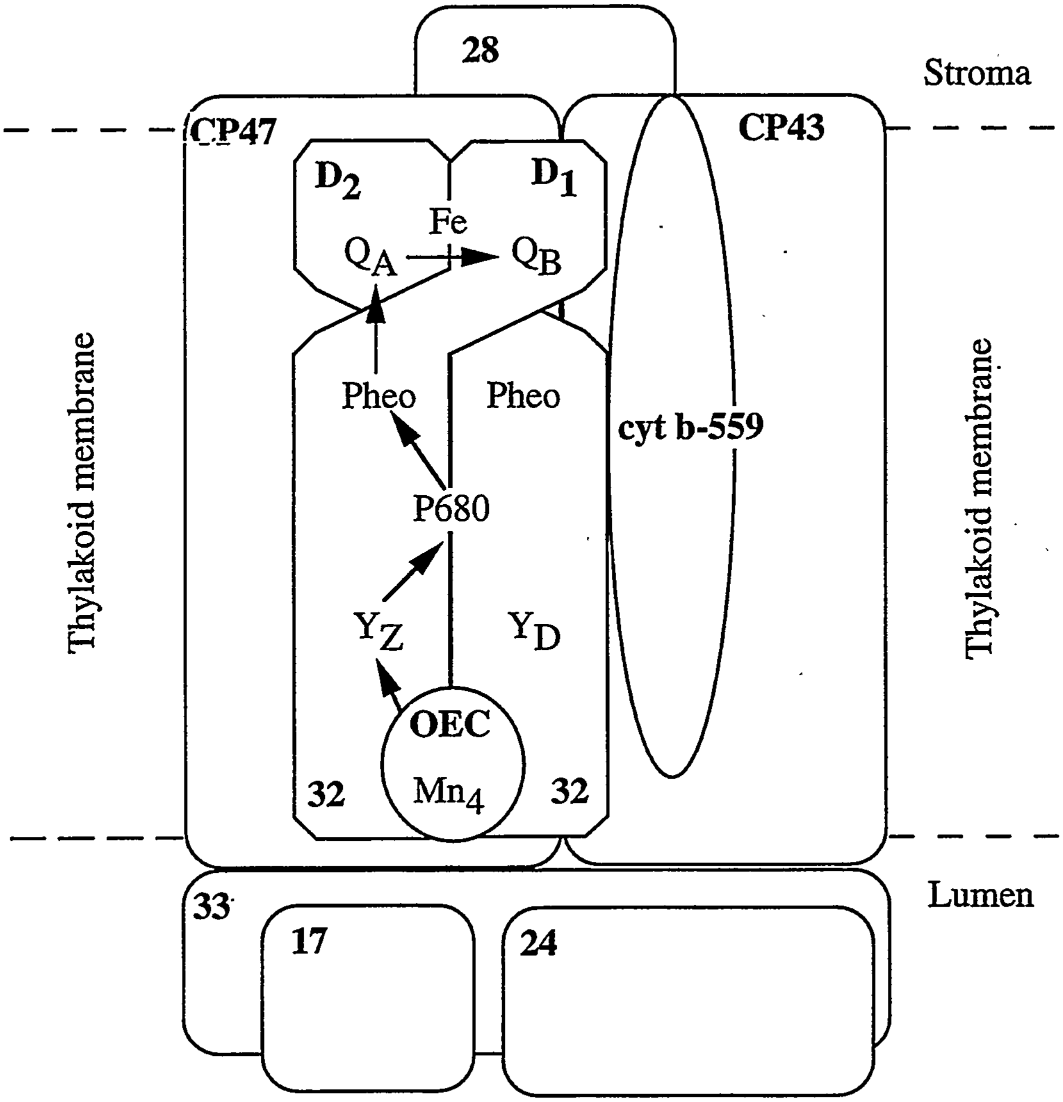

Fig. I-2. A structural model for the major polypeptide components of PSII in green plants. Apparent masses (in kilodaltons) are indicated for each polypeptide except cytochrome b-559 (as a heterodimer of 4- and 9-kDa). The 17-, 24-, and 33-kDa polypeptides are peripheral to the membrane at the lumen side. Solid arrows show the direction of electron transfer. The abbreviations used for the electron transfer components are the same as described in Fig. I-1. Adapted from Debus, (1992) *Biochim. Biophys. Acta. 1102*, 269.

and 17 kDa polypeptides also protect the Mn complex from being attacked by exogenous reductants (Debus, 1992).

I.B. The Oxygen-Evolving Complex (OEC).

Now we turn to the focus of this thesis, the structure and mechanism of the OEC. As mentioned in section I.A.2, the OEC is where the bacterial analogy becomes invalid because the purple bacteria do not evolve oxygen. Two key features of the OEC are its ability to transfer electrons singly through Y_Z to reduce P_{680}^+ and its ability to accumulate four oxidizing equivalents to oxidize water.

The oxidation of water can be represented by the following half-reaction.

$$2H_2O_{(l)} \rightarrow 4e^- + 4H^+{}_{(aq)} + O_2 \qquad (2)$$

The standard reduction potential at pH=7 (E°') of Eq. (2) is -0.817 V. We can estimate the value of ΔG¤ for the overall reaction of elelctron transport from water by combining Eq.(2) with the following half reaction:

$$NADP^+(aq) + H^+ + 2e^- \rightarrow NADPH_{(aq)} \qquad (3)$$

where E°'= -0.324 (Tinoco et al., 1995). The overall reaction of electron transport from water becomes:

$$2H_2O + 2NADP^+ \rightarrow O_2 + 2NADPH + 2H^+ \qquad (4)$$

The ΔG¤ for Eq. (4) is ~1.14 eV per electron transferred. This energy is supplied by four einsteins of photons at 680 nm. The energy of one einstein of photon at 680 nm is

1.82 eV. In terms of the average potential of water oxidation, the single photon event in PSII is able to provide enough energy for water oxidation.

The removal of four electrons from water have been modeled by scientists (Radmer & Cheniae, 1977a). Several pathes with various redox potentials at pH 7.0 can be approached. The initial step involves hydroxide radical as an intermediate with a potential as high as 2.3 V, which cannot be achieved by absorption of a single photon in PSII. Therefore, the OEC is required to stablize the high potential intermediate so the reaction in Eq.(2) can occur.

The second trick performed by the OEC is its ability to stabilize the reactive and highly oxidizing intermediates for a long time (typically minutes). It is then easy to appreciate why the OEC has drawn so much interest from scientists for many years. In the past two decades our understanding of the OEC has advanced dramatically. These advances will be described in the following subsections.

I.B.1. The Kok Cycle.

Joliot (Joliot et al., 1969) and Kok (Kok et al., 1970) and their coworkers measured the yield of molecular oxygen released by saturating light flashes. They found that the yield, as a function of the number of flashes, has an oscillation period of four. The maximum yield appeared after the third, seventh, and eleventh flash. Their results indicated the possible involvement of a complex that can store up to four oxidizing equivalents required to release one molecular oxygen. This observation was quickly confirmed (Weiss & Sauer, 1970) and Kok provided the S-state model for the OEC, as shown in Fig.I-3.

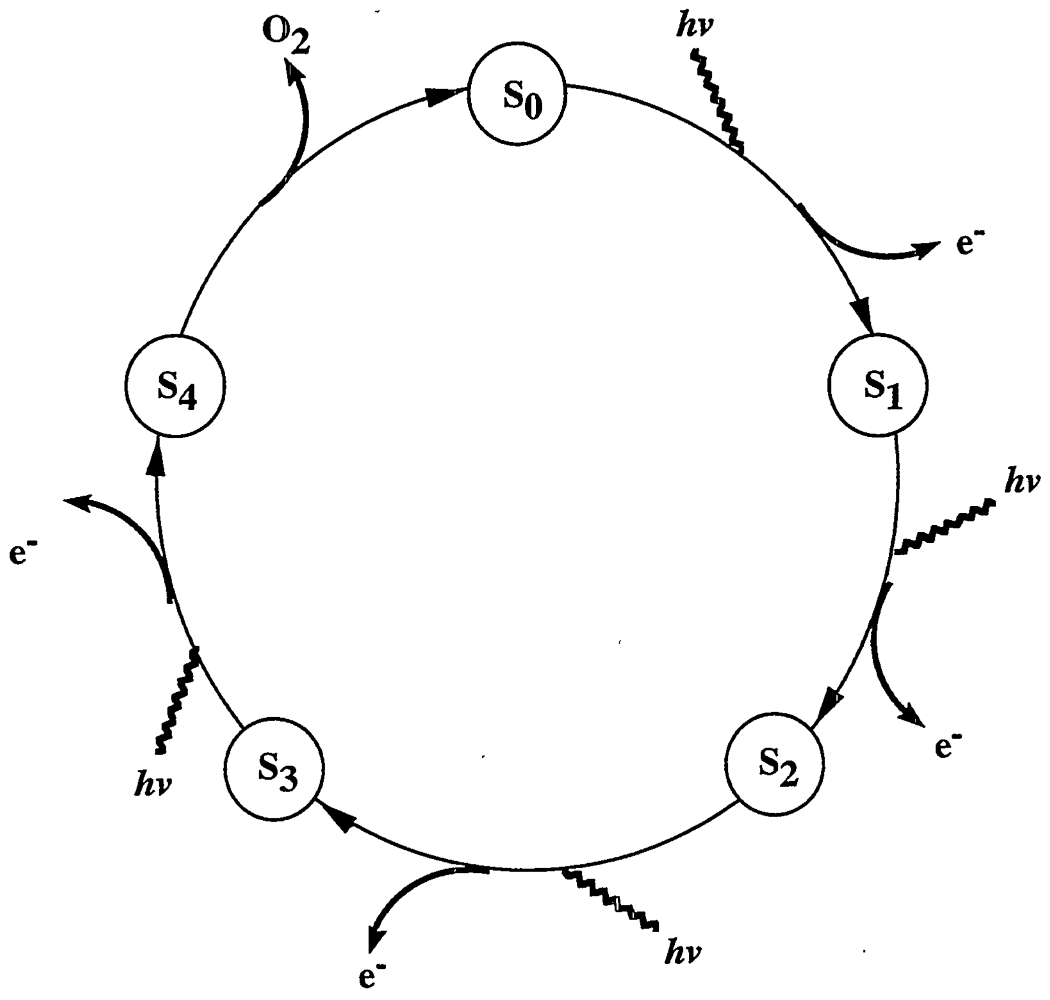

Fig. I-3. The Kok S-state model of the OEC. Each S_n represents different intermediate states of the catalytic water oxidation cycle. The subscript (n) denotes the number of the stored oxidizing equivalent

In this model, each S_n represents different intermediate states of the catalytic water oxidation cycle, and the subscript (n) denotes the number of stored oxidizing equivalents. Each successive photon activation of the PSII reaction center causes one electron transfer from the catalyst S until 4 equivalents are accumulated (the S_4 state). At this moment one molecular oxygen is released and the OEC spontaneously reverts from the S_4 state to the S_0 state. The S_4 state is a transient intermediate, and has not yet been isolated and characterized. The resting state (dark-adapted state) is not the most reduced state, S_0, but the S_1 state that is one step more oxidized.

I.B.2. Four Mn are Required for Water Oxidation.

Manganese has long been known to be required for water oxidation (Cheniae, 1980). Depletion of manganese in plants or algae results in the loss of oxygen evolution capability. This activity can be restored within 30 min upon the addition of Mn^{2+} to the growth media (Pirson, 1937). Light is also required along with Mn^{2+} to recover oxygen evolution activity in Mn-deficient algae (Kok & Cheniae, 1966; Ross & Calvin, 1967).

Mn is chosen by nature to serve in the key process of water oxidation probably because it has multiple oxidation states (ranging from +2 to +7), and some of these states have high reduction potentials. A value of four Mns per PSII reaction center is found in most experimental studies (Radmer & Cheniae, 1977b, Yocum et al., 1981). These four Mn are believed to be correlated and are generally referred to collectively as the Mn complex or the Mn cluster. The requirement of Mn for oxygen evolution has led scientists to assume the Mn complex to be the main device of the OEC to accumulate the oxidizing equivalents that corresponds to the S-state transitions.

It is still not determined whether the site for the accumulation of oxidizing equivalents (solely by the Mn complex?) is the same as the site for oxygen evolution. Renger proposed that the role for the Mn complex is only to stabilize reactive intermediates and then to accumulate oxidizing equivalents; while the formation of molecular oxygen does not happen at the same site (Renger, 1978). However, almost all of the models proposed make the implicit assumption that Mn is directly involved in the water splitting and oxygen formation, although there is no supporting experimental evidence for this (Kambara et al., 1985; Padhye et al., 1986; Christou & Vincent, 1987; Yachandra et al., 1993).

I.B.3. The Structure of the Mn Complex in OEC.

I.B.3.1. The Results from EPR Spectroscopy

The first spectroscopic evidence of the involvement of the Mn complex was discovered in the early 1980's (Dismukes & Siderer, 1981; Hansson & Andréasson, 1982). It was a multiline signal (MLS) observed by Electron Paramagnetic Resonance (EPR) in broken spinach chloroplasts following a flash of light at room temperature. A period-of-four oscillation pattern was found in the study of the dependence of the MLS on flash numbers. The MLS signal was assigned to the S_2 state because the amplitude of the MLS was maximal on the first flash and again on the fifth flash.

This 19-line partially resolved MLS was interpreted as resulting from magnetic interactions between two Mn atoms in a binuclear complex [Mn_2(II,III) or Mn_2(III,IV)] or possibly among four Mn's, i.e. Mn_4 (III, III, III, IV). Cooper and coworkers showed that the EPR spectra of synthetic, binuclear mixed-valence Mn compounds, di-μ-oxo bridged Mn(III)-Mn(IV) are similar to the partially resolved MLS from the OEC

(Cooper et al., 1978). Simulations indicated that the EPR MLS could be due to a mixed-valence complex involving Mn_2(II,III) or Mn_2(III,IV) (Brudvig & Crabtree, 1986).

The second well-studied EPR signal of the Mn cluster, centered at $g \approx 4.1$, is also associated with the S_2 state (Casey & Sauer, 1984; Zimmermann & Rutherford, 1984). This $g \approx 4.1$ EPR signal is believed to arise from a different configuration of the Mn complex (Kim et al., 1992; Liang et al., 1994). A more detailed description of this $g \approx 4.1$ EPR signal and the structural correlation between these two S_2 EPR signals can be found in chapter III.

At present, on the basis of the EPR results, a tetrameric origin for the MLS is probably the most favored (Kim et al., 1990; Rutherford, 1992). The modified S_2 MLS generated by ammonia treatment (Beck & Brudvig, 1986; Beck et al., 1986) or by the exchange of Ca^{2+} by Sr^{2+} (Boussac & Rutherford, 1988) showed 21-22 lines with reduced hyperfine spacing (6.8 mT). Unlike the native MLS, this modified MLS is more difficult to reconcile with a dimer model (Rutherford, 1992). An even more drastically modified MLS generated by a Ca^{2+}-depletion procedure showed at least 26 lines and ~30 lines in oriented Ca^{2+}-depleted PSII particles (Boussac et al., 1990). These results support the hypothesis that more than two Mn ions make up the Mn cluster responsible for these MLS (Boussac et al, 1990). The MLS spectra measured at S-band (3.8 GHz) also supported a model bigger than a dimer (Haddy et al., 1989).

Recently, a 13-16 mT-wide EPR signal centered at g=2.0 has been observed from Ca^{2+}-depleted (Boussac, et al., 1990; Tso et al., 1991; Hallahan et al., 1992), Cl^--depleted (Baumgarten et al., 1990; Boussac et al., 1992) and F^--inhibited (Baumgarten et al., 1990) PSII samples. These signals have been attributed to a modified form of the "S_3" state (Boussac, et al., 1990; Baumgarten et al., 1990; Boussac et al., 1992) or to an "S_2-plus-radical" state arising from the magnetic interaction between the Y_Z^+ and the Mn complex of the S_2 state (Hallahan et al., 1992).

I.B.3.2 The Results from XAS.

Another important technique -- X-ray absorption spectroscopy (XAS) -- has made an influential contribution to the current structural understanding of the Mn cluster. XAS is a powerful tool which can provide structure information at the molecular level without the need for a crystal. Chapter II contains further discussion of the use of this technique to examine the Mn cluster in OEC. Two types of information can be obtained from XAS: (a) the ligand environment, and (b) the oxidation state of the Mn absorber. Information about the ligand environment can be achieved from the extended X-ray absorption fine structure (EXAFS). The theory of XAS will be further described in chapter II.

EXAFS data have been obtained on the OEC of the isotropic PSII samples poised at the S_1 state (McDermott et al., 1988; Penner-Hahn et al., 1990; Sauer et al., 1992; MacLachlan et al., 1992; Yachandra et al., 1993), and at the S_2 state after continuous illumination at 140 K (Liang et al., 1994) or at 200 K (McDermott et al., 1988; Sauer et al., 1992; MacLachlan et al., 1992; Yachandra et al., 1993). Both the S_1 and S_2 states have been examined in Ca^{2+}-depleted and Sr^{2+}-reconstituted PSII particles (Latimer et al., manuscript in preparation). Oriented membranes for the native (Mukerji et al., 1994) and ammonia-treated (Dau et al., manuscript in preparation) PSII samples have also been measured. The EXAFS of S_0^* and S_3^* state have been reported using special protocols to prepare these states in the majority of the PSII centers (Guiles et al., 1990a,b). The * sign differentiates these chemical-induced S-states from the native, flash-induced S-states (see below and chapter IV).

The Fourier transforms of the EXAFS data show three well resolved peaks. The simulation results are summarized as follows:

1) There are approximately 2 N or O ligand atoms per Mn at ~1.8 Å;

2) There are 2 to 4 N or O ligand atoms per Mn at 1.9-2.2 Å;

3) Each Mn atom in the Mn cluster has 1-1.5 Mn atom neighbors at a distance of ~2.7 Å and 0.5 Mn-Mn or Mn-Ca vector at 3.3 Å;

4) The dichroism studies indicate that the two 2.7 Å vectors are oriented with an average angle of ~ 60° with respect to the membrane normal. The 3.3 Å vector, on the other hand, makes an angle of ~43° with respect to the membrane normal (Mukerji et al., 1994).

On the basis of these observations and interpretation from the previous reports, Klein and coworkers proposed a model (Yachandra et al., 1993) of the Mn cluster diagrammed in Fig. I-4. This model consists of two di-μ-oxo bridged Mn dimers that are bridged by one mono-μ-oxo and one or two carboxylato bridges. Mn-Mn distances of 2.7 Å are characteristic of di-μ-oxo bridged Mn complexes. The closest distance between the two di-μ-oxo bridged Mn dimers is 3.3 Å, which is characteristic of the Mn-Mn distances in synthetic di-μ-carboxylato bridged Mn complexes.

Note that this model is a straightforward construction based on the distances and coordination numbers acquired from the OEC data. This model is also compatible with the results of EPR (mentioned before) and oriented-PSII EXAFS studies. A list of possible arrangements of the Mn cluster in the OEC has been discussed (DeRose et al., 1994). The EXAFS results do not support the symmetric cubane clusters (Brudvig & Crabtree, 1986) or the "butterfly" tetranuclear clusters (Christou & Vincent, 1987).

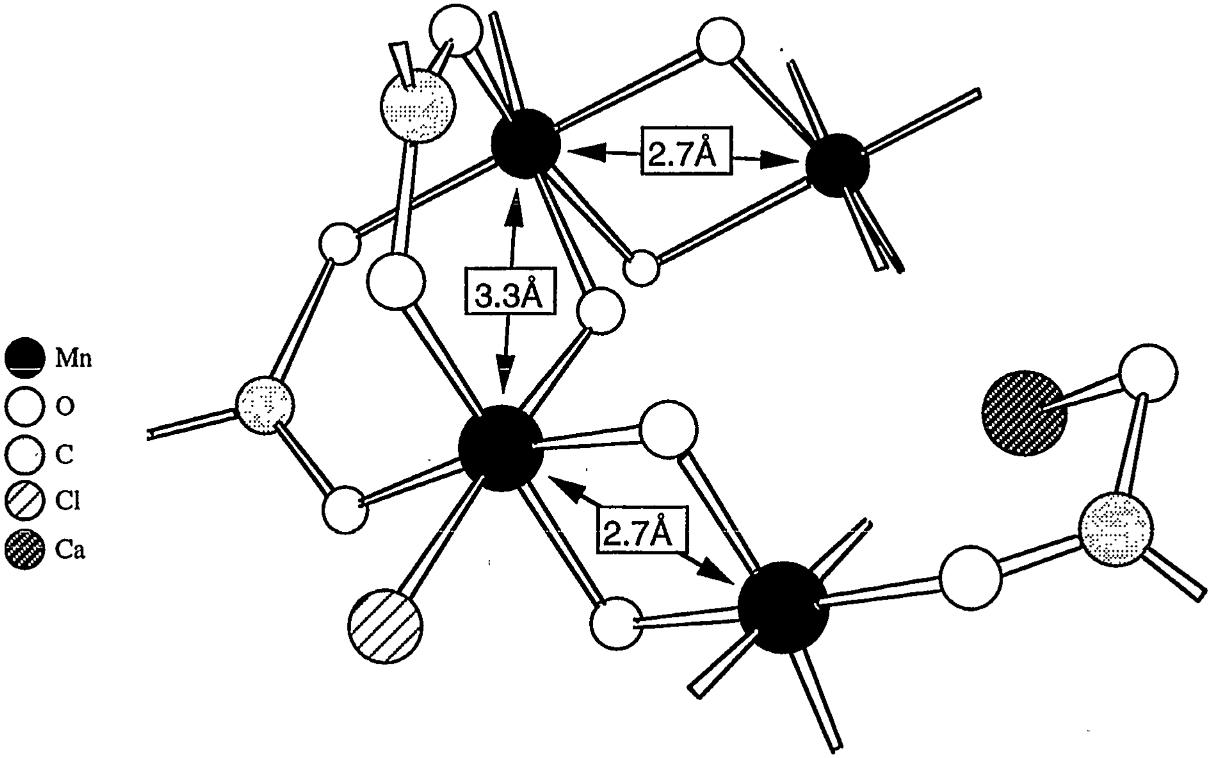

Fig. I-4. Proposed Model for the Manganese Complex in Photosystem II. Adapted from Yachandra et al., (1993) *Science 260*, 675.

I.B.4. The Oxidation States of the Mn Complex in OEC.

In the Kok cycle, the oxidation equivalents are stored stepwise in the OEC after each photon absorption. Spectroscopic attempts (including XAS, UV, Near-IR, IR, EPR & NMR) to identify the redox states of the Mn cluster or other molecular species have produced an abundance of information. However, no general agreement has been achieved yet, even when similar techniques are used. The following sub-sections are the author's attempt to provide a brief summary from various spectroscopic methods.

I.B.4.1. The Valence state of the Mn complex from XAS.

As mentioned in section I.B.3, XAS also furnishes valence state information on the Mn complex at different S-states. XAS is intuitively a good approach to this question among the available spectroscopic methods because the X-ray absorption edge energy is sensitive to the oxidation state of the Mn cluster. From the inflection point of the Mn absorption edge, and the shape of the edge as well as the pre-edge, information on the redox states of the Mn ions in different S-states has been deduced (Yachandra et al., 1993).

The Klein/Sauer group proposed two Mn(III) and two Mn(IV) in the S_1 state. Upon advancing to the S_2 state, one Mn(III) is oxidized to Mn(IV) (Sauer et al., 1992; Yachandra et al., 1993). These conclusions were obtained after a careful comparison of the second derivative analyses of the XAS edge and pre-edge features of many Mn model compounds (Sauer et al., 1992). These assignments are now generally agreed upon by the XAS-OEC community (Kusunoki et al., 1990; Penner-Hahn et al., 1992). In addition, the bond valence sums calculation based on bond lengths determined by crystallography or EXAFS also predicted the S_1 state to contain two Mn(III) and two Mn(IV) (Thorp, 1992). This method has successfully predicted the correct oxidation states of the metal ions in a variety of model compounds and metalloenzymes (Thorp, 1992).

The edge position has also been measured in samples that were poised predominantly at the S_0^* and S_3^* states using special protocols (Guiles et al., 1990a,b). The K-edge shift in the $S_1 \rightarrow S_0^*$ transition shows that the oxidation state decreases by one equivalent per four Mn. This outcome indicates that Mn is oxidized during the $S_0^* \rightarrow S_1$ transition. There is a significant change in the structure of the complex during the $S_0^* \rightarrow S_1$ transition evident from the EXAFS results. The Klein/Sauer group concludes that this structural change is consistent with oxidation of Mn(II) to Mn(III) in a multinuclear complex by comparison to inorganic Mn model compounds.

On the other hand, there is little or no edge shift or change of edge shape detected from the $S_2 \rightarrow S_3^*$ advancement. According to the EXAFS, no significant change of the ligand environment was observed upon S_3^* formation (Guiles et al, 1990b). These results have been interpreted to reflect no Mn oxidation during the $S_2 \rightarrow S_3^*$ transition.. Therefore, the oxidative equivalent stored within the OEC during this transition probably stays on another intermediate donor to the Mn complex, or delocalizes to ligand(s) of the Mn complex. Possible amino acid residues including histidine (Guiles et al., 1990b; Boussac et al., 1990) or tyrosine (Hallahan et al., 1992; MacLachlan & Nugent, 1993) have been proposed to either ligate or reside close to the Mn cluster. The magnetic coupling between these redox active amino acid residues and the Mn complex is thought to account for the lack of observable EPR signals in the native S_3 state.

As mentioned in section I.B.3.1., a "modified S_3" or an "S_2-plus-radical" EPR signal generated from the Ca^{2+}-depleted PSII has been observed and proposed to arise from a redox-active histidine residue. A small edge shift of 0.3 eV is detected in this modified $S_2 \rightarrow S_3$-state transition (Latimer et al., manuscript in preparation).

Note that the XAS K-edge results mentioned so far are PSII samples prepared by continuous illumination at suitable conditions to achieve these various S-states. One can argue that these modified S_3 (including the S_3* and the Ca^{2+}-depleted S_3 samples) and S_0* states are generated under non-physiological conditions (either illuminated at cryogenic temperature or pre-treated by strong oxidants or reductants) and they may not accurately represent the native S-states in PSII. The obvious solution is to measure the XAS from the native S-states induced by room-temperature flashes. This approach had been very difficult because the XAS measurement requires concentrated samples that are almost impossible to saturate by sources of flash light. This situation changed recently when a much improved X-ray fluorescent detecting system became available (see chapter II).

We have successfully acquired high quality K-edge spectra from all of the S-states induced by saturating flashes from either a Xe-lamp or a Nd-YAG laser. These results confirm our previous XAS reports on thick samples (illuminated by continuous light source) that Mn is oxidized during the $S_0 \rightarrow S_1$ and $S_1 \rightarrow S_2$ transitions. Also, consistent with our previous results, the current XAS on the flash-induced S_3 state better supports the absence of Mn oxidation during the $S_2 \rightarrow S_3$ transition. This experiment will be described in detail in Chapter IV.

On the other hand, Ono and coworkers reported XAS results on flash-induced PSII samples that support one equivalent of Mn oxidation during the $S_2 \rightarrow S_3$ transition (Ono et al., 1992; Kusunoki et al., 1993). Similar conclusions have also been drawn from flash-induced S_3 state on Ca^{2+}-depleted (Ono et al, 1993), as well as continuously illuminated, S_3 state in acetate-, ammonia- and sodium chloride-inhibited PSII membranes (MacLachlan et al., 1994). In addition to these XAS results, those studied by UV optical spectroscopy also support one equivalent of Mn oxidation upon the S_3 formation (See below).

A summary of the current view of the Mn edge data from the XAS is as follows. There is consensus on the interpretation of the $S_1 \rightarrow S_2$ transition, where the Mn oxidation states are thought to be two Mn(III) and two Mn(IV) in the S_1 state, and one Mn(III) oxidizes to Mn(IV) in the S_2 state. We conclude from both PSII and Mn model compound studies that the scheme for oxidation state changes of the S-states is most likely to be (Sauer et al., 1992):

S_0	Mn_4(II,III,IV,IV)
S_1	Mn_4(III,III,IV,IV)
S_2	Mn_4(III,IV,IV,IV)
S_3	Mn_4(III,IV,IV,IV)

The oxidation state assignment for S_3 is controversial: other groups (see above) support an oxidation state of Mn_4(IV,IV,IV,IV) in the S_3 state. The origin of the discrepancy is not clear.

I.B.4.2. Studies from Other Spectroscopic Methods.

I.B.4.2.1. Optical Spectroscopy.

Difference spectra of the successive S-state transitions have been obtained in the UV and near-IR regions.

UV. The procedures to quantify and assign the difference spectra are complicated, and the results are often not reproducible. Different amplitudes and shapes of the spectra among various laboratories result in a large degree of controversy. At present, there is reasonable agreement that an absorption change occurs on the $S_2 \rightarrow S_3$ transition which is about the same size as that on the $S_1 \rightarrow S_2$ transition , at least in the region around 350 nm (Dekker & Van Gorkom, 1987; Saygin & Witt, 1987; Lavergne, 1989; Kretschmann et al., 1988; Van Leeuwen et al., 1990).

Near-IR. Weak absorption changes in the near infrared region associated with the S-state transitions have been observed. They have been attributed to intervalence electronic transitions within a mixed-valent Mn cluster (Dismukes & Mathis, 1984; Dismukes, 1986). The absorption changes appear upon S_2 formation, remain unchanged on S_3 formation, and decrease on S_0 formation. These results imply that no Mn oxidation occurs on formation of the S_3. However, this assignment has been questioned, and the absorbance change could be explained by sample scattering (Velthuys, 1988).

I.B.4.2.2 EPR Relaxation Studies.

At low temperature, the spin-lattice relaxation rate of the EPR signal of the tyrosine radical Y_D^+ is accelerated by dipolar coupling to other nearby paramagnets, including the Mn complex. The results show that S_0 is the fastest relaxing state, S_1 is the slowest, S_2 and S_3 are identical and are faster relaxing than S_1. These data are interpreted as suggestive of: 1) a diamagnetic Mn complex in the S_1 state; 2) no Mn oxidation during the $S_2 \rightarrow S_3$ transition; 3) the presence of a mixed-valence, s=1/2 state in both the S_2 and S_3 states; and 4) a s=1/2 Mn cluster containing Mn(II) in the S_0 state (Styring & Rutherford, 1988).

I.B.4.2.3 NMR Proton Relaxation Studies.

The relaxation of solvent water protons is enhanced when they rapidly exchange with protons which are close to fast relaxing paramagnets. Flash-induced enhancements in the NMR spin-lattice relaxation rate of solvent protons have been detected at room temperature in PSII using a highly sensitive NMR instrument (Srinivasan & Sharp, 1986a,b). Among the Mn oxidation states, Mn(II) and Mn(IV) in high-spin octahedral environments are candidates as strongly relaxing centers, while Mn(III) has very large static zero-field splittings and is very weakly relaxing. Therefore, changes occurring in the proton relaxation enhancement after each S-state transition were correlated with the redox state of the Mn.

The results from these studies show 1) that the S_0 state is fast relaxing, indicating the presence of Mn(II); 2) that upon formation of the S_1 state, a slow relaxing state is produced; thus Mn(II) oxidizes to Mn(III) during the $S_0 \rightarrow S_1$ transition; 3) an increase in proton relaxation rate upon formation of the S_2 state, indicating that one Mn(III) is oxidized to Mn(IV); and 4) no change has been found upon the formation of the S_3 state, and therefore implies no Mn oxidation occurring in the $S_2 \rightarrow S_3$ transition.

A summary of the above results indicates that the near IR absorption spectroscopy and both the EPR & NMR relaxation studies do not support Mn oxidation occurring in the $S_2 \rightarrow S_3$ transition. Conflicting assignment is found only from the UV absorption spectroscopy.

I.C. The Goals.

In comparison with the mechanisms of carbon dioxide assimilation and electron transport, that of photosynthetic oxygen evolution is much less understood. Thus, the goals of our work are to reveal :

A) more detailed structure of the Mn complex;

B) how this structure is important for functions of the OEC to store oxidizing equivalents generated by the PSII reaction center;

C) how those oxidizing equivalents are used to convert two water molecules to one oxygen molecule; and

D) whether the site for the accumulation of oxidizing equivalents (solely by the Mn complex?) is the same as the site for oxygen evolution.

Obviously, a full understanding of the structure of the Mn complex at each S-state is important before we can understand the mechanism and active site of the OEC. Thus, the purpose of this thesis is to employ the XAS to seek answers on the following two structure-related questions:

(1) What are the structural correlations between the two EPR signals (the MLS and $g\approx4.1$) from the S_2 state?

(2) What are the oxidation states of the Mn cluster in each S-state? When samples are prepared under physiological condition, are the results similar to those prepared at the cryogenic temperature? Is the Mn complex the sole site to accumulate the oxidizing equivalents in the Kok scheme?

This thesis starts from a general introduction of photosynthesis then gradually focuses to the core of my interest, the structure and valence state of the Mn cluster in the OEC. Materials and methods related to this work are covered in chapter II. The results aiming to answer question (1) are described in chapter III. Chapter IV will offer our current point of view on question (2).

I.D. Reference.

Baumgarten, M., Philo, J. S. & Dismukes, G. C. (1990) *Biochemistry 29*, 10814

Beck, W. F. & Brudvig, G, W. (1986) *Biochemistry 25*, 6479

Beck, W. F., de Paula, J. C. & Brudvig, G, W. (1986) *J. Am. Chem. Soc. 108,* 4018

Boussac, A. & Rutherford, A. W. (1988) *Biochemistry 27*, 3476

Boussac, A., Zimmermann, J.-L. & Rutherford, A. W. (1988) in *Current Research in Photosynthesis* (Baltscheffsky, M., ed.), Vol. I, pp. 713-716, Kluwer, Dordrecht.

Boussac, A., Zimmermann, J.-L., Rutherford, A. W. & Lavergne, J. (1990) *Nature 347*, 303

Boussac, A., Sétif, P. & Rutherford, A. W. (1992) *Biochemistry 31*, 1224

Bowlby, N. R., Petersen, J., Babcock, G. T. & Yocum, C. F. (1990) in *Current Research in Photosynthesis* (Baltscheffsky, M., ed.), Vol. I, pp. 539-542, Kluwer, Dordrecht.

Bowlby, N. R., Ghanotakis, D. F., Yocum, C. F., Petersen, J. & Babcock, G. T. (1988) in *Light-Energy Transduction in Photosynthesis: Higher Plant and Bacterial Models* (Stevens, S. E., Jr. and Bryant, D. A., eds.), pp. 215-226, American Socieity of Plant Physiologists, Rockville.

Bricker, T. M. (1990) *Photosynth. Res. 24*, 1

Brudvig, G. W. & Crabtree, R. H. (1986) *Proc. Natl. Acad. Sci. U.S. A. 83*, 4586

Buser, C. A., Diner, B. A. & Brudvig, G. W. (1992) *Biochemistry 31*, 11441

Casey, J. L., & Sauer, K. (1984) *Biochim. Biophys. Acta 767*, 21

Cheniae, G. (1980) *Methods Enzymol. 69*, 349

Christou, G. & Vincent, J. B. (1987) *Biochim. Biophys. Acta. 895,* 259

Cooper, S. R.; Dismukes, G. C.; Klein, M. P.; Calvin, M. (1978) *J. Am. Chem. Soc. 100*, 7248

Debus, R. J. (1992) *Biochim. Biophys. Acta. 1102,* 269

Dekker, J. P. & Van Gorkom, H. J. (1987) *J. Bioenerg. Biomembr. 19,* 125

DeRose, V. J., Mukerji, I., Latimer, M. J., Yachandra, V. K., Sauer, K., & Klein, M. P. (1994) *J. Am. Chem. Soc. 116,* 5239

Deisenhofer, J., Epp, O., Miki, K., Huber, R., & Michel, H. (1984) *J. Mol. Biol.*, 180, 385

Dismukes, G. C., & Siderer, Y. (1981) *Proc. Natl. Acad. Sci. U.S.A. 78*, 274

Dismukes, G. C. & Mathis, P. (1984) *FEBS Lett. 178*, 51

Dismukes, G. C. (1986) *Photochem. Photobiol. 43*, 99

Gerken, S., Brettel, K., Schlodder, E. & Witt, H. T. (1988) *FEBS Lett. 237*, 69

Guiles, R. D., Yachandra, V. K., McDermott, A. E., Cole, J. L., Dexheimer, S. L., Britt, R. D., Sauer, K., & Klein, M. P. (1990a) *Biochemistry 29*, 486

Guiles, R. D., Zimmermann, J.-L., McDermott, A. E., Yachandra, V. K., Cole, J. L., Dexheimer, S. L., Britt, R. D., Wieghardt, K., Bossek, U., Sauer, K., & Klein, M. P. (1990b) *Biochemistry 29*, 471

Haddy, A., Aasa, R. & Andréasson, L.-E. (1989) *Biochemistry 28* , 6954

Hallahan, B. J., Nugent, J. H. A., Warden, J. T. & Evans, M. C. W. (1992) *Biochemistry 31*, 4562

Hansson, Ö., & Andréasson, L.-E. (1982) *Biochim. Biophys. Acta 679*, 261

Hearst, J. E. (1986) *Encycl. Plant Physiol., New Ser. 19*, 382

Hoganson, C. W. & Babcock, G. T. (1988) *Biochemistry 27*, 5848

Joliot, P.; Barbien, G.; Chabaud, R. (1969) *Photochem. Photobiol. 10*, 309

Kambara, T.; Hendrickson, D. N.; Govindjee (1985) *Proc. Natl. Acad. Sci. USA , 82*, 6119

Kim, D. H., Britt, R. D., Klein, M. P., & Sauer, K. (1990) *J. Am. Chem. Soc. 112*, 9389

Kok, B. & Cheniae, G. M. (1966) *Curr. Top. Bioenerg. 1*, 1

Kok, B.; Forbush, B.; McGloin, M. (1970) *Photochem. Photobiol. 11*, 457

Kretschmann, H., Dekker, J. Pl, Saygin, O. & Witt, H. T. (1988) *Biochim. Biophys. Acta. 932,* 358

Kusunoki, M., Ono, T., Suzuki, M., Uehara, A., Matsushita, T., Oyanagi, H., & Inoue, Y. (1990) in *Current Research in Photosynthesis* (Baltscheffsky, M., ed.), Vol.

I, pp. 801-804, Kluwer, Dordrecht.

Kusunoki, M., Ono, T.-A., Noguchi, T., Inoue, Y. & Oyanagi, H. (1993) *Photosynthesis Research 38*, 331

Lavergne, J. (1989) *Proc. Nat. Acad. Sci. USA 86*, 8768

Leibl, W., Breton, J., Deprez, J. & Trissl, H. -W. (1989) *Photosynth. Res. 22*, 257

Liang, W., Latimer, M. J., Dau, H., Roelofs, T. A., Yachandra, V. K., Sauer, K., & Klein, M. P. (1994) *Biochemistry 33*, 4923

MacLachlan, D. J., Hallahan, B. J., Ruffle, S. V., Nugent, J. H., Evans, M. C. W., Strange, R. W. & Hasnain, S. S. (1992) *Biochem. J. 285*, 569

MacLachlan, D. J. & Nugent, J. H. (1993) *Biochemistry 32*, 9772

MacLachlan, D. J., Nugent, J. H. A. & Evans, M. C. W. (1994) *Biochim. Biophys. Acta. 1185,* 103

McDermott, A. E., Yachandra, V. K., Guiles, R. D., Coles, J. L., Dexheimer, S. L., Britt, R. D., Sauer, K., & Klein, M. P. (1988) *Biochemistry 27*, 4021

Michel, H. & Deisenhofer, J. (1988) *Biochemistry 27*, 1

Miller, A.-F. & Brudvig, G. (1991) *Biochim. Biophys. Acta. 1056,* 1

Mukerji, I., Andrews, J. C., DeRose, V. J., Latimer, M. J., Yachandra, V. K., Sauer, K., & Klein, M. P. (1994) *Biochemistry 33,* 9712

Nuijs, A. M., Van Gorkom, H. J., Plijter, J. J. & Duysens, L. N. M. (1986) *Biochim. Biophys. Acta. 848*, 167

Okamura, M. Y., Feher, G. & Nelson, N. (1982) in *Photosynthesis: Energy Conversion*

by Plants and Bacteria, I (Govindjee, ed.), pp. 195-272, Academic Press, N. Y.

Ono, T.-A., Noguchi, T., Inoue, Y., Kusunoki, M., Matsushita, T. & Oyanagi, H. (1992) *Science 258*, 1335

Ono, T.-A., Noguchi, T., Inoue, Y., Kusunoki, M., Yamaguchi, H. & Oyanagi, H. (1992) *FEBS Lett. 330* , 28

Padhye, S.; Kambara, T.; Hendrickson, D. N.; Govindjee (1986) *Photosyn. Res., 9,* 103

Penner-Hahn, J. E., Fronko, R. M., Pecoraro, V. L., Yocum, C. F., Betts, S. D., & Bowlby, N. R. (1990) *J. Am. Chem. Soc. 112*, 2549

Penner-Hahn, J. E., Fronko, R. M., Pecoraro, V. L., Yocum, C. F., Betts, S. D., & Bowlby, N. R. (1992) *J. Am. Chem. Soc. 114,* 10650

Pirson, A. (1937) *Z. Botan 31*, 193

Radmer, R. & Cheniae, G. (1977a) in *Primary Processes of Photosynthesis*, J. Barber,

ed., Elsevier, Amsterdam, pp. 303.

Radmer, R.; Cheniae, G. M.(1977b) *Top. Photosynth. 2,* 303

Renger, G. (1978) in *Photosynthetic Oxygen Evolution*; Metzner, H., Ed.; Academic: London; pp 229.

Ross, R. T. & Calvin, M. (1967) *Biophys. J. 7*, 595

Rutherford, A. W. (1987) in *Progress in Photosynthesis Research* (Biggins, J., ed.), Vol. I, pp. 277-283, Martinus Nijhoff / Dr. Junk, Dordrecht.

Rutherford, A. W. (1992) in *The Photosystems: Structure, Function and Molecular Biology* (Barber, J. ed.), pp. 180-229, Elsevier Science Publishers B.V.

Sagin, O. & Witt, H. T. (1987) *Biochim. Biophys. Acta 893,* 452

Sauer, K., Yachandra, V. K., Britt, R. D., & Klein, M. P. (1992) in *Manganese Redox Enzymes* (Pecoraro, V. L., Ed.) pp. 141-175, VCH Publishers, New York.

Sauer, K. (1980) *Acct. Chem. Res. 13*, 249

Srinivasan, A. N. & Sharp, R. R. (1986a) *Biochim. Biophys. Acta 850,* 211

Srinivasan, A. N. & Sharp, R. R. (1986b) *Biochim. Biophys. Acta 851,* 329

Styring, S. & Rutherford, A. W. (1988) *Biochemistry 27*, 4915

Thorp, H. H. (1992) *Inorg. Chem. 31*, 1585.

Tinoco, I., Sauer, K. & Wang, J. (1995) in *Physical Chemistry: Principles and Applications in Biological Sciences.* Chapter IV. Prentice-Hall, INC., New Jersey.

Tso, J., Sivaraja, M. & Dismukes, G. C. (1991) *Biochemistry 30*, 4734

Van Leeuwen, P. J., Vos, M. H. & Van Gorkom, H. J. (1990) *Biochim. Biophys. Acta 1018*, 173

Velthuys, V. E. (1988) *Biochim. Biophys. Acta 933,* 249

Weiss, C.; Sauer, K. (1970) *Photochem. Photobiol. 11*, 495

Yachandra, V. K., DeRose, V. J., Latimer, M. J., Mukerji, I., Sauer, K., & Klein, M. P. (1993) *Science 260*, 675

Yocum, C. F., Yerkes, C. T., Blankenship, R. E., Sharp, R. R. & Babcock, G. T. (1981) *Proc. Nat. Acad. Sci. USA 78*, 7507

Zimmermann, J.-L., & Rutherford, A. W. (1984) *Biochim. Biophys. Acta 767*, 160

Chapter II. Material and Methods.

II.A. Preparation of Oxygen-Evolving PSII Membranes.

Two types of protocols were used to prepare the PSII particles in this thesis. Table II-1 lists the buffers used in both preparations.

II.A.1. Type-1.

Type-1 samples were prepared from a protocol modified from the BBY method described by Berthold et al. (1981). Fresh spinach (4-7 bunches) from the market was washed in ice-water and destemmed. In the cold room (4°C), the leaves were further torn to small pieces and ground in a Waring blender for 10 s in 800 ml Grind buffer [4 mM $MgCl_2$, 1 mM EDTA, 0.4 M NaCl, 5 mM sodium ascorbate, 2 mg/ml bovine serum albumin (BSA), 50 mM Hepes, pH 7.5]. The BSA and sodium ascorbate were added to the Grind buffer shortly before the grinding procedure. The grinding blend was filtered through 2 and then 16 layers of cheesecloth and immediately spun down at 5,000 g (Sorvall GS3 or GSA rotors, 6,000 rpm, 4°C) for 10 min. All of the following steps were performed under dim green light and on ice in the 4°C room. The chloroplast pellet was washed with 300 ml Wash buffer [150 mM NaCl, 8 mM $MgCl_2$, 50 mM Hepes, pH 6.0] and centrifuged again as above. The thylakoid pellet was then resuspended into a small amount of Resin (resuspension and incubation) buffer [15 mM NaCl, 10 mM $MgCl_2$, 50 mM MES, pH 6] to a chlorophyll concentration of ~ 3 mg Chl/ml. Typically 220-360 mg Chl was obtained from 5-7 bunches of spinach. A proper amount of Resin buffer and 25% stock solution of Triton X-100 (dissolved in Resin buffer) were added to make the mixture a final concentration of 2 mg Chl/ml and a Triton-to-chlorophyll ratio (w/w) of 25:1. This mixture was incubated with slow stirring in the dark at 0°C for 25

Table II-1. Media Used in the Preparation of PSII-Enriched Membranes from Spinach

Medium	Chemical	Final Concentration	Concentration and the Preparation (gram/liter) of Stock	Volume (ml) of Stock per 1 liter of Medium
Grind	NaCl	400 mM	4.0 M, (117 g / 0.5 l)	100.0
(pH 7.5)	$MgCl_2\cdot 6H_2O$	4 mM	0.4 M, (40.7 g/ 0.5 l)	10.0
	$EDTA\cdot Na_2$	1 mM	0.1 M, (7.4 g / 0.2 l)	10.0
	HEPES[a] (Free Acid)	50 mM	1.0 M, (59.6 g / 0.25 l)	50.0
	Sodium[b] Ascorbate	5 mM	1.0 g / 1.0 liter	
	BSA[b]	2 mg/ml	2.0 g / 1.0 liter	
Wash	NaCl	150 mM	4.0 M, (117 g / 0.5 l)	37.5
(pH 6.0)	$MgCl_2\cdot 6H_2O$	8 mM	0.4 M, (40.7 g/ 0.5 l)	20.0
	MES[a]	50 mM	1.0 M, (39.0 g / 0.2 l)	50.0
Resin	NaCl	15 mM	4.0 M, (117 g / 0.5 l)	3.75
(pH 6.0)	$MgCl_2\cdot 6H_2O$	10 mM	0.4 M, (40.7 g / 0.5 l)	25.0
	MES[a]	50 mM	1.0 M, (39.0 g / 0.2 l)	50.0
Medium A[c]	NaCl	15 mM	4.0 M, (117 g / 0.5 l)	3.75
(pH 6.5)	$MgCl_2\cdot 6H_2O$	5 mM	0.4 M, (40.7 g / 0.5 l)	12.5
	MES[a]	50 mM	1.0 M, (39.0 g / 0.2 l)	50.0
	$CaCl_2\cdot 2H_2O$	5 mM	0.1 M, (7.4 g / 0.5 l)	50.0

[a] Stored at 4°C.

[b] Added freshly before use.

[c] A cryoprotectant (either sucrose to a final concentration of 400 mM or 50% (v/v) glycerol) is usually added into Medium A.

min. The suspension was then centrifuged immediately (within 2 min) at 37,000 g (Sorvall SS34 rotor, 17,500 rpm) for 30 min. The PSI membranes were in the soluble phase; therefore, the resulting pellet was PSII-enriched. These PSII-enriched membranes were resuspended in Resin buffer and centrifuged at 500 g (Sorval SS34 rotor, 2,000 rpm) for 2 min. This low-speed cut spun down most unwanted materials including intact thylakoids, other cell debris and starch (white color) into the pellet. Inevitably, approximately 17 % of the PSII-enriched particles was also centrifuged into the pellet. The supernatant was then pelleted by centrifugation at 37,000 g (Sorvall SS34 rotor, 17,500 rpm) for 30 min. Depending on the spinach, sometimes various amounts of residual starch was found at the bottom of the tubes after this centrifugation. Care then was applied in the following resuspending steps to leave out the small white pellets.

The pelleted PSII-enriched membranes were washed in Medium A [15 mM NaCl, 5 mM $MgCl_2$, 5 mM $CaCl_2$ and 50 mM MES at pH 6.5] with 0.4 M sucrose and centrifuged for 30 min at 37,000 g. After one more wash and centrifugation at 37,000 g for 30 min, this pellet was stored at -20°C if not for immediate use. Right before use, the pellet was thawed in ice in complete darkness for one hour, then washed in Medium A with 0.4 M sucrose and spun down. Depending on the experiments to be performed, pelleted PSII was used directly or resuspended into Medium A with 0.4 M sucrose or 50% (v/v) glycerol to a suitable chlorophyll concentration. The yield of PSII is typically ~ 40-50 % of the amount of the thylakoid. The specific activities of oxygen evolution is ~ 600 μmol of O_2/mg of Chl/h.

II.A.2. Type-2.

This protocol was modified from the K&M method described by Kuwabara & Murata (1982). This modified version of the preparation basically used the same media and procedures as the BBY-type protocol, except the incubation time of detergent treatment was only 1 min. Possible damage or distortion of the Q_B site due to a long exposure of the thylakoid membranes to strong detergents (e.g. Triton X-100) in a BBY-type protocol has been a concern (personal communication with Dr. T. Ono). Because the detergent incubation time in the KM-type preparation was significantly shorter, PSII membranes with a more intact Q_B site were obtained at the expense of an increased content of PSI. Consequently the specific oxygen-evolving activity was lower, typically ~350-450 μmol of O_2/mg of Chl/h. Compared with the PSII membranes generated from the KM-type (Type-2) preparation, the higher content of the distorted Q_B site in membranes from the BBY-type (Type-1) protocol resulted in an offset of the period-of-four pattern after the second flash and more scrambling of the distribution of the S-states at higher flash numbers. This will be described further in Chapter IV.

II.B. Oxygen Evolution Measurements.

Oxygen evolution activity was measured by a Clark-type oxygen electrode (Yellow Springs Instruments, Ohio) as described by DeRose (1990), with one modification. Instead of water, 5% $CuSO_4$ solution was put in the spherical flask which was aligned before the electrode cuvette. The function of this spherical flask was to both focus the light and to perform as a better heat filter with $CuSO_4$ solution in it.

II.C. Sample Preparation for Both EPR and XAS.

II.C.1. Preparation of the "Thick" Samples.

The "thick" samples for both X-ray absorption and EPR studies were prepared by mounting the final PSII membrane pellets directly onto the lucite sample holders. These specially designed sample holders were suitable to fit in the cryostat for each spectroscopic measurement. The sample holder had an internal compartment, with dimensions of 2.1 cm x 0.3 cm x 0.15 cm. The well for filling PSII membranes was formed by gluing a piece of mylar tape to one side of the lucite frame. The other open side directly faced the incoming X-ray beam. Chlorophyll concentrations in these samples ranged from 25-35 mg Chl/mL. Chlorophyll concentrations were determined by using the method described in Arnon (1949). Chlorophyll absorption was measured on an AVIV 14 DS spectrophotometer (AVIV, Lakewood, NJ) or on a Varian 2300 spectrophotometer (Varian, Houston, TX). The complete advance from the S_1 to S_2 state in these thick samples was accomplished by continuously illuminating the S_1 samples at 195 K or at 0°C when DCMU was added (See chapter III).

II.C.2. Preparation of the S-State Samples Induced by Flashes.

Different from the "thick" samples described above, which were able to build up the S_2 state by a long-time (~7 min) continuous illumination, the S_2 or higher S-state samples advanced by single flashes need to be saturable by the light sources (either a Xe lamp or a Nd-YAG laser). To guarantee a 100% saturation, these samples needed to be dilute and therefore in a liquid form. Unlike the "thick" samples, these liquid samples cannot be aligned vertically. A vertical alignment was possible only when the PSII suspension was filled into sample holders with an enclosed compartment. We had prepared these samples by sealing both open sides of the sample holders with Mylar tapes and injected PSII suspension into the sample compartment by a Hamilton syringe. The S/N of these samples were found to be only 50% compared with those which did not have a Mylar layer between the PSII surface and the incident X-ray beam. This was because the incident X-ray beam hit the Mylar surface and created large amount of scatters to our detector, and relatively decreased the S/N ratio of the samples. Hence most of the S-state samples illuminated by saturating flashes were prepared in lucite holders with open surface and aligned horizontally during the flash course (described in Set-up section).

Two different size sample holders were used in our flash study (chapter IV). The first (type 1) had the same dimension as described above for the thick samples. The second (type 2), with inner dimensions 1.5 cm x 0.3 cm x 0.08 cm, was ~50% thinner in the direction of the light path compared with the first type. The Xe lamp could saturate higher concentrations of the PSII membranes filled in the type 2 sample holders. The S/N of XAS was mainly determined by the concentration of the PSII membranes, not by the type of sample holders.

PSII-enriched membranes were resuspended in Medium A with 50% glycerol to a final Chl concentration of 4-5 mg/mL. PPBQ was added from a 50 mM stock solution (9.2 mg in 1 mL DMSO) into this PSII suspension to a final concentration of 500 μM. PPBQ (Eastman Kodak Company) had been crystallized from ethanol to obtain a satisfactory purity. Disposable syringes with teflon needles were used to load the PSII suspension to both types of sample holders. Typically the amount of PSII suspension was ~120 μL and ~50 μL for type 1 and type 2 sample holders, respectively.

All illuminations, EPR and X-ray absorption measurements were performed directly on the samples mounted in these holders. All of the samples were also rechecked by EPR measurements to monitor the possible damage induced by the intense X-ray beam produced from the synchrotron radiation source. Typically, less than 10% reduction of the MLS was found with the S_2 samples after being exposed to X-ray.

II.D. Experimental Set-up for S-States Flash-Induced by a Xe-Lamp.

Fig. II-1 is an illustration of the set-up used in the flash experiment. This set-up was designed for liquid samples with an open surface which needed to be aligned horizontally during the course of flashing at room temperature. The housing of the Xe lamp was supported by two lab jacks with its light output facing downward. A tapered light guide (made of Lucite) was placed beneath the lamp to direct the flash output to the sample surface. The light guide was designed to funnel the light intensity into the area of the sample surface (explained in Fig. II-2). The incident light hitting at the central area of the light guide would pass through the other end and directly absorbed by the sample (route a). However, that from the outer area would hit the wall of the light guide at first (point x), then would reflect back and forth but always be confined in the light guide due to total internal reflection (route b). The exit angle of route b has a very large scattering angle when it left the light guide. Therefore, the surface of the samples was kept as close as possible to the end of the light guide as long as the surface of the light guide would not contact the liquid sample. Typical distance between the end of the light guide and the sample surface was within 2 mm.

II.E. EPR Spectroscopy.

Low-temperature X-band EPR spectra were recorded using a Varian E109 EPR spectrometer equipped with a Model 102 microwave bridge. For the measurements of the

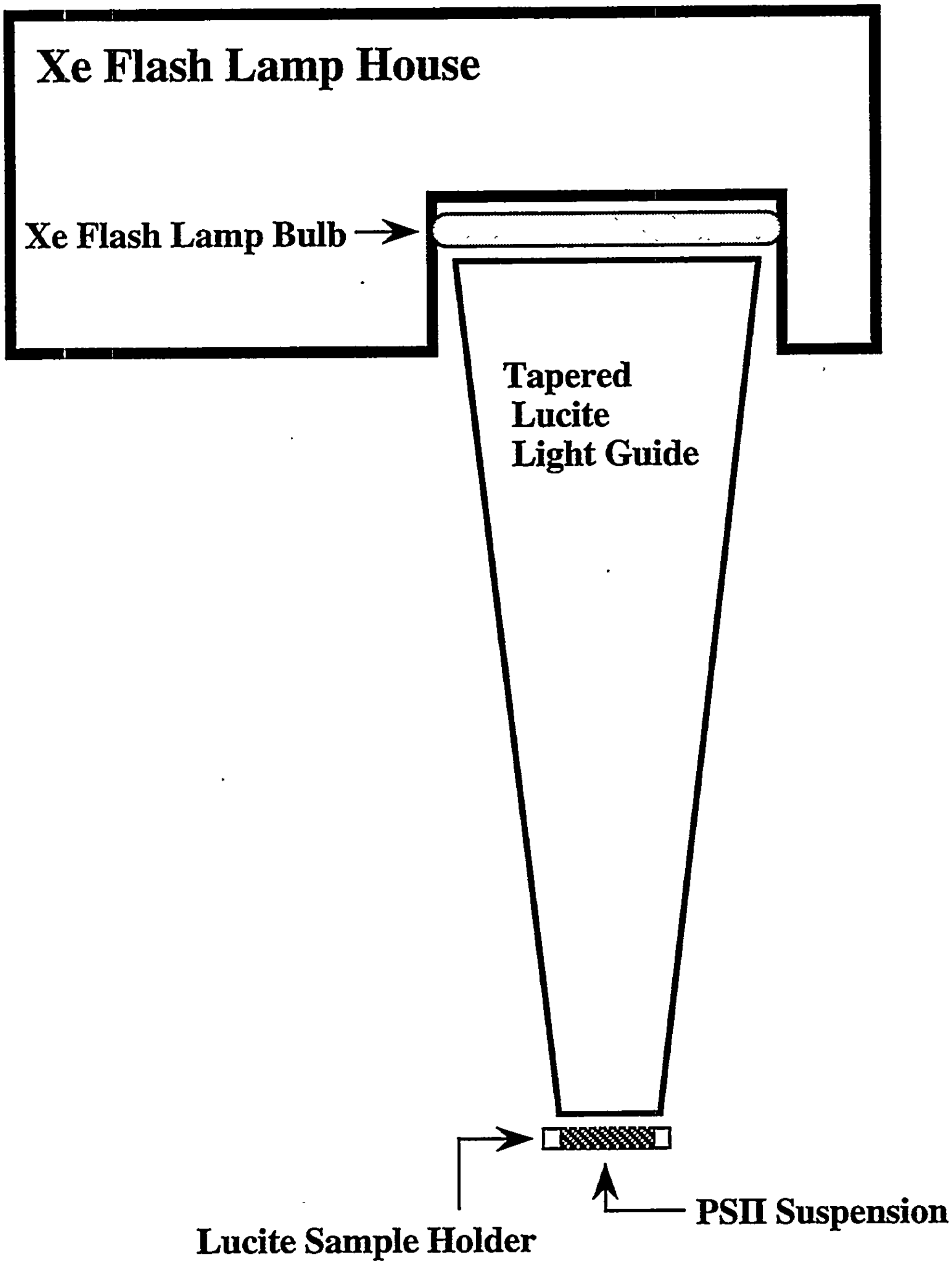

Fig. II-1. An illustration of the set-up used in the flash experiments. Samples were placed horizontally with the open side faced upward and close to the output of the light guide.

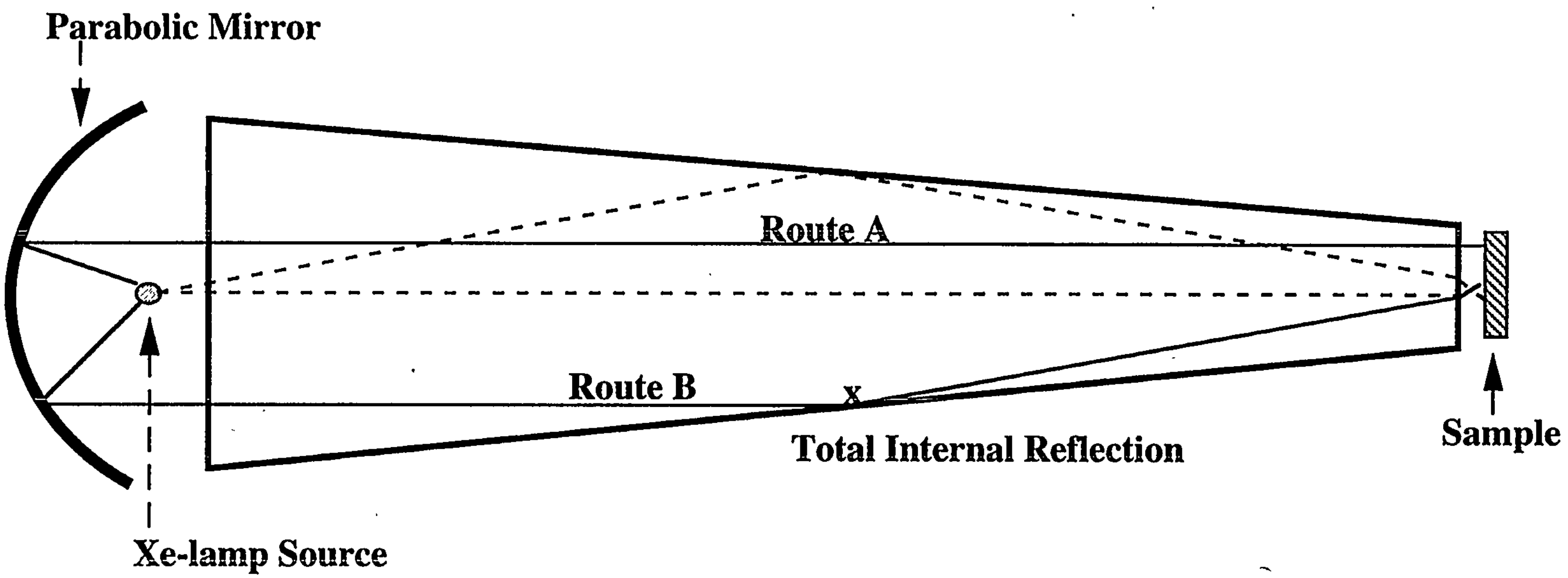

Fig. II-2 Schematic representation of the function of a light guide. the isotropic light radiation was constrained toward the sample direction by a parabolic mirror. Two representative routes reflected by the mirror are shown as Routes A and B. Two others representing direct rays are shown in dashed lines. The light guide helps to "guide" the output of the lamp to the sample surface by total internal reflection.

MLS and g≈4 signal, sample temperature was maintained at 8 K using an Air Products LTR liquid helium cryostat. Spectrometer conditions were as follows: microwave frequency, 9.21 GHz; field modulation amplitude, 3.2 mT at 100 *k*Hz; microwave power, 30 mW. EPR MLS amplitudes were quantitated by adding peak-to-trough amplitudes of three of the downfield and three of the upfield hyperfine lines, relative to g=2. Sample temperature was kept at 18 K for the measurements of the Y_D^+ signal, with the following spectrometer conditions: microwave frequency, 9.21 GHz; field modulation amplitude, 3.2 mT at 100 *k*Hz; microwave power, 1 μW.

II.F. X-ray Absorption Spectroscopy.

We use X-ray absorption spectroscopy (XAS) to study the structure of the Mn cluster in the OEC of PSII. Data are presented in Chapters III and IV. A brief description of the theory, data collection and data analysis will be described. Detailed discussions can be found in related articles referrenced in each section.

II.F.1. Why X-ray Absorption Spectroscopy?

First of all, I would like to take a moment to state why, among many spectroscopic techniques, we would use XAS as our main tool to probe the structure of the Mn cluster in OEC. The reasons are as follows:

1) XAS is element-specific. X-rays are absorbed by elements primarily through the photoelectric effect, i.e. when a bound electron is excited to a continuum state resulting in ionization by an incident photon. The threshold energy required for this transition is equal to the ionization energy of the bound electron and therefore is characteristic to each element. The K edge results from ionization of a 1*s* electron, while the L edges result

from ionization of 2*s* or 2*p* electrons. With a monochromator, we can tune the X-ray to the threshold energy of almost any element of interest. In biological systems, besides the metal cluster, there are protein backbones, other biomolecules , water and maybe other metals present as well. The use of XAS is especially beneficial because it provides a means to examine the structural environment of one metal without overwhelming interference from other elements.

2) XAS is a technique that yields structural characteristics from metallo-proteins without the need for samples to be single crystals. The crystal structure of many important metallo-proteins haven't been solved, including the OEC. Our samples are typically a frozen solution / suspension of PSII-enriched membranes.

3) The position and shape of the X-ray absorption near edge structure (XANES, approximately within 50 ev of the inflection edge) yields information about the electronic nature (oxidation state) and the geometrical arrangement of ligand atoms (symmetry) around the metal absorber. Extended X-ray absorption fine structure (EXAFS), referring to the oscillatory behavior in absorption coefficient in the region of the spectrum above the absorption edge, contains information about the numbers, types and distances of the neighboring atoms from the absorbers.

4) The availability of synchrotron radiation sources makes possible the examination of the active-site structures in metallo-proteins. The X-ray intensity emitted from synchrotron radiation sources is at least 5 orders of magnitude greater than conventional X-ray tubes. This development, as well as the improvement of the fluorescent detectors, makes it feasible to measure our dilute samples. Typical Mn concentration of our samples ranges from 0.8-0.08 mM depending on the type of experiments (See the sample preparation section above in this chapter).

II.F.2. General Introduction to EXAFS.

EXAFS spectra generally refer to the region 50-1000 ev above the absorption edge. The EXAFS oscillations occur in molecules or condensed phase. For isolated atoms, the absorption coefficient decreases monotonically as a function of energy beyond the edge. Elastic backscattering of the photoelectron from neighboring atoms results in the EXAFS oscillations. We can view this phenomenon in a more pictorial way by using a model of classical waves: scanning the photon energy through the EXAFS region causes the corresponding wavelength of the photoelectron to change. Hence, the peaks of the EXAFS oscillations form when the backscattering and outgoing photoelectron waves interfere constructively. On the other hand, the troughs happen at the energies where the backscattering and outgoing photoelectron waves interfere destructively.

The theory of EXAFS has been well developed in last 20 years. Although the first discovery of EXAFS was in the early 1930s (Kornig, 1931), the theoretical derivations of EXAFS were not reported until the early 1970s, using an expression based on single-scattering theory (Sayers, 1971; Sayers et al, 1974; Stern et al, 1975). Since then many good discussions on EXAFS theory have appeared (Eisenberger & Kincaid, 1978; Lee et al., 1981; Scott, 1984; Teo, 1986).

The EXAFS modulation of the absorption $\chi(k)$ is the sum of the sinusoidal oscillations from every backscattering atom. It can be described by the following equation:

$$\chi(k)=\frac{\Delta\mu(k)}{\mu_0(k)}=\sum_j\frac{N_j|f_j(k,\pi)|}{kR_j^2}e^{-2\sigma_j^2k^2}e^{-2R_j/\lambda(k)}\sin[2kR_j+\alpha_j(k)], \qquad (1)$$

where $\chi(k)$ is the normalized EXAFS spectrum as a function of k, $\Delta\mu(k)=\mu(k)-\mu_0(k)$, with $\mu(k)$ and $\mu_0(k)$ denoting the absorption coefficients of the element of interest with and without EXAFS modulation, respectively. N_j is the number of backscattering neighbors of type j for a given absorber atom (Mn) at a distance R_j, $|f_j(k,\pi)|$ is the backscattering amplitude of the jth atom and is a function of the atomic number of the backscattering element. The magnitude of the photoelectron wave vector is given by $k=[(2m_e/h^2)(E-E_0)]^{1/2}$, where m_e is the electron mass, E is the X-ray photon energy, E_0 is the threshold photoionization energy, and h is Planck's constant. The function $\alpha_j(k)$ can be considered as the phase shift that the photoelectron wave undergoes as it passes out of the absorber potential, through the scatterer potential, and back into the absorber potential. The Debye-Waller factor σ describes the attenuating effect resulting from thermal (assuming harmonic vibration) and static (assuming Gaussian pair distribution) disorder. $\lambda(k)$ is the photoelectron mean free path.

Eq. (1) reveals that each EXAFS wave is determined by the backscattering amplitude $N_j\,|f_j(k,\pi)|$, the damping factors $[e^{-2\sigma_j^2k^2}$ and $e^{-2R_j/\lambda(k)}]$, the $1/(kR_j^2)$ dependence, and the sinusoidal oscillation which is a function of distances $(2kR_j)$ and the phase shift $(\alpha_j(k))$. The effects of these components are as follows:

1) The backscattering amplitude function $|f_j(k,\pi)|$ and phase function α_j are characteristic to each backscatterers. Therefore these two functions can be used as indicators to identify different scattering atoms provided the atomic numbers are very different.

2) The sinusoidal oscillations contributed from each type of neighboring atom depend not only on the distances between the absorber-scatterer pairs, but also on the phase shifts.

3) Knowledge of the backscattering amplitude and phase functions is essential to go from the EXAFS data to distances R_j. For most elements they have been calculated and

tabulated using curved-wave single-scattering theory (McKale et al., 1988). These functions can also be derived experimentally from model compounds. Curve fitting analyses of EXAFS spectra using both tabulated and experimentally derived functions have provided accurate structural information (Powers, 1983; Teo, 1986).

4) The two exponential damping factors in Eq. (1) limit the detectable range of EXAFS to ~1000 eV above the edge. In many biological samples this range is even shorter as a result of poor signal-to-noise ratio or the presence of another absorbing edge. The Debye-Waller factor σ represents the fact that the atoms are not stationary, and this will smear out the EXAFS oscillations. The second exponential factor accounts for the photoelectrons which have suffered inelastic losses and will not have the proper wave vector to contribute to the interference process. The inelastic losses are due to excitation of the neighboring atoms or the intervening medium.

II.F.3. Data Collection.

X-ray absorption K-edge spectra were collected at beam line VII-3 and EXAFS spectra were collected at beam lines IV-2 and VI-2 at the Stanford Synchrotron Radiation Laboratory (SSRL); some EXAFS spectra in Chapter II and K-edge spectra in Chapter III were collected on beam line X9-A at the National Synchrotron Light Source (NSLS). Practical descriptions of the synchrotron radiation sources used in our study can be found in Guiles and McDermott's theses for the laboratory at SSRL (Guiles, 1988; McDermott, 1987) and in DeRose's thesis for that at NSLS (DeRose, 1990).

Fig. II-3 presents an instrumental set-up for XAS at the beamlines. Similar to any optical experiment, our set-up consists of the basic components including radiation source, monochromator, incident flux (I_0) measurement, a sample chamber and a detector.

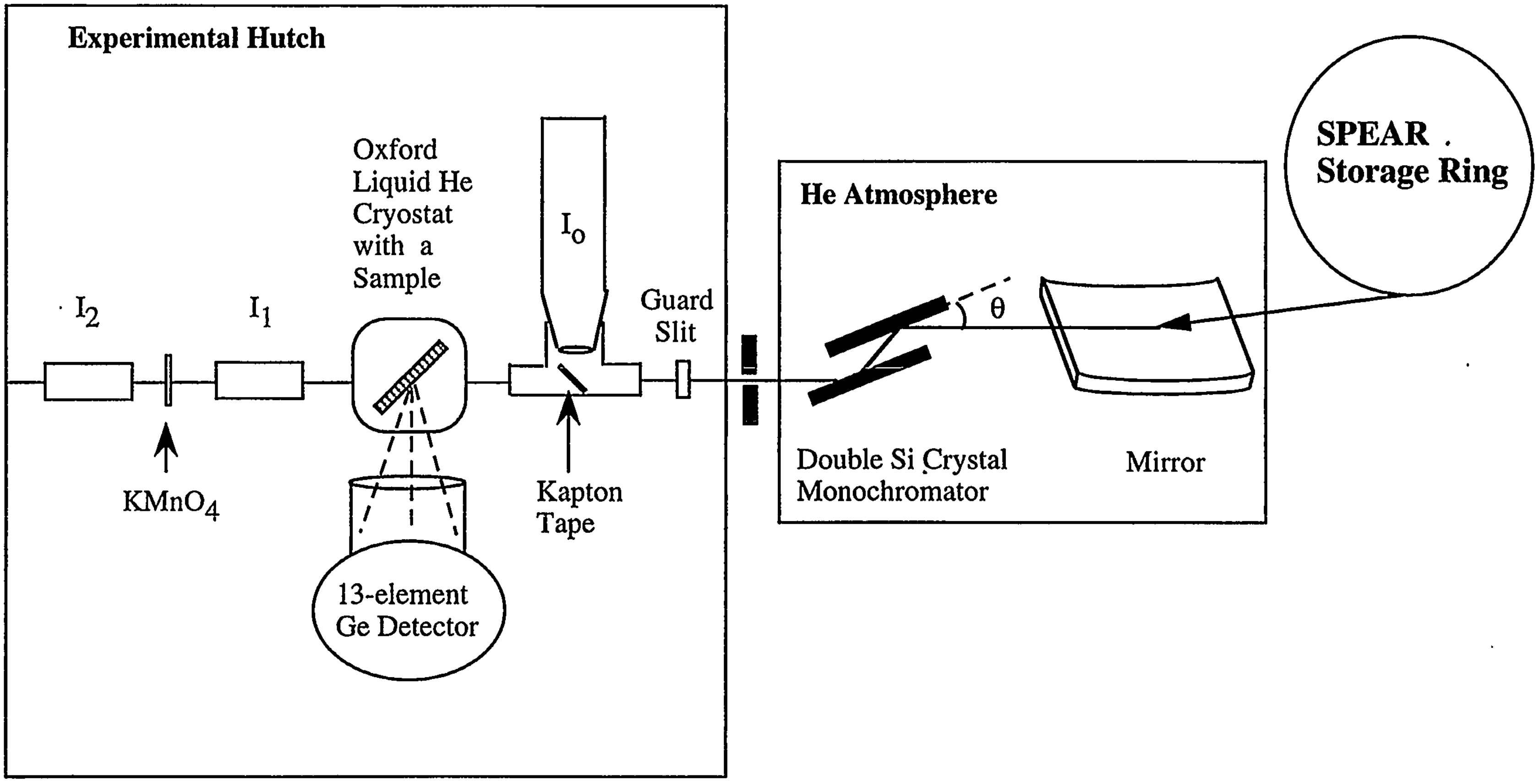

Fig. II-3 Experimental set-up (not drawn to scale) for fluorescence detection of x-ray absorption spectroscopy.

Sometimes a mirror upstream of the monochromator is used to focus the radiation to increase the beam intensity. However, because the X-ray beam is highly collimated, beam focusing degrades the energy resolution. Hence, this mirror is not used when we collect edge spectra which require higher resolution than the EXAFS spectra. Another function of this mirror is to reject higher-order harmonics by changing the grazing angle of the incident X-ray. At a certain angle, the fundamental is reflected towards the sample (due to total external reflection) while the higher harmonics will penetrate through the mirror and be absorbed or scattered away. Moreover, the metal coated on the mirror can absorb X-rays and therefore there is a "cut-off" energy for the X-rays after the mirror. The later two effects cause the mirror to be a good low pass filter.

X-ray beams are monochromatized by using Bragg reflection from a specific diffraction plane of a single crystal:

$$n\lambda = 2d \sin \theta, \qquad n=1,2,3.... \qquad (2)$$

where n is the order of the reflection, λ the wavelength of the diffracted X-ray, d the spacing of the crystal lattice planes and θ the angle between the Bragg planes and the incident ray. This monochromator diffracts the X-rays in much the same way as a diffraction grating does to visible radiation in optical spectroscopy, except the grating is provided by the spacing of the crystal lattice planes. A conventional two-crystal monochromator with fixed separation is used at SSRL. The incident beam is Bragg reflected from two flat crystals in sequence and the emergent beam is parallel to the incident beam (Fig. II-3). However, as the crystal angle is scanned during the data collection, θ changes correspondingly and the vertical position of the exit beam changes. Therefore, the table in the experimental hutch on which the experimental apparatus sits is controlled by a computer to track the beam exiting from the monochromator.

Si<220> double-crystal monochromators were used for all of the X-ray absorption measurements in this thesis based on the consideration of energy resolution and unwanted glitches (a sudden X-ray beam loss at some characteristic wavelengths due to the interference of another crystal plane(s) which diffracts the beam coincidently). Si<111> has the greatest output of the X-ray flux but the least resolution. The properties of Si<400> are exactly opposite to Si<111>. For EXAFS measurements which require less energy resolution but depend strongly on signal-to-noise ratio, Si<111> would be the best choice if not for the fact that many glitches exist in the Mn EXAFS region. On the other hand, Si<400> would be the best for the XANE experiments with its highest energy resolution. However, it has been found that Si<400> crystals are more prone to crystal heating, which affects the energy calibration (DeRose, 1990) and therefore the accuracy of our edge position. To use Si<220> is a good compromise, because it has better energy resolution than Si<111>, less flux attenuation than Si<400>, and no drawbacks as described above as found with either Si<111> or Si<400> crystals.

Another point worth mentioning is to reduce the X-ray harmonic content in the beam. These harmonics ($n \geq 2$ in Eq. (2)) are present with the fundemental frequency and are unwelcome because they can lead to distortions in the data (Scott, 1984). The harmonic content can be reduced at several locations. The first, as described above, is at the mirror before the monochromator. The second approach is at the selection of monochromator. For example, Si<111> crystals will not diffract even-order harmonics. However, this approach is not always suitable for a specific experiment, as described above for our project. The third method is to "detune" (slightly misalign the Bragg planes) the monochromator, which is done by rotating one crystal with respect to the other. This results in a drastic reduction of the harmonic to fundamental ratio with a small loss in total fundamental intensity. A typical harmonic-to-fundamental ratio measured at Beamline VII-3 is shown in Table II-2.

Table II-2. The Harmonic-to-Fundamental Ratio Measured at Beamling VII-3 at SSRL.

Percent Tuned (%)	Harmonic-to-Fundamental Ratio
100%	0.65
75%	0.18
50%	0.03

The harmonic-to-fundamental ratio reduces from 0.65 to 0.18 when the crystal is 25% detuned (75% tuned). Further detuning the monochromator to 50% decreases the ratio to 0.03. In this thesis, the second crystal was tuned to 50-75% of the maximum flux to reduce the transmission of the X-ray harmonics. The fourth approach which has recently been applied to our experiment uses a double mirror harmonic suppressor. This simple in-hutch mirror is able to reduce the harmonic content to an undetectable level and still maintains 53% of fundamental flux (Latimer et al., in press).

I_0 in our experiment is measured by using a piece of kapton to deflect a small part of the incident X-ray beam 90 degrees upward to a scintillation-photomultiplier tube. This "scattered" I_0 is measured under the similar mode as our sample detection (fluorescence detection, see below), and therefore is better at ratioing out the glitches than a regular ion chamber. The beam intensity after the sample (I_1) is measured by an ion chamber filled with nitrogen gas. To correct for possible monochromator drift during the scans, a small amount of the beam after I_1 is allowed to pass through a thin layer of $KMnO_4$ and into another ion chamber I_2. $KMnO_4$ is a suitable energy calibrant for our experiments because it has a narrow pre-edge (also known as the "white-line") feature at 6543.3 eV. In this manner, each scan of the sample is energy-calibrated simultaneously with data acquisition. All samples were maintained at 10 ± 1 K in an Oxford liquid helium cryostat.

X-ray absorption spectra were collected in fluorescence mode (Jaklevic et al., 1977). For most biological samples, because they are typically dilute, fluorescence detection is preferred. Fluorescence is detected using a Canberra Industries 13-element Ge solid-state detector as previously described (Cramer et al., 1988; DeRose, 1990). The fluorescence technique is most sensitive when paired with a detector with high energy resolution, like the solid-state detector. The ratio of fluorescence to scatter is maximum when the detector is positioned at right angle to the incident X-ray beam, with the sample at 45 degrees to both the incident beam and the detector. The fluorescence signal was recorded by setting the single-channel analyzer (SCA) window of each Ge element to the Mn Kα peak.

A modification of the detector set-up from a previous report (DeRose, 1990) is to assign different time constants (shaping time) to the shaping amplifiers of the 13 Ge elements according to their location on the detector surface. Conventionally, for the thick samples (~0.7 mM), the 13 amplifiers are set to have the same shaping time, which is convenient for us to set up windows to collect Mn Kα fluorescence on all 13 SCA's. However, for the thin, "flash-induced" samples (~0.08 mM), any method to improve the signal-to-noise of the Mn Kα fluorescence is valuable. Instead of using a universal shaping time for all of the 13 Ge elements, we use three "shells" according to the geometrical arrangement of the detector (Fig. II-4). This approach optimizes the results of our already dilute "thick" samples and is especially important to the even more dilute, "Flash-induced" samples (Chapter IV). The rationale is described in the following few paragraphs.

Photoreaction of an incident X-ray photon with a Ge element creates an input current pulse, with its area propotional to the X-ray energy. A shaping amplifier converts each input current pulse to a uniform Gaussian-shape pulse with its height (in Voltage) propotional to the X-ray energy. The shaping time is the time constant in which each incoming current pulse is allowed to be "shaped" to the Gaussian-shape pulse. Each shaping amplifier is equipped with a few options of time constants. A longer shaping time results in a better "shaped" output pulse, and therefore achieves a better energy resolution. However, this means that fewer input pulses can be processed in a unit time, so fewer fluorescence counts can be collected. Shortening the shaping time can accommodate more counts, but worsens the energy resolution. Thus, there is a tradeoff between "maximum

(a) Thick Samples:

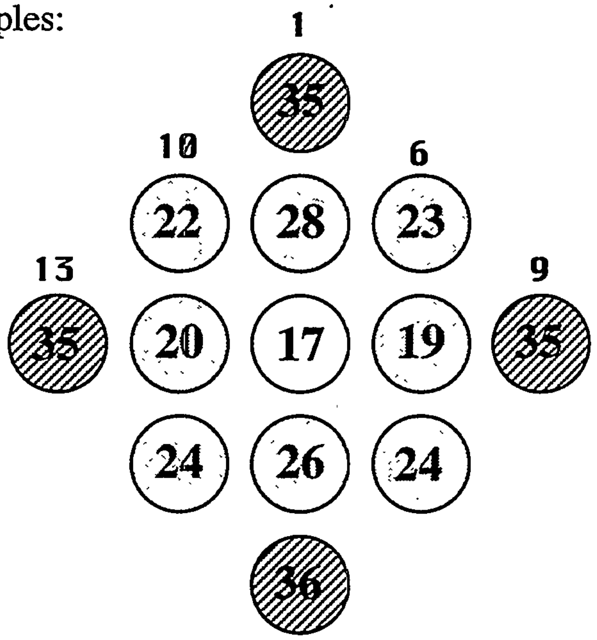

(b) Thin Samples:

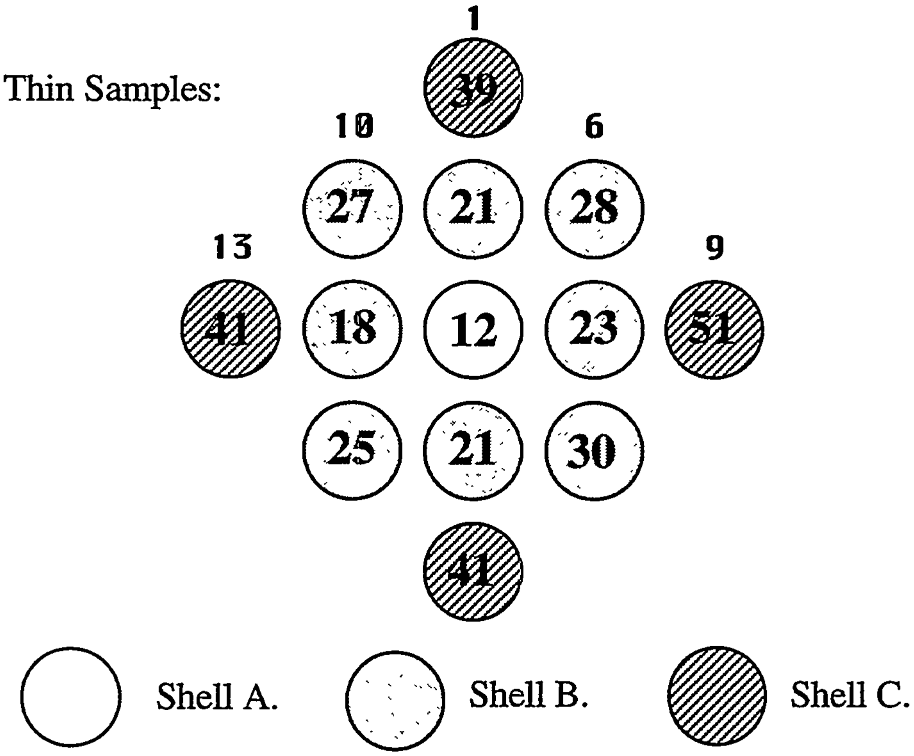

Fig. II-4 Graphic layouts (as seen when facing the detector) of the 13 elements of the Ge detector with the total ICR's (in kilo counts per second) shown inside each element for the (a) regular "thick" and (b) flash-induced, "thin" samples. Elements are numbered for clarity (as shown above each column).

fluorescence counts" and "best energy resolution" that one has to judge according to the experimental objectives.

The total counts entering at each Ge element contain both fluorescence and scattered photons. In our samples, most counts seen by the detector are from the scattered photons. For example, the total incident count rate (ICR) to the shaping amplifier from the central channel is approximately 12-18 kilo counts per second (cps) for both types of samples. However, for a typical flash-induced sample, the fluorescence counts after energy discriminator are only 200-300 cps, which amounts to approximately 1.6 % of the total ICR. This ratio is even worse for the outer channels (shell B and C). Fig. II-4 presents the typical ICR's of the 13 Ge elements from both the "thick" and "thin" samples.

Ideally, to get the maximum fluorescence counts we would like to (a) collect as many total counts as possible, then (b) use good energy discriminating devices to separate the Mn fluorescence Kα peak (at ~ 5.9 KeV) from the scatter peak (from 6.4 - 7.1 KeV). Part (b) is not a problem because good energy discriminators (SCAs) are available, and they work in a very satisfactory manner. However, part (a) is restricted because the response of the electronics associated with the shaping amplifiers is not linear indefinitely. In other words, when the ICR is over a threshold value, the shaping amplifier will be saturated.

The threshold values of the ICR are characteristic with the shaping time constants assigned to each amplifier. Fig. II-5 describes the relation of the input (ICR) and the output flux (AMP_{out}) after a shaping amplifier (Element # 4, shell B) when the amplifier is set to shaping time constants of 0.5, 0.75, 1.0 or 2.0 μs. The amplifier loses its linearity faster as the shaping time constant increases. The critical counts before the amplifier saturated are approximately 45, 33, 23 and 17 kilo cps when the time constants are set to be 0.5, 0.75, 1.0 and 2.0 μs, respectively.

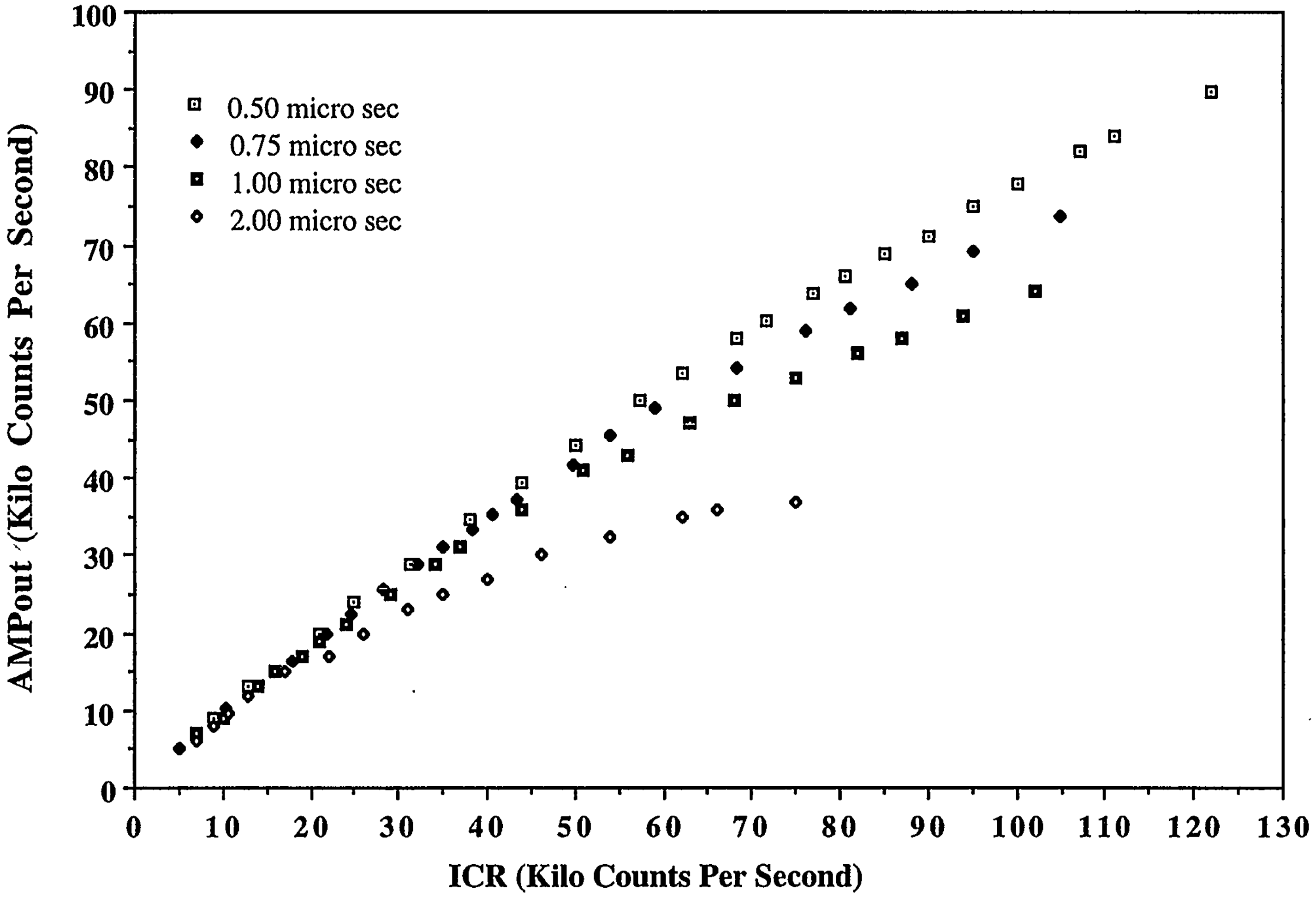

Fig. II-5. Extent of linearility of the shaping amplifier (AMPout to ICR) at various time constants. Data were obtained from element #4 of the Ge detector at Beamline VII-3 at SSRL.

Therefore, we use an approach which is at an intermediate position with respect to both energy resolution and fluorescence counts -- to set the shaping time of the 13 amplifiers into 3 shells (Fig II-4). The central element (shell A) contains the most fluorescent counts and the lowest ICR; therefore the shaping time is set to be 1.0 μs to obtain best energy resolution. The total count rate on this element is limited to less than 20 kHz. For elements in shell B, with smaller fluorescence-to-scatter ratio, the total count rates during the measurements are maintained at less than 30 kHz and the amplifier shaping time is 0.75 μs. For the outer elements (shell C), which will be saturated easiest with the highest scatter photons, the total count rate is approximately 40 kHz and the shaping time constant is shortest (0.5 μs) to collect more fluorescence counts.

In our "thin" samples, sometimes we found it is worthwhile to sacrifice one element in shell C (to have it saturated) to collect more counts in the rest of the elements. As shown in Fig. II-4, one element (#9) received 51 kcps but the other 3 elements of shell C were able to be maintained below the threshold cps.

With a shaping time of 1.0 μs, the resolution of each element is approximately 250 eV. Each EXAFS spectrum contained 344 points, with higher point density around the pre-edge region (0.25 eV/point) for better $KMnO_4$ energy referencing. Typical scans were collected from 150 eV below to 560 eV above the edge and required about 40 min.

An unfocused X-ray beam, with about 1 eV energy resolution, was used for edge studies. Energy calibration was performed simultaneously as described above. The slit in front of the I_0 detector was closed to a vertical size of 1 mm. The full-width-half-maximum of the $KMnO_4$ "white-line" was 1.6 ± 0.1 eV. Typical edge spectra were recorded by scanning from about 40 eV below to 50 eV above the edge. The point density was 5/eV. Each spectrum contained 401 points and required about 20 min to collect. At least 5 edge scans were averaged for each sample.

The inflection energies reported in Chapters III and IV were obtained from the zero-crossing points of the second derivatives generated by analytical differentiation of a third-order polynomial fit to the data over an interval of ± 3.0 eV on each side of a data point. The uncertainty in the inflection point energy is ± 0.1 eV.

II.F.4 XAS Data Analysis.

The data were analyzed as described in detail elsewhere (Teo, 1986; Guiles et al., 1990; DeRose, 1990). The analysis programs for EXAFS and XANE data were described in the theses of Goodin (1983) and Guiles (1988). A brief outline follows: A routine EXAFS analysis can be separated to three parts:

Part 1. Data reduction from μ(E) to $\chi(k)$. This part includes the procedures to convert the experimentally measured abosorption spectra in energy space to the interference function $\chi(k)$ in k-space. Each raw scan was devided point-by-point by I_0 according to the following equation:

$$\mu(E)\alpha\frac{F}{I_0}\ , \qquad (3)$$

Bad scans (usually due to beam loss or irreproducible glitches) were removed after carefully examining the data. Each individual scan then was weighted and added as described elsewhere (Yachandra, 1994). After addition, a linear function was fit to the pre-edge background and subtracted from the data. For some data in Chapter IV, a Gaussian-tail-shaped background was used due to a more serious scattering background in the dilute samples. The data then were normalized to a unit absorption amplitude which was defined by the intersection point between a second-order polynominal fit to the data after the edge and a vertical line at the maximum absorption edge. The next step is to divide these normalized data by the free atom absorption ($\mu_0(k)$) according to Eq. (1). For data presented in this thesis, tabulated numbers for free atom absorption were used (McMaster et al., 1969).

$\chi(k)$ was obtained by converting the data from a function of energy E to a function of photoelectron wave vector k by the equation $k=[(2m_e/h^2)(E-E_0)]^{1/2}$. The next step is to multiply $\chi(k)$ by k^3 to counteract the EXAFS attenuation due to the factor of $1/k$ in Eq. (1) and roughly the $1/k^2$ behavior of $|f_j(k,\pi)|$ at large values of k. This k^3weighting prevents the low-k oscillations from dominating the smaller ones at high k, and hence allows us to better examine heavy scatterers (e.g. metallic neighbors) which peak at higher k region than the light ones.

The last step is to further remove the residual background over the k range, especially at higher k regions where the background has been amplified by k^3 weighting. A good method is to fit $k^3\chi(k)$ with a polynomial spline using a least-squares procedure. The spline function divides the EXAFS region into a specific number of domains and a given order of polynomial function is fit within each domain. The ends of the intervals are tied together and limited to have equal value and slope. Splines with 2-4 domains and a third-order polynomial function are used. The spline is a very flexible function, and it can readily remove the low-frequency background components without affecting the higher frequency EXAFS oscillations. The background-removing effect is evaluated by coupling the spline procedure with Fourier transformation. The background contribution usually peaks at apparent distance (R') less than 1 Å in the Fourier transform spectra (See *Part 2*). This inspection usually provides insight for improvement of background removal or further data analyses.

Part 2. Fourier transform and filtering. This part prepares the "isolated-shell(s)" for our fitting routine. Fourier transformation of the EXAFS data from wave-vector-space to distance-space provides a simple physical picture of the local structure around the Mn absorber. Back-scattered waves with various frequencies contributing to $k^3\chi(k)$ will be presented in the form of distances from the backscatterers to the Mn absorber after Fourier transformation. Typically, a finite k range from k_{min}~3.5 Å^{-1} to k_{max}~12.0 Å^{-1} is used. Data before 3.5 Å^{-1} are discarded because contributions from multiple scattering become important and therefore Eq. (1) (based on a single-scattering description of EXAFS) is invalid. For our samples, the EXAFS at $k \geq 12.0$ Å^{-1} are interfered by the Fe edge. k_{min} and k_{max} should be carefully chosen to have $\chi(k)$ values close to zero to reduce truncation effects.

In practice, applyig the curve-fitting technique to the raw data is difficult because of the noise and the large number of parameters required in the data. Therefore, a technique named Fourier filtering is usually used before curve-fitting. First, the distance range of peak(s) of interest from Fourier transforms is selected. Then, a general Hamming window with smooth boundaries is applied to the selected peaks, and the data within the window are back transformed to k space. The resulting isolated shell(s) then can be fit without the contamination of high frequency noise or the residual background.

Part 3. Curve-fitting. Curve-fitting is the main technique used to extract the structural information from the EXAFS data. The isolated shell(s) from the EXAFS data were fit using Eq. (1) with theoretical values for the backscattering amplitudes and phase shifts for the scattering-absorbing pairs, based on the curved-wave formalism of McKale et al. (1988). In this work the Debye-Waller parameters were allowed to vary over a range comparable with those derived from multinuclear Mn compounds. The energy of the absorption edge (E_0) was varied in simulations to allow better phase matching to the experimental waves. The parameter E was allowed to change ± 20 eV from E_0, which was the energy at maximum peak height of the Mn K edge. The values of the average distance R_j, the numbers of scattering atoms N_j at distance R_j, the Debye-Waller factor σ_j and the threshold energy E_0 were simultaneously fit with a nonlinear least-squares fitting program (Goodin, 1983; Guiles, 1988). Other details of the curve-fitting technique or more general data analysis methods are available (Teo, 1986; Yachandra, 1995).

II.G. Reference.

Arnon, D. I. (1949) *Plant Physiol.* 24, 1

Berthold, D. A., Babcock, G. T., & Yocum, C. F. (1981) *FEBS Lett. 134,* 231

Eisenberger, P., & Kincaid, B. M. (1978) *Science 200*, 1441

Goodin, D. (1983) *Ph. D. Dissertation*, University of California-Berkeley, CA Lawrence Berkeley Laboratory Report LBL-16901.

Guiles, R. D. (1988) *Ph. D. Dissertation*, University of California-Berkeley, CA Lawrence Berkeley Laboratory Report LBL-25186.

Latimer, M. J., Rompel, A., Underwood, J. H., Yachandra, V. K. & Klein, M. P. (1995) *Rev. Sci. Instrum.* In press.

Lee, P. A., Citrin, P. H., Eisenberger, P., & Kincaid, B. M. (1981) *Rev. Mod. Phys. 53*, 769

Kronig, R. deL. (1931) *Z. Phys. 70*, 317

Kronig, R. deL. (1932) *Z. Phys. 75,* 191, 468

Kuwabara, T. & Murata., N. (1982) *Plant Cell Physiol. 23*, 533

McMaster, W. H., Kerr Del Grande, N., Mallet, J. H. & Hubbel, J. H. (1969) in *Compilation of X-ray Cross Sections* , Lawrence Radiation Laboratory.

McKale, A. G., Veal, B. W., Paulikas, A. P., Chan, S.-K., & Knapp, G. S. (1988) *J. Am. Chem. Soc. 110*, 3763

Power, L. (1983) *Biochim. Biophys. Acta 683*, 1

Sayers, D. E. (1971) Ph.D. Dissertation, University of Washington.

Sayers, D. E., Lytle, F. W., & Stern, E. A. (1974) *In "Amorphous and Liquid Semiconductors," Proc. 5th Int. Conf. Amorph. Liq. Semicond.* (J. Stuke & W. Brenig, eds.), pp. 403-412. Taylor & Francis, London.

Scott, R. A. (1984) In *"Structural and Resonance Techniques in Biological Research"*

(D. L. Rousseau ed.), pp. 295-362. Academic Press, Orlando, Fl.

Stern, E. A., Sayers, D. E., & Lytle, F. W. (1975) *Phys. Rev. B 11*, 4836

Teo, B. K. (1986) *Inorg. Chem. Concepts, 9* (Jorgensen et al. eds.) Springer-Verlag, New York.

Yachandra, V. K. (1995) *Methods in Enzymology*, (K. Sauer, ed.), pp. 638-675, Vol. 246, Chapter 26, Academic Press, Orlando, Fl.

Chapter III. Correlation between Structure and Magnetic Spin State of the Mn Cluster in the Oxygen-Evolving Complex of Photosystem II in the S_2 State: Determination by X-ray Absorption Spectroscopy

III.A. Introduction: The MLS and the g≈4 EPR Signals.

Two low-temperature electron paramagnetic resonance (EPR) signals have been assigned to the Mn cluster in the S_2 state: the multiline signal (MLS) and the g≈4 signal.

The MLS was the first spectroscopic evidence of the involvement of the Mn atoms in active, oxygen-evolving PSII complexes. This signal was first observed in broken spinach chloroplasts which had been quickly quenched to 133 K following a flash at room temperature (Dismukes & Siderer, 1981; Hansson & Andréasson, 1982). A period-of-four oscillation pattern was found in the study of the dependence of the MLS on flash number. The amplitude of the MLS was maximal on the first flash and again on the fifth flash. Therefore, this signal was assigned to the S_2 state.

Continuous illumination of the dark-adapted PSII membranes (the S_1 state) could also generate this MLS, provided only one electron was allowed to transfer from the OEC to the acceptor side. This could be done by blocking the electron transfer from Q_A^- to Q_B, via two commonly used protocols. The first built up the MLS by continuously illuminating the S_1 sample at 195K. At this temperature the electron transfer from Q_A^- to Q_B is prohibited. The second method to accumulate the MLS was illuminating DCMU-treated PSII at room temperature. DCMU is a herbicide which binds at the Q_B site much more strongly than a native Q_B molecule and therefore inhibits electron transfer from Q_A^-

to Q_B by competing with plastoquinone for the Q_B site. In this chapter, the first method was used.

Centered at g=2, the MLS spanned a magnetic field range of 150-180 mT and exhibited at least 18 partially resolved hyperfine lines at X-band (~9 GHz). Anisotropy was observed with the MLS at both X-band and S-band (~3.9 GHz) EPR measurements (Kim et al., 1992; Haddy et al., 1989). Particularly at the S-band, a significant hyperfine anisotropy was found and attributed to the cause of the "non-resolvable" hyperfine lines. A variety of di-μ-oxo bridged Mn(III,IV) binuclear complexes had also been found to contain 16 hyperfine lines at X-band. This similarity suggested the Mn cluster responsible for oxygen-evolving activity was an exchange-coupled complex of at least two Mn atoms (Dismukes & Siderer, 1981; Hansson & Andréasson, 1982).

The g≈4 EPR signal was first discovered in PSII samples which were continuously illuminated at 140 K (Casey & Sauer, 1984; Zimmermann & Rutherford, 1984). This signal was centered at g≈4 with a peak-to-trough separation of 32-36 mT (denoted S_2-g4 signal) and did not exhibit resolved hyperfine features except under certain conditions (see below.). Similar to the MLS, this g≈4 signal was destroyed by treatment that removed Mn. It was originally attributed to an electron transfer intermediate between the Mn cluster and $P680^+$ (Casey & Sauer, 1984; Zimmermann & Rutherford, 1984). This signal was reassigned to be an alternative form of the S_2 state, once the amplitude of the g≈4 signal was found to follow the period-of-four oscillation pattern and was maximum following the first and fifth flashes (Zimmermann & Rutherford, 1986).

This assignment was further supported by an X-ray absorption edge spectroscopy study. Formation of the g≈4 EPR signal was associated with a shift of the Mn K-edge which was similar to that observed upon formation of the MLS from the S_1 state (Cole et al., 1987). This S_2-g4 signal, like the MLS, had been shown to arise from an active form of the Mn cluster, based on similar ability to convert the S_2 to the S_3 state and ultimately produce oxygen (Ono et al., 1987; Andréasson et al., 1990; Haddy et al., 1990).

The origin of the S_2-g4 signal has been of great interest ever since it was first discovered. Although the native g≈4 EPR signal lacked resolved hyperfine lines, the existence of underlying hyperfine structure was still predicted because the signal was not appreciably narrower at S-band than at X-band (Haddy et al., 1992). This ambiguity inspired the search and discussion for various models to explain both the MLS and the S_2-g4 signal.

One model attributed these signals to two different conformations of a tetranuclear Mn cluster with different spin states. An alternate model involved a redox equilibrium between a monomeric Mn(IV) and a mixed-valence dimer (Hansson et al, 1987; Aasa et al., 1987) or trimer (Pecoraro, 1988; Kessissoglou et al., 1989, Li et al., 1988). This was based on studies on the monomeric Mn(IV) model compounds which were able to exhibit a g≈4 EPR signal. The third model suggested that the MLS and the S_2-g4 signal may originate from two different conformations of a trinuclear Mn cluster. In this model, the fourth, EPR-silent Mn atom was located some distance away and could aid as an electron transfer intermediate between the trimer and Y_Z^+ (Kessissoglou et al., 1989; Li et al, 1988). This model was supported by the studies on trimeric Mn compounds: some trinuclear Mn complexes could give rise to EPR signals that were similar to the MLS and S_2-g4 signal.

A conclusive assignment of the S_2-g4 signal was not achieved until the observation of hyperfine structure on the g≈4 EPR signal in oriented ammonia-treated samples (Kim et al., 1990). At least 16 Mn hyperfine lines were resolved. The number of the hyperfine lines and their spacing ruled out the possibility of a monomeric Mn(IV) to be an origin of the S_2-g4 signal. Although the model which suggested that both of the S_2 signals arise from a trimer connot be excluded at present, a tetranuclear origin of the MLS is favored on theoretical ground (Bonvoisin et al., 1992, Brudvig, 1989).

Moreover, recent EPR measurements strongly support a model in which the S_2-g4 and S_2-MLS arise from different spin-state configurations of an exchange-coupled tetranuclear Mn complex (Kim et al., 1992). It is known that the MLS originates from the S=1/2 ground state (Britt et al., 1989). On the other hand, multifrequency EPR studies provide evidence that the S_2-g4 signal originates from the middle Kramer's doublet of a near rhombic S=5/2 state (Haddy et al., 1992).

The relative amplitude of the two S_2 EPR signals is sensitive to a variety of experimental conditions. In samples illuminated at 200 K, both signals are observed in the presence of sucrose; while with glycerol, ethylene glycol or ethanol, only the MLS appears (Zimmermann & Rutherford, 1986; De Paula et al., 1987). However, at lower illumination temperature (130-140 K), the S_2-g4 EPR signal appears predominantly regardless of which cryoprotectant is used. Table III-1 summarizes the effects of temperature and cryoprotectent on these two S_2 EPR signals generated by continuous illumination at low temperature.

Annealing the S_2-g4 samples to 200 K in the dark generates more MLS at the expense of the $g \approx 4$ EPR signal (Casey & Sauer, 1984). Based on the observation of the amplitude conversion of the S_2-g4 to S_2-MLS, the two species characterized by the two S_2 signals have been proposed to be interrelated (Zimmermann & Rutherford, 1986; Beck & Brudvig, 1986; Hansson et al., 1987). PSII preparations treated with NH_3, F^-, NO_3^-, I^- or when Ca^{2+} is replaced by Sr^{2+} have been reported to show an enhanced S_2-g4 signal

Table III-1 The Effects of Temperature and Cryoprotectent on the MLS and S_2-g4 Signals Generated by Continuous Illumination at Low Temperature.

	Temperature	MLS	g=4
Sucrose, 0.4 M	200 K	yes	yes
	140 K	no	yes
Glycerol, 50%	200 K	yes	no
	140 K	no	yes
Ethylene Glycol 30%	200 K	yes	no
	140 K	no	yes
Ethanol, 5%	200 K	yes	no

(Casey & Sauer; 1984; Beck & Brudvig, 1986; Ono et al., 1987; Beck & Brudvig, 1988; Boussac & Rutherford, 1988; Ono & Inoue, 1989; DeRose, 1990).

Not all of the S_2-g4 signals mentioned above have the same line width and g-value. Treatment with ammonia not only induces the resolution of at least 16 hyperfine lines on the $g \approx 4$ EPR signal, but also shifts the $g \approx 4.1$ signal to $g \approx 4.2$, narrows the signal to approximately 300 Gauss, and increases the signal amplitude (Kim et al., 1992; Beck & Brudvig, 1986,1988). Substitution of F^- for Cl^- has been reported to narrow the $g \approx 4$ signal and increase its amplitude relative to that of the MLS (Casey & Sauer, 1984; Beck & Brudvig, 1988; Ono et al., 1987). The similar amplitude increase with the $g \approx 4$ EPR signal have also been detected in the following treatments: when the Cl^- is replaced by NO_3^-, I^- or methylamine (Ono et al., 1987; Beck & Brudvig, 1988); and when Ca^{2+} is replaced by Sr^{2+} (Boussac & Rutherford, 1988; Ono & Inoue, 1989).

Investigation of the coordination chemistry of the Mn cluster is important to understand better the catalytic mechanism of water oxidation. We have used X-ray absorption spectroscopy to study the local structure of the Mn cluster in the OEC. Observation of a positive shift in the Mn X-ray K-edge energy provided direct evidence for the oxidation of Mn accompanying the S_1 to S_2-MLS transition (Goodin et al., 1984). Similar conclusions were reported based on the Mn K-edge study of the S_2-g4 samples measured at 170 K (Cole et al., 1987).

Extended X-ray absorption fine structure (EXAFS) studies provide further information about the types of ligands, the Mn-to-ligand distances and the coordination number of the Mn cluster (Yachandra et al., 1987). Extensive EXAFS studies have been performed to characterize the S_2-MLS and S_1 samples (DeRose, 1990; Penner-Hahn et al., 1990; Sauer et al., 1992; MacLachlan et al., 1992; Yachandra et al., 1993).

However, no EXAFS studies on the S_2-g4 samples, either from native or treated PSII preparations are available. The observation that at 130-140 K the native g≈4 EPR signal was generated predominantly, but converted to the MLS signal upon annealing at 200 K, has led to the suggestion that the molecular configuration of the Mn cluster in the S_2-g4 state is closer to that in the dark-adapted S_1 state (de Paula et al., 1987).

In this chapter I present the results of Mn K-edge and EXAFS experiments performed on native PSII samples poised predominantly in the S_2-g4 state by illumination at 130 K. The X-ray absorption data presented here are of significantly improved quality compared with the Mn K-edges we reported earlier for the S_2-g4 samples (Cole et al., 1987), due mainly to the use of a 13-element Ge fluorescence detector and data collection at 10 K. Results presented here confirm our previous study of the S_2-g4 samples, indicating the oxidation of Mn in the advance from the S_1 to the S_2-g4 state. However, comparing the S_2-g4 and S_2-MLS samples, differences in the edge position and shape are now detected.

Furthermore, the EXAFS analyses surprisingly showed an altered molecular configuration of the Mn cluster in the S_2-g4 state relative to that of both the S_1 and S_2-MLS states. This is unexpected, because our previous EXAFS results showed that the structure of the Mn cluster in the OEC remained substantially unchanged during the S_1 to S_2-MLS transition (DeRose, 1990; Sauer et al., 1992). Unlike the S_1 or S_2-MLS state, both the second and third shells of the Mn backscatterers in the S_2-g4 state contain an increased heterogeneity. Conclusions are drawn from a detailed comparison of the simulation results obtained from the S_1, S_2-MLS, S_2-g4 and S_2-ann. (S_2-ann., the S_2-g4 samples annealed in the dark at 200 K, which produces the S_2-MLS spectrum) samples. The significance of these analyses and models for the Mn cluster of the OEC are discussed.

III.B. Materials and Methods

III.B.1. Preparation of PSII Membranes.

Oxygen-evolving PSII membranes from spinach were prepared using Type 1 protocol as described in section II.A.1 of Chapter II, with typical oxygen-evolving activity of 500-600 µmol of O_2/mg Chl/h. The PSII membrane pellets were washed in medium A with 50% glycerol as the cryoprotectant and centrifuged again. Chemical oxidation of cytochrome b_{559} was accomplished by incubating PSII membranes suspended at 3 mg Chl/mL in the dark for 10 min at 4°C in medium A with 5 mM $K_3W(CN)_8$ / $K_4W(CN)_8$, and then washed and centrifuged as above. The samples for X-ray absorption studies were prepared by mounting these PSII membrane pellets directly onto the lucite sample holders, with a hollowed compartment (dimensions 2.1 cm x 0.3 cm x 0.15 cm) backed by a piece of mylar tape. The open side directly faced the incoming X-ray beam. All illuminations, EPR and X-ray absorption measurements were performed directly on samples mounted in these holders. Chlorophyll concentrations in these samples ranged from 20-25 mg Chl/mL.

III.B.2. Illumination.

Samples prepared as described above were kept in the dark for 2 h at 4°C to poise the PSII membranes in the S_1 state, then frozen in liquid nitrogen. Prior to illumination, samples were equilibrated for 2 min in an unsilvered dewar at 131 ± 3 K (for the S_2-g4 state) or 200 K (for the S_2-MLS state). Samples were continuously illuminated for 7 min using a 400 W tungsten lamp, with a 7-cm path of 5% aqueous $CuSO_4$ as a heat filter. Temperature was maintained at 195 K in a dry ice/methanol bath or at 131 ± 3 K with a continuous stream of liquid nitrogen-cooled nitrogen gas. The temperature was monitored throughout the illumination period with a copper-constantan thermocouple. The S_2-ann.

samples were generated by warming (annealing) the S_2-g4 samples to 200 K in the dark for 90 s, then frozen in liquid nitrogen within 2 sec.

III.B.3. Q_A^- Signal Quantitation.

The amount of Q_A^- signal from each EPR spectrum was estimated by the following equation:

$$q'=b'-a'(b/a)$$

where b' is the peak-to-trough amplitude of a MLS hyperfine peak located in the Q_A^- region (between 330-350 mT in Fig. III-1); a' is the amplitude of a second MLS peak at lower field than the g=2 region (between 270-290 mT in Fig. III-1), where no Q_A^- or other EPR signal is present. b and a, measured from a flash-induced S_2 state, are the amplitudes of the two MLS hyperfine peaks located at the same magnetic field with respect to b' and a'. This flash-induced S_2 state was generated at room temperature using either a xenon lamp or a Nd-YAG laser. At room temperature, the electron transfer from Q_A to Q_B is not blocked and therefore no Q_A^- signal is produced. q' is the amplitude of Q_A^- before normalization. Both the MLS and Q_A^- (q) amplitudes were normalized to correct for variable sample concentrations and volume. All spectra were quantitated from the light-minus-dark difference spectra.

III.B.4. X-ray Absorption Measurements.

X-ray absorption K-edge spectra were collected at beam line VII-3, and EXAFS spectra were collected at beam lines IV-2 and VI-2 at the Stanford Synchrotron Radiation Laboratory (SSRL); some EXAFS spectra were collected on beam line X9-A at the National Synchrotron Light Source (NSLS). Si<220> double-crystal monochromators were used for all of the X-ray absorption measurements. The second crystal was detuned to 75% of the maximum flux to reduce the transmission of the X-ray harmonics. All samples were maintained at 10 ± 1 K in an Oxford liquid helium cryostat. To ensure sample integrity EPR spectra were recorded after X-ray measurements. X-ray absorption spectra were collected in fluorescence mode (Jaklevic et al., 1977), using a Canberra Industries 13-element Ge solid-state detector, as described in Chapter II.

The inflection energies from the XANE spectra were obtained from the zero-crossing points of the second derivatives generated by analytical differentiation of a third-order polynomial fit to the data over an interval of ± 3.0 eV on each side of a data point. The uncertainty in the inflection point energy is ± 0.1 eV. These values are different from those previously reported by our group. This is because the signal-to-noise ratio in our earlier data was lower, thus we reported the maxima of the (symmetric) peak of the first derivative obtained from a second-order polynomial sliding fit to the edge spectra as the edge positions (Yachandra et al., 1987; Cole et al., 1987; Guiles et al., 1990). Recently, with much improved signal-to-noise ratio, our present data require less smoothing and thus retain more structures on the absorption edge. This results in a clearly asymmetric peak shape in the first derivative and therefore it is not suitable to report the maximum as the edge position.

The Mn EXAFS data from PSII samples were fit with theoretical values for the backscattering amplitude and phase shifts for the scattering-absorbing pairs, based on the curved-wave formalism of McKale et al. (1988).

III.C. Results.

III.C.1 EPR Spectroscopy.

Fig. III-1 shows the light-minus-dark EPR difference spectra of the S_2-MLS, S_2-g4 and S_2-ann. samples. Four light-induced features are seen in the S_2-g4 spectrum: a broad Q_A^- signal at $g \cong 1.9$, a small MLS centered about $g=2$, a small peak at $g \cong 3.1$ representing the g_z feature of oxidized cytochrome b_{559}, and a broad $g \approx 4$ signal. The optimal temperature to generate the maximum amount of the $g \approx 4$ signal was found to be at approximately 130 K (de Paula et al., 1985). Compared with the MLS amplitude of the S_2-MLS samples, the amount of MLS left in the S_2-g4 samples was approximately 20% ± 10%. After the S_2-g4 samples were annealed at 195 K in the dark for 90 s, the $g \approx 4$ signal typically disappeared, and the amount of MLS recovered to approximately 70%. The MLS could be restored to 100% after reillumination of these S_2-ann. samples at 200 K for 7 min. This indicated that up to 30% of the PSII centers were in the S_1 state after the annealing process. We believe, however, that most of these centers were not in the S_1 state in the S_2-g4 samples before the annealing process. The evidence is as follows:

(1) The amount of the Q_A^- signal generated in the S_2-g4 samples is approximately the same as that in the S_2-MLS samples (Table III-2, see Materials and Methods for the quantitation of the Q_A^- signal.). At temperatures below 200 K, electron transfer from Q_A to Q_B is blocked. Therefore the amount of Q_A^- accumulated is proportional to the amount of the advance from the S_1 to S_2 state. No alternative donors are detected by EPR spectroscopy. This indicates that the amount of the PSII reaction center in the S_2 state is approximately the same for the S_2-g4 and S_2-MLS states.

(2) The amount of Q_A^- signal decreased approximately 30% in the S_2-ann. samples after the annealing of the S_2-g4 samples (Table III-2). This is consistent with 30-40% Q_A^-

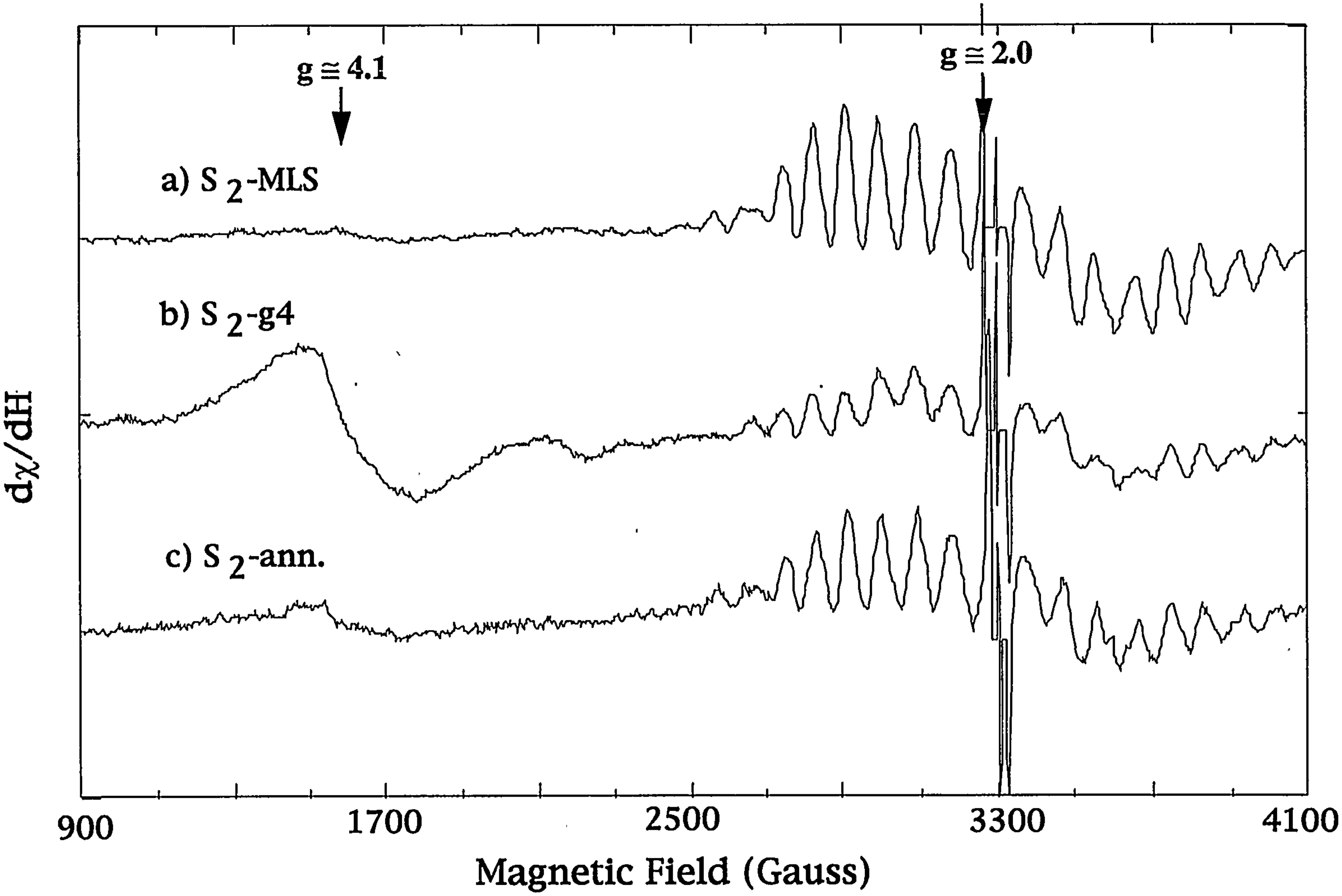

Fig. III-1: Illuminated-minus-dark difference EPR spectra of PS II samples from spinach in the (a) S_2-MLS state, (b) S_2-g4 state, and (c) S_2-ann. state. Spectrometer conditions are described under Materials and Methods.

Table III-2: Amplitudes of the multiline and Q_A^- Signals of PSII Preparations

sample	MLS amplitude[a]	Q_A^- signal amplitude[b]
S_2-MLS	100%	6.4
S_2-g4	20%	6.6
S_2-ann.	70%	4.6
200 K illumination of the S_2-ann. samples	100%	6.7

[a] Multiline signal amplitudes are expressed as percentages of those of the S_2-MLS samples. Uncertainties in the MLS amplitude quantitation are ± 10%.

[b] Q_A^- signal amplitude is expressed as described in Materials and Methods. Uncertainties in the quantitation are estimated to be ± 20%. Differences among samples are within 6%.

radical recombination with the S_2 state to form the S_1 state, resulting in only 60-70% of MLS recovery after the annealing process.

(3) Cytochrome b_{559} can function as an alternative electron donor to the PSII reaction center. Although a small oxidized cytochrome signal was detected in some of our untreated S_2-g4 samples, the same EPR and EXAFS results were obtained from S_2-g4 samples generated from S_1 state samples which did not contain any oxidizable cytochrome b_{559}. These samples were prepared by treating the PSII preparation with octacyanotungstate(V) before being dark-adapted. Octacyanotungstate(V), with its high reduction potential, has been used to oxidize cytochromes in PSII (Casey & Sauer, 1984).

The PSII centers in the S_2-g4 state have been reported to be less stable than those in the S_2-MLS state. Approximately 20% of the PSII centers in the S_2-g4 state was shown to recombine with Q_A^- generating the S_1 state at 220 K (Zimmermann & Rutherford, 1986). Our EPR results showed a decrease of approximately 30 ± 10% of the Q_A^- signal in the S_2-ann. samples. The difference of the percentage was within the uncertainty of the amplitude quantitation of the Q_A^- signal.

III.C.2. Mn K-Edge Spectra.

The Mn K-edge absorption spectra and the edge inflection energy of the representative S_1, S_2-g4, and S_2-MLS samples are compared in Fig III-2(a). All samples contain a pre-edge 1s→3d transition at approximately 6541 eV which becomes allowed in a coordination environment which is not centro-symmetric. A shift in the absorption edge to energy higher than that of the S_1 state is apparent in the S_2-g4, S_2-MLS and S_2-ann. (not shown) samples, with increases of 0.8 eV, 1.1 eV and 0.9 eV, respectively. The edge inflection energy of the S_2-g4 and S_2-ann. samples is respectively 0.3 eV and

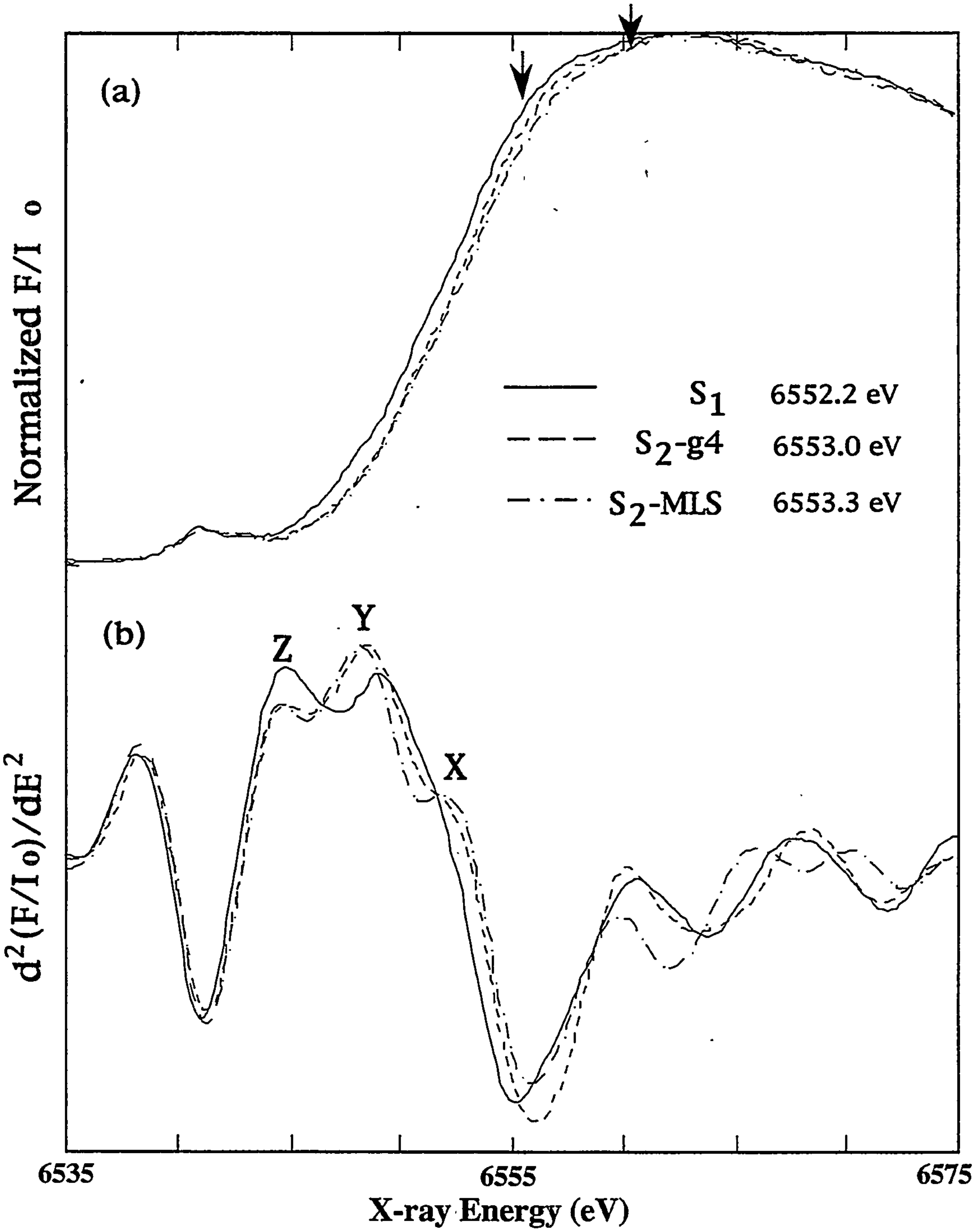

Fig. III-2: (a) Mn K-edge absorption spectra and inflection point energies of PS II particles from spinach poised in the S_1 (——), S_2-g4 (----), and S_2-MLS (-.-.-) state. (b) The corresponding second derivatives. A linear fit to the spectra below the Mn absorption edge has been removed. The inflection energies were obtained from the zero-crossing points of the second derivatives generated by analytical differentiation of a third-order polynomial fit to the data over an interval of ±3.0 eV on each side of a data point. The spectra were collected in fluorescence mode and ratioed to the incident X-ray photon intensity, I0. The inflection energy of the S_2-ann. samples (not shown) is 6553.1 eV.

0.2 eV lower than that of the S_2-MLS sample. The lower edge energy of the S_2-g4 samples is reproducible. As to the lower edge shift of the S_2-ann. from the S_2-MLS samples, it can be well explained that it is due to the 20% S_1 composition in the S_2-ann. samples. As mentioned above, this S_1 content results from the recombination reaction between the S_2 state and the Q_A^- during the annealing process.

Moreover, the edge shape of the S_2-g4 samples is clearly different from that of the S_2-MLS samples at the region close to the top of the edge (marked with arrows). Fig. III-2(b) shows the corresponding second derivatives of the K-edge spectra from Fig. III-2(a). The second derivatives reveal reproducible changes of features among the S_1, S_2-g4 and S_2-MLS samples. Feature X is minimum in the S_1 state, larger in the S_2-g4 state and increases further in the S_2-MLS state. Features Z and Y are distinctive between the S_1 and S_2 states, but quite similar within the two types of S_2 state. The small change in edge position and shape are suggestive of a change in the structure of the Mn cluster of the S_2-g4 samples relative to those of either the S_2-ann. or S_2-MLS samples. The lower edge inflection energy of the S_2-ann. sample may result from an S_1 state (≅30%) fraction generated from the recombination of the S_2-g4 centers with Q_A^- during the annealing process.

III.C.3. Mn EXAFS.

The k^3-weighted EXAFS spectra of representative S_2-MLS and S_2-g4 samples show reproducible differences in the region of k=8-10 Å^{-1} (Fig. III-3). The Fourier transforms of the k^3-weighted Mn EXAFS of the S_1 and S_2-MLS samples are shown in Fig. III-4. In Fig. III-4, the positions of the three peaks, labelled Peaks I-III, correspond to shells of scatterers at different "apparent" distances from a Mn absorber. These "apparent" distances are shorter than the actual distances due to an average phase shift

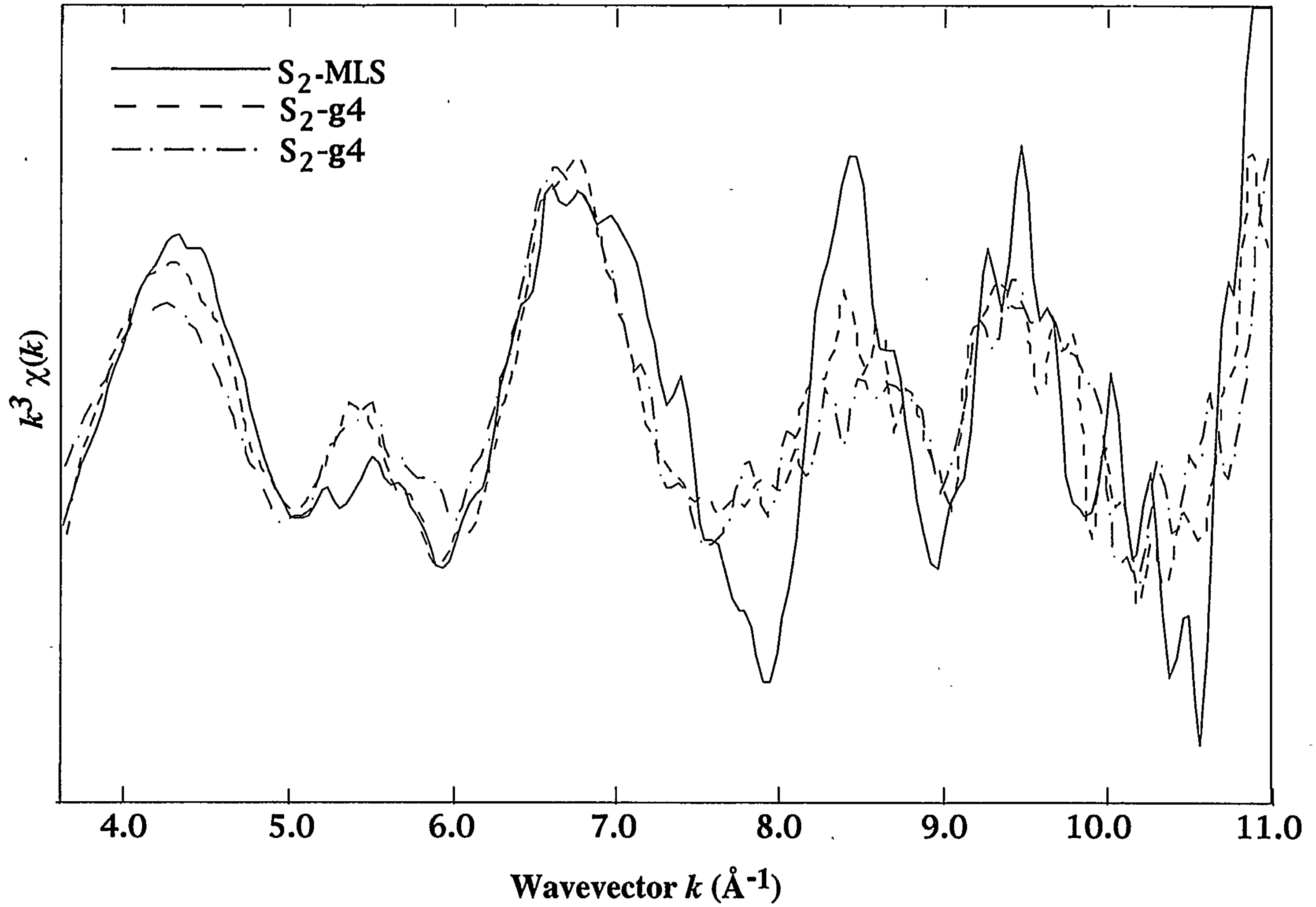

Fig. III-3: k^3-weighted EXAFS spectra of two kinds of S_2 samples: S_2-MLS (solid line), and two S_2-g4 samples (two dashed traces).

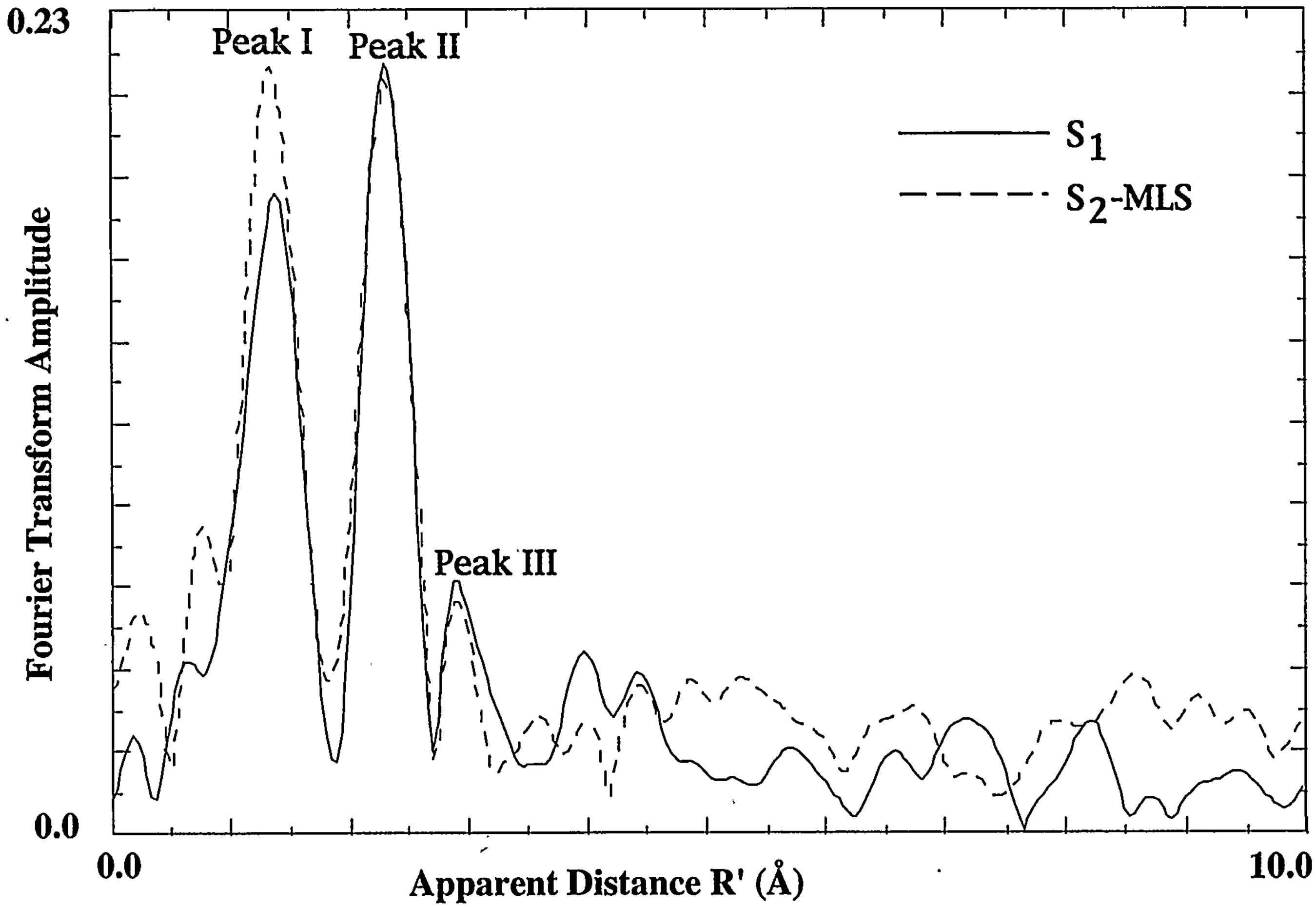

Fig. III-4: Fourier transform spectra of the k^3-weighted Mn EXAFS of the S_1 (——) and S_2-MLS state (----). The distances indicated are shorter than the actual distances to the scattering shells because of an average phase shift which is characteristic of the given absorber-scatterer pair.

induced by the potential effect of the given absorber-scatterer pair on the photoelectron (Sayers et al., 1971). Peak II and Peak III are quite similar between the S_1 and S_2-MLS state (Fig. III-4). Peak I in Fig. III-4 is assigned to 2 ± 0.2 N or O ligand atoms at distances of ~1.8 Å and 2 to 4 N or O ligand atoms at distances between 1.95 Å to 2.15 Å. Peak II is mainly due to the backscattering from 1.2 ± 0.2 Mn neighbors at 2.7 Å from the Mn absorber. Peak III could arise from Mn or Ca at about 3.3 Å (Sauer et al., 1992; Yachandra et al., 1993).

The Fourier transform spectra (Fig. III-5) of the S_2-g4 sample *k*-space data (Fig. III-3) show that Peaks II and III are decreased in amplitude relative to the S_2-MLS samples. The amplitude decrease of Peak III is less prominent than that of Peak II. The heights of these major Fourier transform peaks for the S_2-g4, S_2-MLS, S_1, and S_2-ann. samples are listed in Table III-3. The heights of Peaks II and III of the S_2-g4 samples are respectively 60 ± 10% and 75 ± 10% of the corresponding peaks of the S_2-MLS and S_1 samples. After annealing the S_2-g4 samples to 200 K in the dark for 90 s the amplitudes of Peaks II and III recovered to 90-95% and 100%, respectively.

To determine whether the decrease of the Fourier transform peak heights was a result of sample damage caused by X-ray exposure, an S_2-g4 sample was annealed to 200 K after the XAS experiment. The intensity of the MLS recovery for this test sample was the same as that obtained from the annealed samples before the XAS experiment. Further evidence against the occurrence of X-ray damage was provided by the Mn K-edge spectra of the S_2-g4 samples. It has been reported that damage to the Mn cluster of the OEC results in a release of Mn^{2+}, which shows a sharp characteristic feature in the Mn K-edge spectra of the PSII samples (Cole et al., 1987, Yachandra et al., 1993). Our samples did not show such a Mn^{2+} feature.

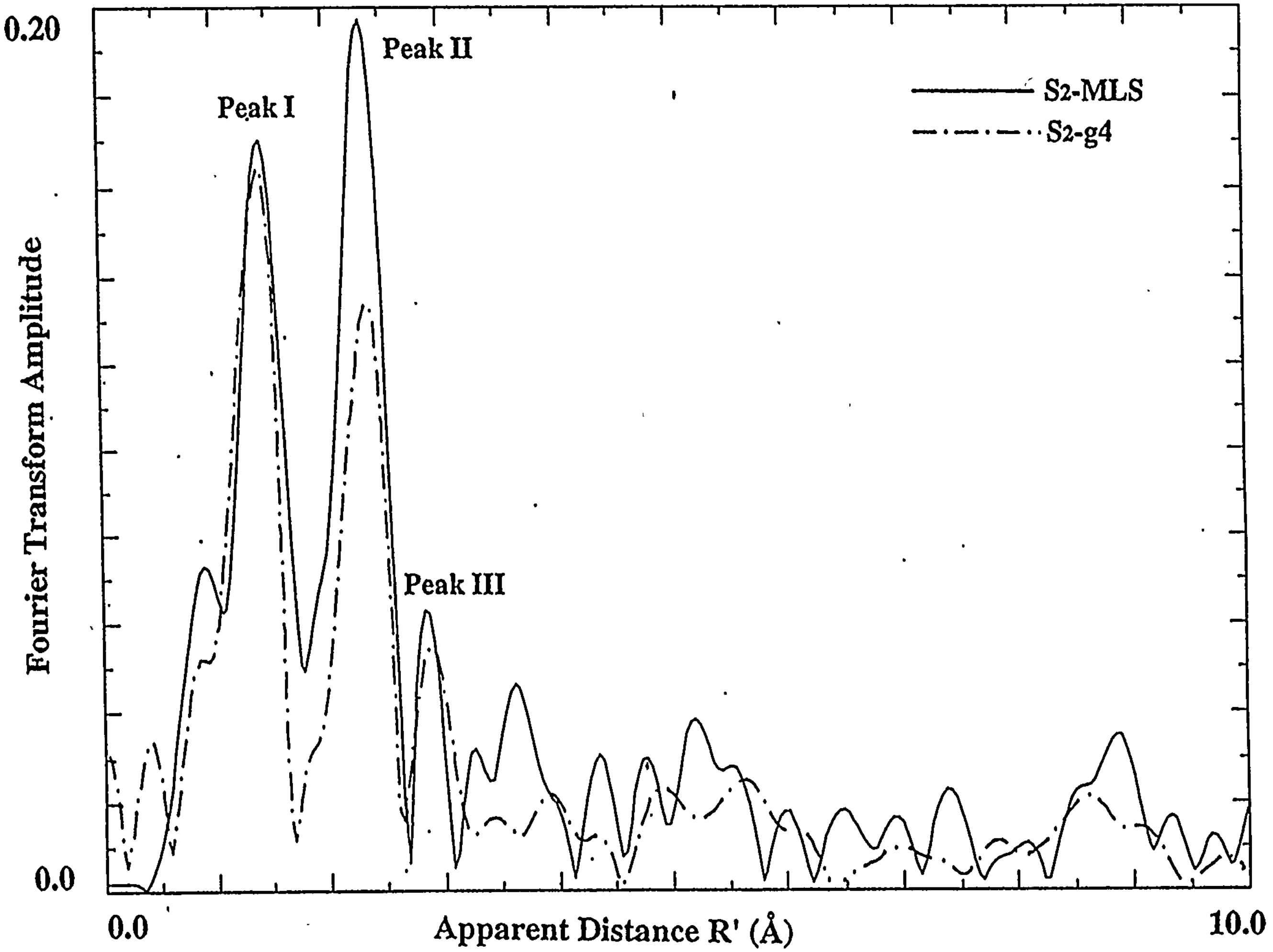

Fig. III-5: Fourier transform spectra of the k^3-weighted Mn EXAFS of the S_2-g4 sample (-·-·-) and S_2-MLS sample (——). The significantly smaller Peak II in the EXAFS of the S_2-g4 sample indicates a more disordered system. The height decrease of Peak III is less prominent than that of Peak II.

Table III-3: Relative Peak Heights of the Fourier Transform of the EXAFS Data from the S_2-g4, S_2-MLS, S_2-ann. and S_1 samples. Peak Heights Are Normalized to Edge Jump.

sample	Peak I	Peak II	Peak III
S_1	0.18	0.21	0.07
S_2-g4[a]	0.18	0.12	0.05
S_2-MLS[b]	0.20	0.20	0.07
S_2-ann.[b]	0.19	0.19	0.08

[a] Average results obtained from 4 samples, the uncertainty within these samples is estimated to be ± 0.05 in Peak I, ± 0.02 in Peak II and ± 0.01 in Peak III, of the average value in this table.

[b] Average value from two samples with an uncertainty of ± 0.02 in Peak I and ± 0.01 in Peak II or Peak III.

III.C.3.1. Curve Fitting of Peak II.

Peak II in the Fourier transform spectra of the S_2-g4 samples is substantially smaller than that of the S_2-MLS samples. This decreased amplitude is characteristic of an increased distance disorder. To further assess the relation between the amplitude decreases in the Fourier transform peaks and the possible structural changes in the Mn clusters in the OEC, each isolated R-space peak was back-transformed to *k*-space. Simulations using the curved-wave approximations were then performed on these isolated *k*-space data (McKale et al., 1988) .

The Fourier-isolated *k*-space spectra, reflecting back-scattering from the second coordination shell of the Mn cluster in the S_2-g4 and S_2-MLS samples, together with their simulated *k*-space spectra are shown in Fig. III-6. Based on the EXAFS analysis on the S_1 and S_2-MLS samples (McDermott et al., 1988; DeRose, 1990), it is estimated that there is 1.2 ± 0.2 Mn-Mn vector at 2.7 Å from each Mn absorber. However, single-shell fits to Peak II from the S_2-g4 samples with Mn coordination number constrained to 1.2 result in the least-squares residuals 2 to 10 fold larger than those from the two sub-shell fits (Table III-4). In addition, the Debye-Waller factors for these single-shell fits are 2- to 4-fold larger than the values (about 0.005 Å^2) reported previously (Yachandra et al., 1993). (Table III-4). Fits to the second shell EXAFS of the S_2-g4 samples with unconstrained Mn coordination number also produced unsatisfactory fitting results including (1) at least a four-fold increase of the least-squares residuals, (2) a doubling of the value of the Mn-Mn Debye-Waller factors, and (3) only 0.65 of Mn-Mn vector in this shell (Data not shown). The results described above indicate that Peak II of the S_2-g4 state corresponds to more than one sub-shell.

Fig. III-6: *k*-space spectra of isolated Peak II (——) for the S_2-g4 and S_2-MLS samples. These EXAFS oscillations were obtained by first applying a window function to Peak II, and then back-transforming it to *k*-space. The fit to a Fourier-isolated Peak II is indicated by the dotted traces. The spectra shown are of (a) the S_2-g4 sample simulated with two Mn sub-shells, (b) the S_2-g4 sample simulated with one Mn shell, (c) the S_2-MLS sample simulated with two Mn sub-shells, and (d) the S_2-MLS sample simulated with one Mn shell. Simulation parameters for the fits are listed in Table III-5. Inclusion of a second sub-shell is shown to be important to improve the quality of fits for the S_2-g4 samples. Much less improvement is obtained to the fits of the S_2-MLS samples.

(a) S_2 (g=4)

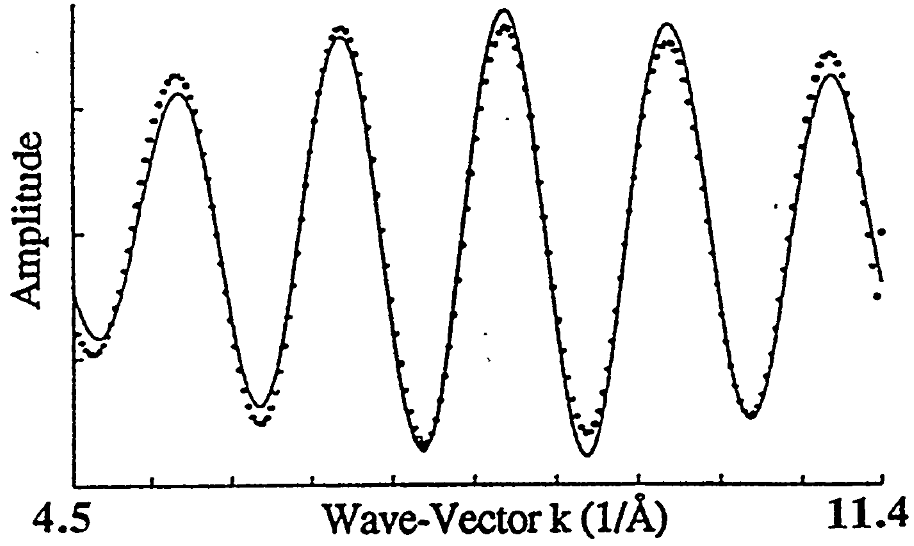

N	R(Å)	σ^2(Å^2)	ΔE_0	F
0.76	2.72	0.001	-13.0	2
0.44	2.85	0.003	-19.2	

(b) S_2 (g=4)

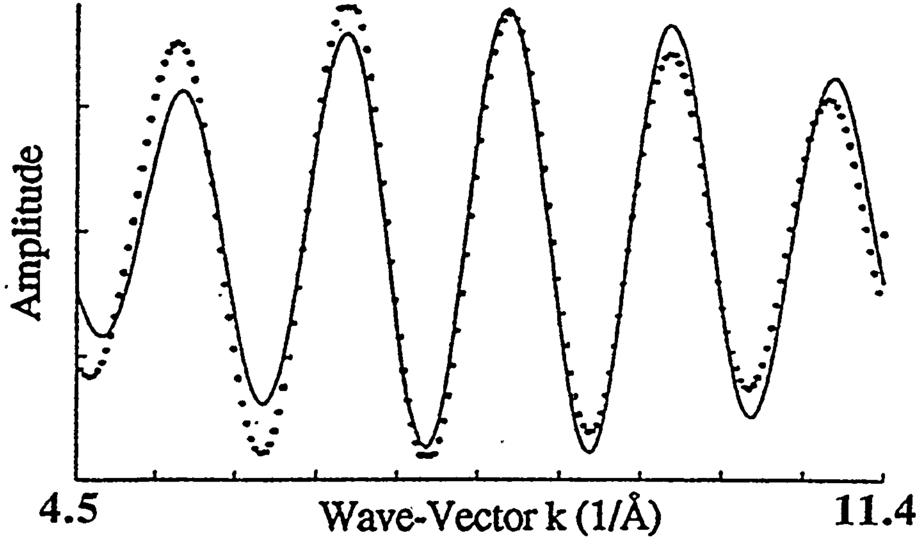

N	R(Å)	σ^2(Å^2)	ΔE_0	F
1.2	2.73	0.010	-17.0	8

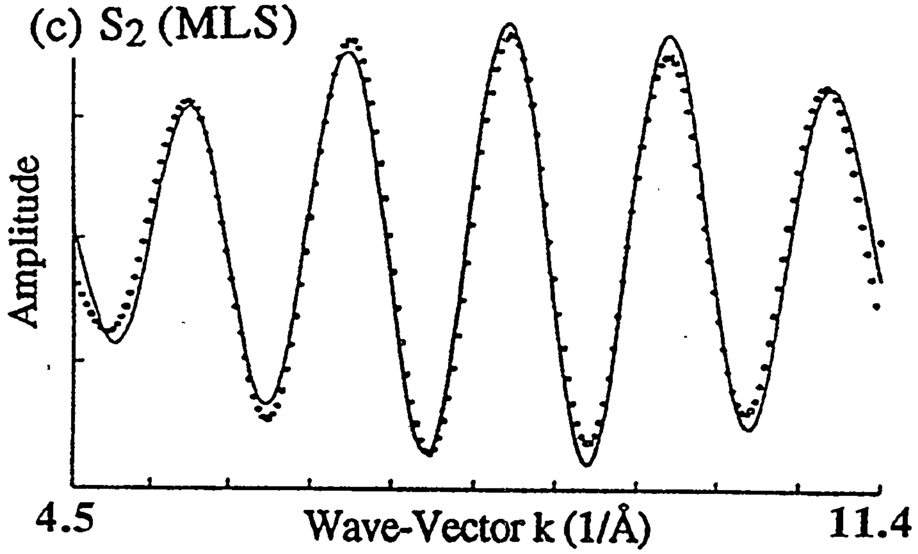

N	R(Å)	σ^2(Å^2)	ΔE_0	F
0.6	2.71	0.002	-19.9	9
0.6	2.81	0.012	0.35	

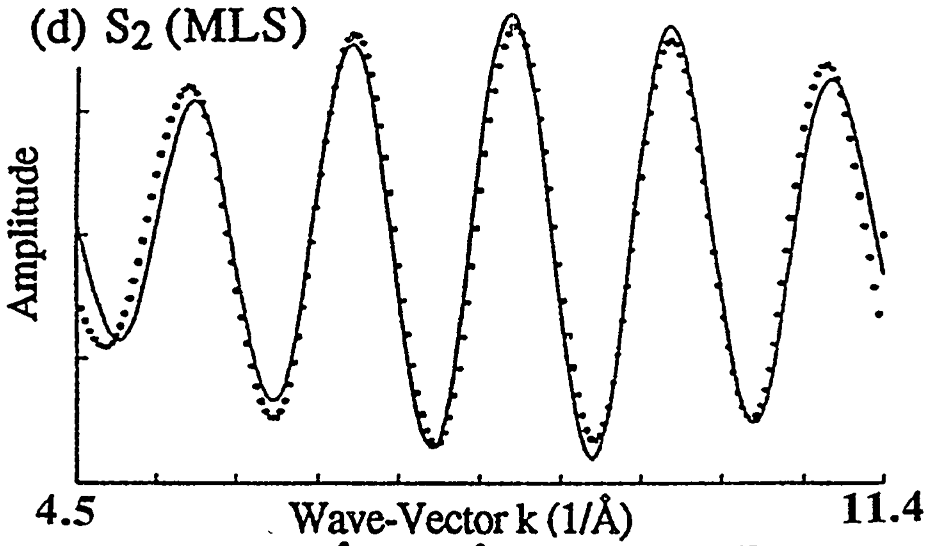

N	R(Å)	σ^2(Å^2)	ΔE_0	F
1.2	2.73	0.005	-14.1	13

Table III-4: One-shell Simulation Results for the Second Shell of the k^3-Weighted EXAFS Data of the S_2-g4 Samples.

sample[c]	N[a]	R(Å)	$2\sigma^2$(Å^2)	ΔE_0	F[b]	
1	1.2	2.74	0.011	-16.0	20*	
2	1.2	2.72	0.011	-17.6	11*	
3	1.2	2.80	0.020	-11.5	9*	
4	1.2	2.73	0.010	-16.0	7	

[a] The coordination number N was constrained to 1.2.

[b] F is the least-squares residual difference between the Fourier-isolated EXAFS and the EXAFS calculated by using theoretical phase and amplitude functions using curved-wave approximations.

[c] Four individual S_2-g4 samples.

*The differences between the fits and the experimental traces are large.

Our previous EXAFS study on F$^-$-treated S_2 state also required two sub-shells at ~2.7 Å from the Mn absorber (DeRose, 1990). Therefore, a series of simulations and fits were made for a model with two sub-shells on the S_2-g4 samples (Table III-5). The numbers of scatterers of the two sub-shells were allowed to vary but with their sum fixed to a value of 1.2, which was obtained from our previous study of the S_1 and S_2-MLS state (McDermott et al., 1988; DeRose, 1990). The resulting least-squares residuals decrease to one quarter of those from the one-shell fits. In addition, the two-shell fits also provide more reasonable values of Debye-Waller factor for each sub-shell and much better fit quality. (See Fig. III-6a and III-6b.)

In contrast, when two-subshell fits to the EXAFS data from the S_1, S_2-MLS, and S_2-ann. samples are performed, 2- to 10-fold larger Debye-Waller factors are found in at least one of the two sub-shells, which is contrary to what is expected (Table III-5). When the fitting included two Mn sub-shells with unconstrained coordination numbers, the 2.74 Å sub-shell accounts for nearly 90% of the total second-shell scatterers (Data not shown). For some samples, good two-shell fits are observed with two close sub-shells (2.72 Å and 2.77 Å). All of these facts indicate that a two-sub-shell model is not necessary for the S_1, S_2-MLS, and S_2-ann. samples.

III.C.3.2. Curve Fitting of Peak III.

Curve fitting of Peak III was performed on isolated, back-transformed *k*-space spectra, as was done for Peak II. The isolated *k*-space oscillations of the S_2-g4 samples have a lower overall amplitude and are damped at higher *k* values in comparison with the S_2-MLS samples (Fig. III-7). This indicates a greater distance disorder in this shell of the S_2-g4 samples and is consistent with the smaller amplitude of Peak III in the Fourier transform spectra. Simulation results are summarized as follows:

Table III-5: Simulation Results for the Second Shell of the S_2-g4, S_2-MLS, S_1 and S_2-ann. Samples.

(A) One-Shell Fits for k^3-Weighted Data

			N[b]	R(Å)	$2\sigma^2$(Å^2)	ΔE_0	F
		S_2-g4[a]	1.2	2.73	0.010	-17.0	8
		S_2-MLS	1.2	2.73	0.005	-14.1	13
		S_2-ann.	1.0	2.72	0.004	-18.0	10
		S_1	1.2	2.74	0.006	-13.7	6

(B) Two-Shell Fits for k^3-Weighted Data

	N_1[b]	R_1(Å)	$2\sigma^2$(Å^2)	ΔE_0	N_2	R_2(Å)	$2\sigma^2$(Å^2)	ΔE_0	F
S_2-g4[a]	0.76	2.72	0.001	-13.0	0.44	2.85	0.003	-19.2	2
S_2-MLS	0.6	2.71	0.002	-19.9	0.60	2.81	0.012	0.35	9
S_2-ann.	0.6	2.71	0.010	-19.0	0.60	2.90	0.040	7.00	9
S_1	0.6	2.72	0.003	-18.7	0.60	2.87	0.020	4.11	3

[a] Average results obtained from the four S_2-g4 samples in Table III-4. In general, distances obtained for individual samples differed by less than 0.02 Å.

[b] The number of scatterers determined at a given distance in different samples of each type was found to be within 8%.

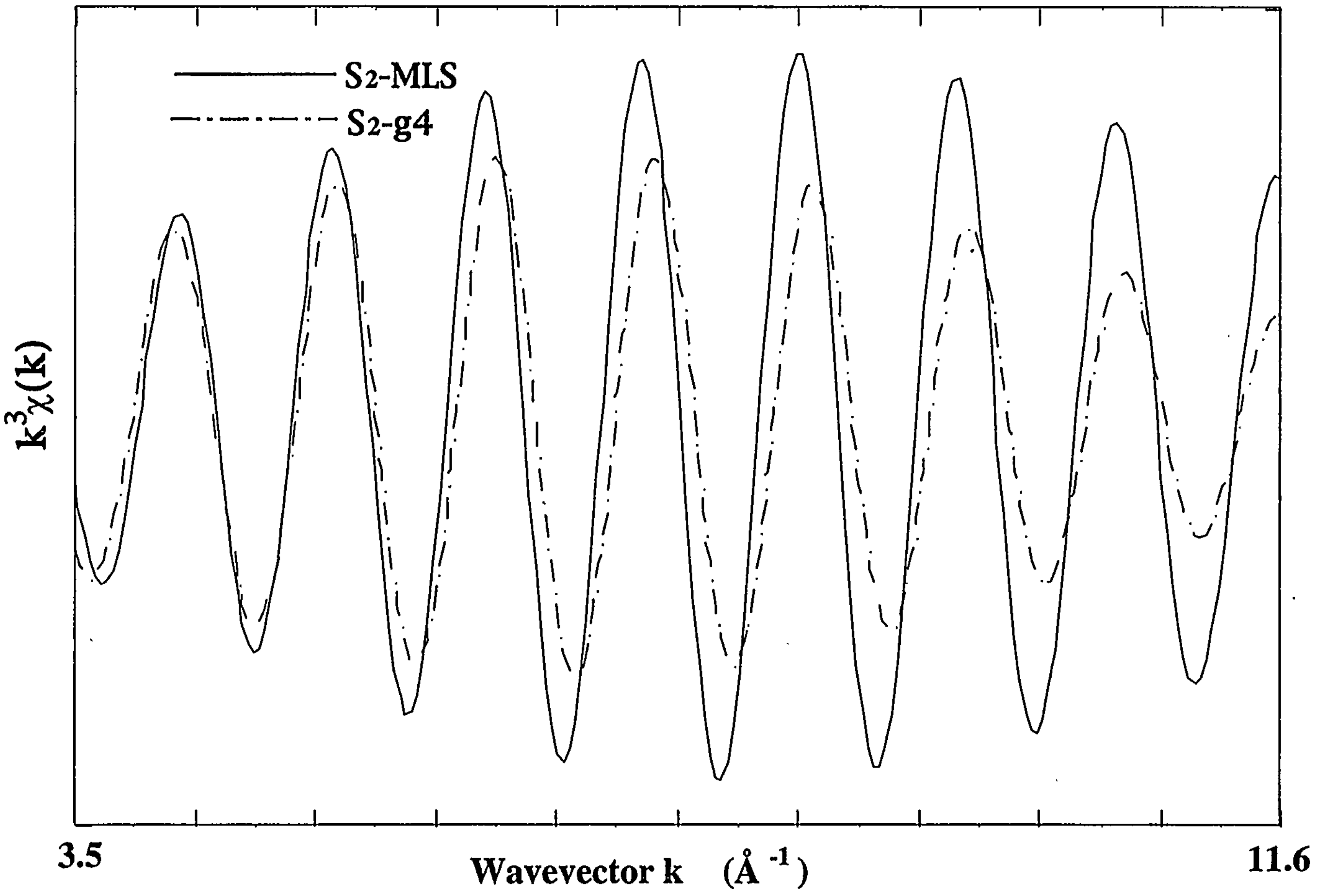

Fig. III-7: Fourier isolates to the third shell of the k^3-weighted Mn EXAFS of the S_2-g4 sample (-.-.-) and S_2-MLS sample (——).

1) The S_2-g4 samples:

Peak III can be fit to a single Mn shell (denoted the 1-Mn fits) at 3.35 Å with unconstrained Debye-Waller factor (0.014 Å^2). The 1-Mn fits to the S_2-g4 samples also requires a coordination number larger than that for the S_2-MLS, S_2-ann. or the S_1 samples (Table III-6A). This larger coordination number is suggestive of a larger Mn scatterer contribution and indicates the possibility of an additional Mn-Mn vector at ~3 Å.

Satisfactory fitting results are also found in three types of two sub-shell fits (Table III-6B): (a) the 2-Mn$_a$ fits, with 1.2 ± 0.1 Mn-Mn vector, (b) the 2-Mn$_b$ fits, with 0.6 ± 0.05 Mn-Mn vector and (c) the Mn+Ca fits, with 0.5-0.6 Mn-Mn vector and 0.26-0.3 Mn-Ca vector per Mn atom in the cluster. All of the two sub-shell fits reduce the least-squares residuals up to 3-fold, and the Debye-Waller factors of each sub-shell approximately 3 to 10 fold. The first sub-shell in these three types of fits is at approximately 3.33 Å from the Mn absorber. The second sub-shell is about 0.11 Å (the 2-Mn$_a$ and 2-Mn$_b$ fits) or 0.20 Å (the Mn+Ca fits) more distant than the first sub-shell.

For the 2-Mn$_a$ fits, the coordination number is equally distributed between the two sub-shells and is approximately twice the value reported in previous studies (DeRose, 1990; Yachandra et al., 1993). For the 2-Mn$_b$ fits, the distribution of the 0.6 Mn-Mn vectors is uneven, with the ratio of the coordination numbers between the 2 sub-shells ranging from 1.5:1 to 2:1. The backscatterer of the second sub-shell is replaced by a calcium in the Mn+Ca fits. The Mn+Ca fits are obtained by constraining the coordination number of each sub-shell to a physically meaningful value (Table III-6B). The distance of the Ca sub-shell in the Mn+Ca fits is approximately 0.1 Å longer than that of the second sub-shell in the 2-Mn$_a$ and 2-Mn$_b$ fits. Because the fit quality among

Table III-6: Simulation Results for the Third Coordination Shell of the S_2-g4, S_2-MLS, S_1 and S_2-ann. Samples; k^3-Weighted EXAFS Data[a].

(A) One-Shell Fits for k^3-Weighted Data (1-Mn Fits)

			N	R(Å)	$2\sigma^2$(Å^2)	ΔE_0	F[b]
	S_2-g4		0.72	3.35	0.014	-11.4	0.41
	S_2-MLS		0.40	3.31	0.007	-13.5	0.47
	S_2-ann.		0.48	3.30	0.005	-20.0	1.08
	S_1		0.48	3.31	0.005	-13.1	0.77

(B) Two-Shell Fits for k^3-Weighted Data from S_2-g4 samples

		N	R(Å)	$2\sigma^2$(Å^2)	ΔE_0	F[b]
2-Mn_a Fits	Mn1 Mn2	0.60 0.56	3.33 3.45	0.0025 0.0043	-4.4 -11.2	0.13
2-Mn_b Fits	Mn1 Mn2	0.40 0.20	3.33 3.47	0.0034 0.0044	-7.2 -1.7	0.15
Mn+Ca Fits	Mn Ca	0.50 0.26	3.35 3.55	0.0045 0.0012	-4.3 -4.0	0.13

[a] In general, distances obtained for individual samples differed by less than 0.02 Å. The number of scatterers determined at a given distance was found to be within 20%.

[b] F is the least-squares difference between the Fourier-isolated EXAFS and the EXAFS calculated by using theoretically derived phase and amplitude functions with the curved-wave formalism (McKale et al., 1988).

the 2-Mn_a, 2-Mn_b, and Mn+Ca fits is similar, we cannot exclude any of the two sub-shell fits for Peak III based on the present data.

2) The S_2-MLS, S_2-ann. and S_1 samples:

Satisfactory results are obtained from the 1-Mn fits in these samples (Table III-6A). The fits to two Mn sub-shells result in large Debye-Waller factors from each sub-shell and therefore are unnecessary (data not shown). However, a Mn+Ca fit results in a decrease of the Debye-Waller factors from both sub-shells and the least-squares residuals relative to those of the 1-Mn fits. Therefore, we cannot exclude the possibility of the Mn+Ca fits to the third shell. The coordination numbers and distances from the best fits for these samples are similar to those from the Mn+Ca fits of the S_2-g4 samples (Table III-6B).

III.D. Discussion.

III.D.1. Edges.

Our Mn K-edges from the S_2-g4 samples show an edge shift of 0.8 eV to higher energy after illuminating the S_1 samples at 131 K. This result, which is indicative that Mn is oxidized during the S_1 to S_2-g4 transition, is in agreement with the previous edge study for samples measured at 170 K (Cole et al., 1987). Our present data, with improved signal-to-noise, show a subtle difference of the edge shape and inflection energy from the previous report. Analyses of the second derivatives of the K-edge spectra further reveal reproducible changes in features and edge position (0.3 eV) between the S_2-g4 and S_2-MLS samples. A structural variation within the Mn cluster could be responsible for both of the changes in edge shape and position. This possibility is supported by the EXAFS data (See below).

III.D.2. EXAFS Studies on Peak II of the S_2-g4 state.

In the present study, the best simulations of Peak II are obtained by introducing two Mn-Mn sub-shells. One sub-shell is at 2.72 Å which is close to that found for the S_2-MLS and S_1 states. The other sub-shell is at 2.85 Å. Upon annealing, the distance of this sub-shell changes back to ~2.72 Å again. The Mn-Mn distance in μ-oxo bridged compounds depends on both the bridging Mn-oxo distance and the Mn-oxo-Mn bond angle. It has been shown that in a synthetic model compound the oxidation of Mn(III,IV) to Mn(IV,IV) causes an increase in the Mn-Mn distance by 0.05 Å (Wieghardt, 1989). The distance increase could be even larger in a protein environment where ligands are derived from amino acid side chains (DeRose, 1990).

Other than the S_2-g4 samples, a previous report on the S_3 state also showed inhomogeneity in its Peak II (Guiles et al., 1990b). In addition, the Fourier transform of the EXAFS data obtained from annealed ammonia-treated S_2 states also show a smaller Peak II (Dau et al., submitted.). However, there are differences between the S_2-g4 and both the ammonia-treated and S_3 samples. In the case of the ammonia-treated and S_3 samples, the second peak could be fit by increasing the Debye-Waller factor. In the case of the S_2-g4 data, it is clear that two different distances are required; just increasing the Debye-Waller parameter does not lead to a satisfactory fit. This fact implies that the second shell disorder of the S_2-g4 state is probably larger than that of the S_3 state or the ammonia-treated S_2 state.

The best two-shell fits obtained for Peak II of the S_2-g4 samples give inequivalent values for the coordination number of Mn scatterers for each sub-shell. Approximately

60% of the total scatterers is contributed by the 2.72 Å sub-shell and 40% by the 2.85 Å sub-shell. (See Table III-5.) We propose that 40% of the 2.72 Å vector arises from the S_2-g4 state, which contains equal amounts of the 2.72 and 2.85 Å vectors. The additional 20% of the 2.72 Å vector is contributed by a fraction of the sample responsible for the small S_2-MLS residuals in the S_2-g4 sample. This argument is supported by our EPR measurements. Table III-7 shows that the coordination numbers of the two sub-shells estimated from the S_2-g4 samples are close to those obtained from the best fits of our EXAFS data.

III.D.3. EXAFS Studies on Peak III of the S_2-g4 state.

Fitting Peak III of the Fourier transforms from the PSII samples is more challenging due to its small amplitude. The backscattering contribution is weaker and more complicated at this longer distance. Relative to the S_2-MLS, S_2-ann. or S_1 samples, the S_2-g4 samples contain an increased distance disorder in Peak III, which results in a larger Debye-Waller factor required for the 1-Mn fits. Three possible 2 sub-shell fits were also investigated: (a) the 2-Mn_a fits, (b) the 2-Mn_b fits, and (c) the Mn+Ca fits. Among these simulation results, the 1-Mn and the Mn+Ca fits are compatible with the model of the Mn complex previously proposed by our group (Yachandra et al., 1993). However, to satisfy the 2-Mn_a fits would require an additional Mn-Mn vector at ~3.45 Å in the S_2-g4 state and this would imply a large structural rearrangement in the Mn cluster. This would involve a slight tilt of dimer I towards dimer II that results in a formation of a new Mn-Mn vector at 3.45 Å. Further, the possible interpretation of the 2-Mn_b fits requires hetereogeneity in the PSII centers where 2/3 of the centers contains 0.6 Mn-Mn vector at 3.33 Å and the other 1/3 of them at 3.47 Å.

Table III-7: The Effective Sub-shell Coordination Numbers (N_1, N_2) Based on the EPR Measurements and on the EXAFS Data from Four Individual S_2-g4 Samples. $N_1+N_2=1.2$.

% of residual MLS from EPR		(N_1 , N_2) estimated using % of residual MLS from EPR	(N_1 , N_2) from the best EXAFS fits
sample 1	23%	(0.74 , 0.46)	(0.76 , 0.44)
sample 2	22%	(0.73 , 0.47)	(0.76 , 0.44)
sample 3	19%	(0.71 , 0.49)	(0.68 , 0.52)
sample 4	21%	(0.72 , 0.48)	(0.72 , 0.48)

On the other hand, the best fits to Peak III of the S_2-MLS, S_2-ann. or the S_1 samples for the 1-Mn or Mn+Ca fits require only one distance and 0.5 Mn-Mn vector per Mn atom in the cluster. The 1-Mn and Mn+Ca fits are indistinguishable, and this is consistent with the previous results with the S_2-MLS or S_1 PSII samples prepared either from spinach or cyanobacteria (DeRose, 1990).

It has been reported that the EXAFS curve-fitting techniques are problematic in dilute biological samples when one attempts to identify scattering atoms at distances > 3 Å, and hence it is difficult to arrive at a unique structural solution from such fits (Scott & Eidsness, 1988). Our results for Peak III also do not provide a unique solution for the S_1, S_2-g4, S_2-ann. or S_2-MLS samples. The ambiguity of differentiating among various fits to Peak III indicates that other approaches are required to reveal its composition. For example,it has been shown that, for the Ca^{2+}-depleted PSII particles, the oxygen evolving activity can be revived by adding Sr^{2+}, which is believed to replace the Ca^{2+} (Boussac & Rutherford, 1988). Therefore, fits of Peak III from the Fourier transform spectra of the Sr^{2+}-substituted PSII particles provide more direct evidence of a probable calcium scatterer. Previous studies in our group on the Sr^{2+}-reconstituted PSII strongly support the existence of Ca scatterers in Peak III (Yachandra et al., 1993; Latimer et al., manuscript in preparation).

III.D.4. Models.

In previous reports, a model has been proposed for the Mn cluster based on the EXAFS results of the S_1 and S_2-MLS state (DeRose, 1990; Yachandra et al., 1993). The overall structure of the Mn complex in the S_1 state is similar to that of the S_2-MLS state. As shown in Fig. III-8b, the Mn cluster in either of these states is proposed to consist of a pair of di-μ-oxo bridged Mn dimers (labeled as dimer I and dimer II) with a 2.7 Å Mn-Mn

Fig. III-8: A structural model: (a) for the S_2-g4 state. (b) for the S_2-MLS state. The Mn(IV,IV) and Mn(III,IV) are denoted by dimer I and dimer II, respectively. The S_2-g4 state is suggested to arise from the middle Kramers doublet of an S=5/2 spin state, which is generated by the ferromagnetic coupling between the dimer I ground state with S_I=1/2 and the dimer II second excited state with S_{II}=2. In this model, a critical ligand site is occupied by a OH^-/H_2O ligand, which modulates the exchange coupling in the Mn complex. In the structure of the S_2-MLS state, chloride is allowed to occupy the critical site resulting from ligand rearrangement at 200 K. This rearrangement results in the S=1/2 ground state due to the antiferromagnetic coupling between S_I=1/2 and S_{II}=0.

(a): S_2-g4 State

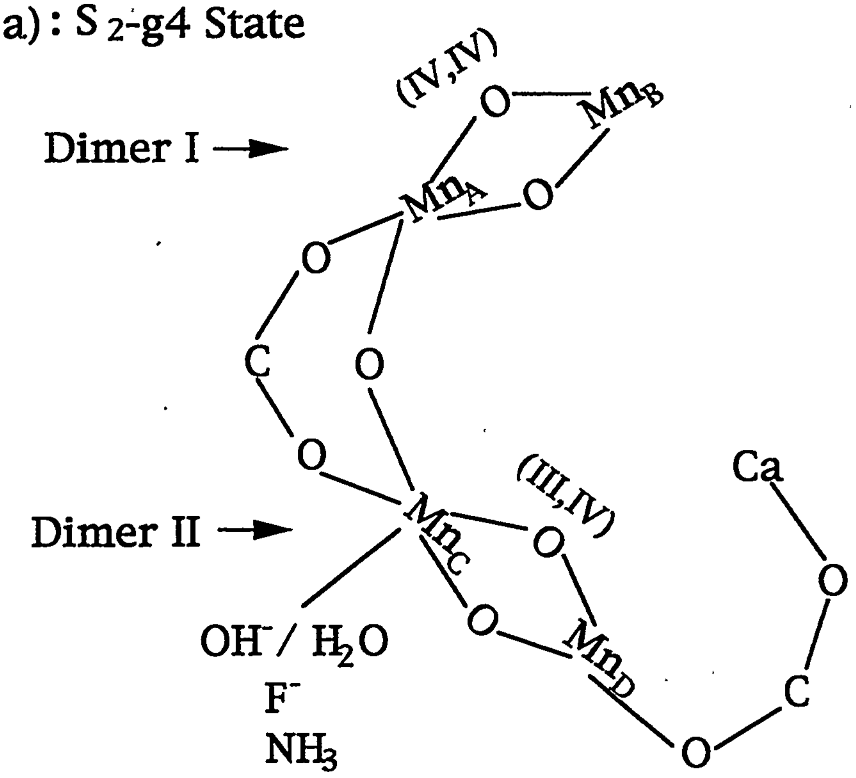

(b): S_2-MLS State

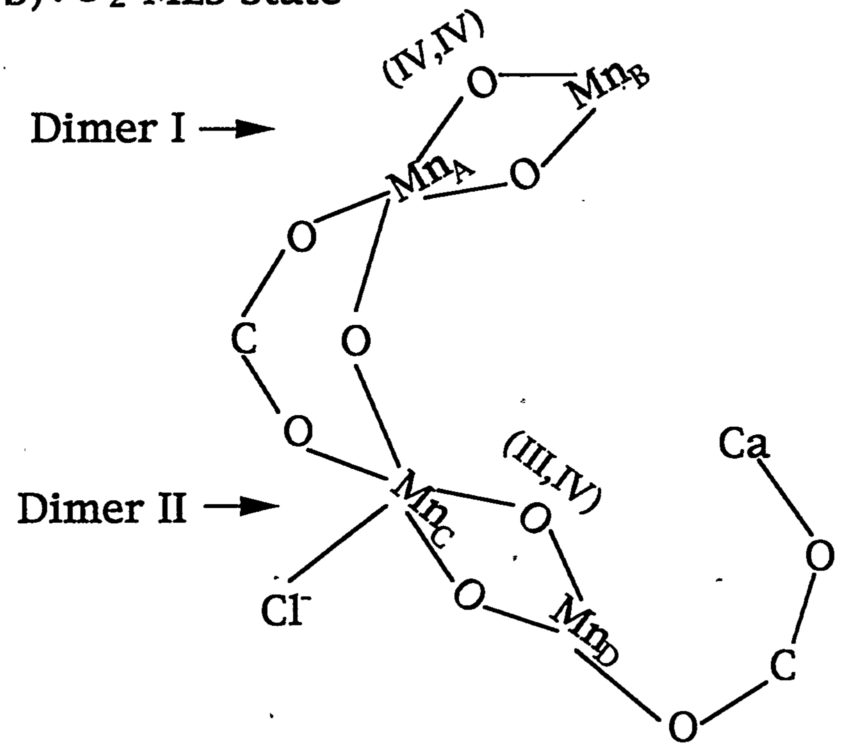

separation in each dimer. Mn_A in dimer I and Mn_C in dimer II, separated by ~3.3 Å, are linked by a mono-μ-oxo and a mono-μ-carboxylato or di-μ-carboxylato bridges. The distances between Mn_A-Mn_D, Mn_B-Mn_D and Mn_B-Mn_C pairs are longer and not detected in our EXAFS data. Note that this model is only one of the topologically equivalent possibilities which are compatible with our data. Detailed model candidates have been discussed elsewhere (DeRose et al., 1994). In the S_2-MLS state, dimer I and dimer II are proposed to be Mn(IV,IV) and Mn(III,IV), respectively, based on previous results from the Mn K-edge spectra. Two speculative sites for Cl^- and Ca^{2+} ions are also shown in this model.

A similar model is proposed for the S_2-g4 state with the following modifications based on the present study:

1) the Mn_C-Mn_D separation in dimer II increases from 2.73 Å to 2.85 Å,

2) an OH^-/H_2O ligand occupies the site where Cl^- is bound in the S_2-MLS state.

We propose that the g=4 signal arises from ferromagnetic coupling between the dimer II $S_{II}=1/2$ ground state and the $S_I=2$ state of dimer I. On the other hand, the MLS arises from antiferromagnetic coupling between the dimer II ground state and the dimer I ground state with $S_I=0$. To account for the appearance of the g=4 EPR signal at 130 K, we propose that one critical ligand site is occupied by an OH^-/H_2O ligand which is replaced by Cl^- in the S_2-MLS state. This proposal is consistent with the results that the g=4 signal in Cl^--depleted S_2-g4 samples is replaced by the MLS upon adding Cl^- in the dark at 0 °C (Ono et al., 1986). This OH^-/H_2O ligand modifies the molecular arrangement of the Mn cluster in a way that results in an increase in one of the Mn-Mn distances to 2.85 Å and increased heterogeneity in the 3.3 Å vector. This could modulate the magnetic coupling and result in ferromagnetic exchange coupling between these two dimers. Fluoride and ammonia, which enhance the g=4 signal in the S_2 state, are also proposed to occupy the same site as OH^-/H_2O ligand. Based on the results that NH_3 and F^- compete for a Cl^- site on Mn (Yocum, 1992), it has been suggested that the conversion of the S_2-g4 to S_2-MLS state involves the binding of Cl^- even at a temperature as low as 160 K (Beck & Brudvig, 1988; Rutherford et al., 1991; Rutherford et al., 1992). Upon warming to 200 K, chloride can then, by small structural rearrangement in the Mn complex, replace the OH^-/H_2O at this site to generate the MLS. At the same time, the Mn-Mn distance of dimer II changes from 2.85 Å to 2.73 Å.

The single μ-oxo bridge between the two dimers plays a key role in the conversion from the S_2-g4 to S_2-MLS state. Studies of inorganic compounds have shown that the exchange-coupling through a single μ-oxo bridge between two Mn atoms can vary from weakly ferromagnetic ($J>0$) to antiferromagnetic ($J<0$) depending on the terminal ligands (Wieghardt, 1989). Unlike the di-μ-oxo-bridged Mn dimers, which usually have strong antiferromagnetic exchange coupling ($J \ll 0$), the flexibility of this single μ-oxo bridge makes the Mn complex more sensitive to the changes of its environment. It has been reported that a small change, such as protonation of the bridging oxygen, is enough to switch between these two types of exchange coupling (Hagen et al., 1989). For the S_2-g4 state, the low formation temperature (130 K) may inhibit rearrangement of the ligands around the Mn atoms. Such rearrangement would be required for the MLS formation and may happen only at higher temperatures (~200 K).

III.E. Conclusions.

The structure of the S_2-g4 state is unique, it is similar to neither the S_1 nor the S_2-MLS state. The evidence comes from our results of X-ray absorption spectroscopy:

1) EXAFS analyses indicate that a structural rearrangement occurs during the S_1 to S_2-g4 transition at 130 K that causes the Mn-Mn distance in one of the di-μ-oxo bridged Mn dimers to increase from 2.73 Å to 2.85 Å. An S_2-MLS state generated by either direct illumination of the S_1 state or by annealing the S_2-g4 state at 200 K has only one distance (2.72 ± 0.01 Å) in the second shell of scatterers. This change is proposed to arise from a rearrangement of the Mn cluster due to a Cl^- ligand binding which is not allowed at 130 K.

2) EXAFS analyses also indicate a larger distance disorder of the third shell for the S_2-g4 state. Two sub-shells, reflecting either the 2-Mn or the Mn+Ca fits, as well as the 1-Mn fits with a large Debye-Waller factor generate satisfactory simulations to the third shell. On the other hand, 1-Mn or Mn+Ca fits are better for the S_1, S_2-MLS, or S_2-ann. state.

3) Both the S_2-g4 and S_2-MLS states show a positive K-edge shift from the S_1 state. The energy of the Mn K-edge for the S_2-g4 state is 0.3 eV lower than that of the S_2-MLS state. In addition, the edge shapes are different for these two forms of the S_2 state. These differences could arise from the structure variation discussed in the EXAFS results.

III.F. References

Aasa, R., Andréasson, L.-E., Lagenfelt, G., & Vänngård, T. (1987) *FEBS Lett., 221,* 245

Andréasson, L.-E. (1990) in *Current Research in Photosynthesis* (Baltscheffsky, M., Ed.), Vol. I, pp. 785-788, Kluwer, Dordrecht.

Beck, W. F. & Brudvig, G, W. (1986) *Biochemistry 25*, 6479

Beck, W. F. & Brudvig, G, W. (1988) *Chem. Scripta 28A,* 93

Berthold, D. A., Babcock, G. T., & Yocum, C. F. (1981) *FEBS. Lett. 134,* 231

Bonvoisin, J., Blondin, G., Girerd, J.-J., & Zimmermann, J.-L. (1992) *Biophys. J. 61,* 1076

Boussac, A. & Rutherford, A. W. (1988) *Biochemistry 27*, 3476

Britt, R. D., Zimmermann, J.-L., Sauer, K. & Klein, M. P. (1989) *J. Am. Chem. Soc. 111*, 3522

Brudvig, G. W. (1989) in *Advanced EPR: Applications in Biology and Biochemistry* (Hoff, A. J., ed.), pp.839-863, Elsevier, Amsterdam.

Casey, J. L., & Sauer, K. (1984) *Biochim. Biophys. Acta 767*, 21

Cole, J., Yachandra, V. K., McDermott, A. E., Guiles, R. D., Britt, R. D., Dexheimer, S. L., Sauer, K. & Klein, M. P. (1987) *Biochemistry 26*, 5967

Cramer, S. P., Tench, O., Yocum, M. & George, G. N. (1988) *Nucl. Instrum. Methods A266*, 586

Debus, R. J. (1992) *Biochim. Biophys. Acta 1102*, 269

De Paula, J. C., Beck, W. F., Miller, A.-F., Wilson, R. B., & Brudvig, G. W. (1987) *J. Chem. Soc. Faraday Trans. I 83*, 3635

De Paula, J. C., Innes, J. B. & Brudvig, G. W. (1985) *Biochemistry 24,* 8114

DeRose, V. J., Mukerji, I., Latimer, M. J., Yachandra, V. K., Sauer, K., & Klein,

M. P. (1994) *J. Am. Chem. Soc. 116,* 5239

DeRose, V. J. (1990) Ph.D. Thesis, University of California, Berkeley. Lawrence Berkeley Laboratory Report: LBL-30077

Dismukes, G. C., & Siderer, Y. (1981) *Proc. Natl. Acad. Sci. U.S.A. 78*, 274

Goodin, D. B. (1983) Ph.D. Thesis, University of California, Berkeley. Lawrence Berkeley Laboratory Report: LBL-16901

Goodin, D. B., Yachandra, V. K., Britt, R. D., Sauer, K. & Klein, M. P. (1984) *Biochim. Biophys. Acta 767*, 209

Guiles, R. D. (1988) Ph.D. Thesis, University of California, Berkeley. Lawrence Berkeley Laboratory Report: LBL-25186

Guiles, R. D., Yachandra, V. K., McDermott, A. E., Cole, J. L., Dexheimer, S. L., Britt, R. D., Sauer, K., & Klein, M. P. (1990) *Biochemistry 29*, 486

Guiles, R. D., Zimmermann, J.-L., McDermott, A. E., Yachandra, V. K., Cole, J. L., Dexheimer, S. L., Britt, R. D., Wieghardt, K., Bossek, U., Sauer, K., & Klein, M. P. (1990) *Biochemistry 29*, 471

Haddy, A. & Vänngård, T. (1990) in *Current Research in Photosynthesis* (Baltscheffsky, M., Ed.), Vol. I, pp. 753-756, Kluwer, Dordrecht.

Haddy, A., Dunham, W. R., Sands, R. H. & Aasa, R. (1992) *Biochim. Biophys. Acta 1099*, 25

Haddy, A., Aasa, R. & Andréasson, L.-E. (1989) *Biochemistry 28* , 6954

Hagen, K. S., Westmoreland, T. D., Scott, M. J., & Armstrong, W. H. (1989) *J. Am. Chem. Soc. 111*, 1907

Hansson, Ö., & Andréasson, L.-E. (1982) *Biochim. Biophys. Acta 679*, 261

Hansson, Ö., Aasa, R., & Vänngård, T. (1987) *Biophys. J. 51*, 825

Jaklevic, J., Kirby, J. A., Klein, M. P., Robertson, A. S., Brown, G. S., & Eisenberger, P. (1977) *Solid State Commun. 23*, 679

Kessissoglou, D. P., Kirk, M. L., Bender, C. J., Lah, M. S., & Pecoraro, V. L. (1989) *J. Chem. Soc., Chem. Commun.* 84

Kim, D. H., Britt, R. D., Klein, M. P., & Sauer, K. (1990) *J. Am. Chem. Soc. 112,* 9389

Kim, D. H., Britt, R. D., Klein, M. P., & Sauer, K. (1992) *Biochemistry 31*, 541

Kok, B., Forbush, M., & McGloin, M. (1970) *Photochem. Photobiol. 11*, 457

Li, X., Kessissoglou, D. P., Kirk, M. L., Bender, C. J., & Pecoraro, V. L. (1988) *Inorg. Chem. 27,* 1

MacLachlan, D. J., Hallahan, B. J., Ruffle, S. V., Nugent, J. H., Evans, M. C. W., Strange, R. W. & Hasnain, S. S. (1992) *Biochem. J. 285*, 569

McKale, A. G., Veal, B. W., Paulikas, A. P., Chan, S.-K., & Knapp, G. S. (1988) *J. Am. Chem. Soc. 110*, 3763

McDermott, A. E., Yachandra, V. K., Guiles, R. D., Coles, J. L., Dexheimer, S. L., Britt, R. D., Sauer, K., & Klein, M. P. (1988) *Biochemistry 27*, 4021

Ono, T.-A, Zimmermann, J.-L., Inoue, Y., & Rutherford, A. W. (1986) *Biochim. Biophys. Acta 851*, 193

Ono, T.-A, Nakayama, H., Gleiter, H., Inoue, Y. and Kawamori, A. (1987) *Arch. Biochem. Biophys. 256*, 618

Ono, T.-A & Inoue, Y. (1989) *Arch. Biochem. Biophys. 275*, 440

Pecoraro, V. L. (1988) *Photochem. Photobiol. 48,* 249

Penner-Hahn, J. E., Fronko, R. M., Pecoraro, V. L., Yocum, C. F., Betts, S. D., & Bowlby, N. R. (1990) *J. Am. Chem. Soc. 112*, 2549

Rutherford, A. W. (1989) *Trends Biochem. Sci. 14*, 227-232

Rutherford, A. W., Boussac, A., & Zimmermann, J.-L. (1991) *New J. Chem. 15,* 491

Rutherford, A. W., Zimmermann, J.-L., & Boussac, A. (1992) in *The*

Photosystems: Structure, Function and Molecular Biology (Barber, J., Ed.), pp. 179-229, Elsevier, B. V., Amsterdam.

Sauer, K., Yachandra, V. K., Britt, R. D., & Klein, M. P. (1992) in *Manganese Redox Enzymes* (Pecoraro, V. L., Ed.) pp. 141-175, VCH Publishers, New York.

Sayers, D. E., Stern, E. A., & Lytle, F. W. (1971) *Phys. Rev. Lett. 27,* 1204

Scott, R. A. & Eidsness, M. K. (1988) *Comments Inorg. Chem. 7,* 235

Wieghardt, K. (1989) *Angew. Chem. Int. Ed. Engl. 28*, 1153

Yachandra, V. K., Guiles, R. D., McDermott, A. E., Cole, J. L., Britt, R. D., Dexheimer, S. L., Sauer, K, & Klein, M. P. (1987) *Biochemistry 26*, 5974

Yachandra, V. K., DeRose, V. J., Latimer, M. J., Mukerji, I., Sauer, K., & Klein, M. P. (1993) *Science 260*, 675

Yocum, C. F. (1992) in *Manganese Redox Enzymes* (Pecoraro, V. L., Ed.) pp. 71-83, VCH Publishers, New York.

Zimmermann, J.-L., & Rutherford, A. W. (1984) *Biochim. Biophys. Acta 767,* 160

Zimmermann, J.-L., & Rutherford, A. W. (1986) *Biochemistry 25* , 4609

Chapter IV. Oxidation State Changes of the Mn Cluster in the Flash-Induced S-states of Photosystem II: Determination by X-ray Absorption Spectroscopy

IV. A. Introduction.

The focus of this chapter is to discuss the valence state changes of the Mn cluster at various S-states. As mentioned in chapter I.B.4.1., X-ray Absorption Near Edge Structure (XANES) provides us with direct information about the Mn oxidation states in the OEC. This chapter contains the results of the XANES measurements of the native (as opposed to treated, see IV.A.1.) PSII-enriched membranes poised at different S-states. The formation of these S-states are induced by room-temperature light flashes.

IV. A. 1. The Preparation of the S_3* and S_0* States.

Not long ago the XANES beyond the S_2 state was a challenge to measure, because the XAS required samples with high concentrations which were almost impossible to saturate by single flashes. Special treatments were applied to PSII-enriched membranes to accumulate the S_3* and S_0* states by continuous illumination at low temperatures. The * sign differentiated these chemically induced S-states from the native, flash-induced S-states.

The Klein/Sauer group reported the first XAS study on the PSII membranes poised at the S_3* state by a protocol with "double-turnover, low-temperature" illumination (Guiles et al., 1990b). After dark adaptation for one hour, the PSII-enriched membranes were treated with 5 mM ferricyanide for 10 min at pH 6.5 in the dark to oxidize the non-heme Fe^{2+} as well as the cytochrome b_{559}. Before illumination, DCMU (200 μM) was added to the PSII suspension to block electron transfer between Q_A and Q_B. This treatment ensured that PSII centers were limited to two turnovers; one to reduce Q_A and the other to reduce Fe^{3+}. The S_3* state then was cryogenically trapped by continuous illumination at 240 K for 10 min. The XANES studies on these S_3* samples showed no edge shift relative to the S_2 state.

Guiles and coworkers also reported the first XAS study on the S_0* state employing a protocol in which hydroxylamine was used to reduce the S_1 to an S_0-like state, denoted as the S_0* state (Guiles et al., 1990a). The PSII-enriched membranes were dark-adapted for 1 h and treated with a low concentration (40 μM) of hydroxylamine for 30 min. Again 50 μM of DCMU was added to the membrane suspension to secure a single-turnover reaction in PSII. After continuous illumination at 195 K, the S_0* state was trapped at 77 K. A shift to lower energy was observed in the edge position of the XANES associated with the $S_1 \rightarrow S_0^*$ transition. The edge position as well as the analyses of the EXAFS indicated the presence of one Mn(II) in the S_0^* state.

IV. A. 2. The Damping of the Flash-Yield Oscillation.

When oxygen evolution or the MLS induced by short single-turnover saturating flashes was measured as a function of the flash number, a period-of-four oscillation pattern was observed (Joliot et al., 1969; Dismukes & Siderer, 1981). Although a periodicity of four was still evident during the second cycle, the oscillation was more damped. The damping of the flash-yield oscillation was suggestive of an increasing degree of disorder of the S-state advancement. Two parameters, misses (α) and double hits (β), were introduced by Kok and coworkers to explain this damping effect (Kok et al., 1970).

Double hits (β) were anticipated if the duration of the flashes was not negligible compared with the dark relaxation time required for Q_A^- reoxidation. Double hits could be largely avoided if very brief flashes were used to induce the S-state transition. Joliot and Kok observed no oxygen evolved upon the second flash if they used short flashes. The duration of flashes from a Xe-lamp was difficult to judge precisely because a tail following the discharge was unavoidable. Flashes induced by Q-switched laser, however, provided a better-defined duration. Weiss and coworkers found no oxygen evolution in the second flash, even with high flash energies, by using very brief laser flashes (2 nsec) (Weiss et al., 1971).

The misses (α) caused decay in the oscillation. This resulted in damped flash yields even when double hits were eliminated. The number of misses was found to be independent of the flash intensity as long as it was at or above the saturation level (Joliot & Kok, 1975). The misses were first explained by Joliot and Kok by the following two mechanisms, which I will designate as (a) and (b). In mechanism (a), the misses occur because the light advancement of the $S_n \rightarrow S_{n+1}$ does not occur in a small fraction of the PSII centers. In mechanism (b), the misses arise from a back-reaction which reverses the effect of the photoreaction. Joliot and Kok also proposed that both the misses and double hits must occur randomly in all reaction centers in order to explain the damping of the oscillation in their experiments (Joliot & Kok, 1975).

IV. A. 3. The Synchronization of the S-state Formation.

PSII samples with specific and well-defined S-state composition after each flash are necessary in studies of the different S-states by spectroscopic methods. One straightforward approach is to reduce the values of α and β. As mentioned in the end of Section IV.A.2, mechanisms (a) and (b) are the main contributions to the misses. In our experiments, the smallest possible value of α is ensured by applying saturating flashes to the PSII samples. In addition, mechanism (a) also depends on the properties of different PSII preparations. As will be described in the Results, Type-1 PSII samples (See Section IV. B.) have a large α upon the second flash, possibly owing to the presence of an impaired Q_B site.

Mechanism (b) proposed by Joliot and Kok involves a back-reaction between the higher S-states (S_2 and S_3) and the reduced quinone acceptors (Q_B^-). Another pathway responsible for the decay of the S_2 and S_3 population in the dark involves reduction of the S_2 and S_3 states by reduced Y_D (Babcock & Sauer, 1973; Velthuys & Visser, 1975; Vermaas et al., 1984; Styring & Rutherford, 1987). To decrease the extent of the two recombination reactions, two treatments have been applied to all of the PSII samples reported in this chapter. The first treatment is the addition of PPBQ (phenyl-*p*-benzoquinone) to the PSII samples as an exogenous electron acceptor, and to keep Q_B oxidized. The second is the "pre-flash" treatment: each PSII sample is given two pre-flashes. The rationales for these treatments are described in detail below.

IV. A. 3. 1. PPBQ Treatment.

In continuous light, Y_D becomes oxidized in all PSII centers, and the $Y_D^+S_0$, $Y_D^+S_1$, $Y_D^+S_2$, and $Y_D^+S_3$ are equally populated. Unlike Y_Z^+, Y_D^+ is stable in the dark for minutes to hours (Babcock & Sauer, 1973; Lozier & Butler, 1973). When the light is switched off, S_2 and S_3 decay to the S_1 state by recombining with the electrons from Q_B^- (Rutherford et al., 1982; Lavergne & Étienne, 1981). In the absence of exogenous electron acceptors, the decay-half times for the S_2 and S_3 states have been determined to be 35 and 40 s, respectively (Forbush et al., 1971; Boussac et al., 1985). To extend the lifetime of the S_2 and S_3 states, an exogenous quinone acceptor (e.g. PPBQ) is often added to the PSII-enriched membranes to slow these recombination reactions. The increased stability of the S_2 and S_3 states at 18 °C has been measured in the presence of PPBQ, with the values of the half-decay time of 3-3.5 min and 3.5-4 min, respectively (Styring & Rutherford, 1988). The flash interval in our experiment is typically 1.5 s, and the PSII samples are frozen within 1-2 s in liquid nitrogen after the last flash (see IV.B.2). Therefore, in the presence of PPBQ, the possible loss of S_2 and S_3 due to recombination after one or two flashes should be negligible.

The reason that PPBQ can prolong the lifetime of the higher S-states is described as follows. After the first flash, Q_A^- reduces PPBQ, and the resulting semiquinone oxidizes the Fe^{2+} of the acceptor side complex (Zimmermann & Rutherford, 1986; Petrouleas & Diner, 1987). This results in the formation of the S_2-Q_A-Fe^{3+} state in which there is no electron available on the acceptor side to recombine with the S_2. Upon the second flash, Fe^{3+} is reduced by an electron from the OEC via Q_A, and the S_3-Q_A-Fe^{2+} state forms. Again there is no electron available on the acceptor side to recombine with the S_3 state. The long-lived S_2 and S_3 states have also been observed when other electron acceptors were used (Beck & Brudvig, 1986) or in leaves when Q_B was oxidized (Rutherford et al., 1984).

In the presence of PPBQ, the source and the reaction pathway for the reducing equivalents to deactivate the S_2 and S_3 states in the dark are not known. However, a direct back-reaction with fully reduced $PPBQH_2$ (occupied at the Q_B site) is not expected to occur, because a high concentration of oxidized PPBQ is present. The oxidized PPBQ probably has a higher affinity for the Q_B site than the reduced form. Therefore, the possible source to deactivate the S_2 and S_3 states is more likely to be exogenous electron donors, possibly $PPBQH_2$ (Styring & Rutherford, 1988).

IV. A. 3. 2. Pre-Flash Treatment.

The purpose for the pre-flash treatment to the PSII samples is to eliminate the dark pathway in which the S_2 and S_3 population decays through a recombination reaction with reduced Y_D in the seconds time scale (Babcock & Sauer, 1973; Velthuys & Visser, 1975; Vermaas et al., 1984; Styring & Rutherford, 1987). The presence of the reduced Y_D in the PSII samples mainly results from the reduction by the S_0 state (See next paragraph).

As described in the previous section, the states of $Y_D^+S_0$, $Y_D^+S_1$, $Y_D^+S_2$, and $Y_D^+S_3$ are equally populated in continuous light. When the light is off, $Y_D^+S_2$ and $Y_D^+S_3$ decay to $Y_D^+S_1$ by recombining with the electrons from the non-specific electron donors in the presence of PPBQ. In addition to this reaction, a slow conversion of the S_0 to S_1 state at room temperature in the dark has also been reported (Styring & Rutherford, 1987). The results indicate that Y_D^+ accepts an electron from the S_0 state in a dark reaction, then Y_D and the S_1 state are subsequently formed. The $t_{1/2}$ for this reaction is ~35 min and ~20 min in PSII-enriched membranes and thylakoid membranes, respectively (Messinger et al., 1993; Styring & Rutherford, 1987). Therefore, after ~ 1 h of dark adaptation, PSII centers are present as: 1) 75% of the $Y_D^+S_1$ state, which arises from the deactivation of the S_2- and S_3-states; and 2) 25% of the Y_DS_1 state (possibly containing some residual $Y_D^+S_0$ state), resulting from the recombination reaction between the S_0 state and Y_D^+.

After two pre-flashes, the PSII centers described at the end of the last paragraph convert into 1) 75% of $Y_D^+S_3$, and 2) 25% of Y_DS_3 (with a residual amount of $Y_D^+S_2$) states. At room temperature in the dark with the presence of PPBQ, centers of the $Y_D^+S_3$ and $Y_D^+S_2$ states will decay into the $Y_D^+S_1$ state due to reduction by non-specific electron donors (possibly other endogenous reductants, like $PPBQH_2$), with a half-life time of 3-4 min as mentioned in Section IV.A.3.1. Those in the Y_DS_3 state will rapidly deactivate to form the $Y_D^+S_2$ centers in the seconds time scale (Babcock & Sauer, 1973; Velthuys & Visser, 1975; Vermaas et al., 1984; Styring & Rutherford, 1987; Vass & Styring, 1991), then eventually decay to the $Y_D^+S_1$ state. Therefore, after two pre-flashes, the PSII centers relax and collect in the $Y_D^+S_1$ state.

As a summary, the pre-flash treatment is used to synchronize the PSII centers to the $Y_D^+S_1$ state before the samples receive the subsequent flashes. It is important to eliminate the amount of reduced Y_D present in the PSII samples. Compared with the reaction time (in the seconds time scale) for the dark recombination reactions ($Y_DS_n \rightarrow Y_D^+S_{n-1}$, n=2 or 3), the interval time between the Xe flashes (~1.5 s, See IV. B.) used in our experiments cannot be ignored. Considering that almost all of the Y_D is oxidized after two pre-flashes, these dark recombination reactions are no longer important, and therefore the S-state population will be less scrambled.

One more process related to the reduction of Y_D^+ is worth mentioning here. The reduction of Y_D^+ has been reported to progress biphasically, with pH- and temperature-dependent half-times in the tens of minutes and hours time range (Vass & Styring, 1991). In addition to the $Y_D^+S_0 \rightarrow Y_DS_1$ reaction described above, the slower process is responsible for the $Y_D^+S_1 \rightarrow Y_DS_1$ reaction. The half-time for the latter process is in the hours scale. However, the contribution of this process can be ignored during the 1 h dark adaptation after two pre-flashes. This is because at room temperature the half-time for this process is much larger than 9 h (Vass & Styring, 1991). Therefore, the approximate initial distribution of the S-states should not be influenced by this reaction, and still remains to be 100% $Y_D^+S_1$ state.

IV. B. Material and Methods.

IV.B.1. Preparation of PS II-Enriched Membranes.

PSII membranes prepared by both Type-1 and Type-2 protocols were used in this study. These protocols were described in chapter II. The PSII membrane pellets were washed in medium A with 50% glycerol as the cryoprotectant, then resuspended to a final Chl concentration of 4-5 mg/ml.. The samples for X-ray absorption studies were prepared by loading these PSII membrane suspensions directly onto two types of lucite sample holders with two different thicknesses. The flash source can saturate higher concentrations of the PSII membranes filled in the thinner sample holders. All of the flash-induced illuminations, EPR and X-ray absorption measurements were performed directly on samples mounted in these holders. The samples were dark-adapted for at least 1 hr at 4 ^oC before being frozen to 77 K in liquid nitrogen. The amplitudes of the Y_D^+ EPR signal were measured and used to correct for sample volume fluctuations. The samples were then equilibrated to room temperature (22 -24 ^oC) in the dark for at least 20 min, before the following flash procedure was applied.

IV.B.2. Flash-Induced Illuminations.

Two flash sources were used to advance the PSII centers:

(1) a Xe flash lamp (CHH 174, ILC Inc.) which gave white flashes of 14 μs FWHM and 40 μs FWTM. The light was directed to the samples by a light guide.

(2) a Q-switched Nd-YAG laser which provided green flashes (532 nm) of 7 ns FWHM. The output laser beam was expanded and collimated to the larger dimension

of the sample area, then focussed by a cylindrical lens to match the smaller dimension. The sample cells were mounted horizontally and illuminated with these two light sources at room temperature as described in chapter II.

Each sample received two pre-flashes to minimize the content of reduced Y_D (see Introduction), followed by dark adaptation at room temperature for 60 min. This procedure synchronized the PSII centers to the $Y_D^+S_1$-state. Then the samples were given 0, 1, 2, 3, 4, or 5 flashes, with 1.5 s intervals. After the last flash the samples were frozen immediately (within 1-2 s) in liquid nitrogen. The EPR-spectra (both Y_D^+ and the MLS) were collected, and the samples were stored at 77 K for further use in the XANES experiments (usually within one week).

IV.B.3. EPR Measurements.

Spectroscopic conditions for EPR measurements were mentioned in chapter II. Typically 1-4 scans were averaged. The MLS-signal was quantitated by adding the peak-to-trough amplitudes of three low-field and three high-field lines. After the XANES experiment the EPR spectra of the samples were re-measured. The amplitude of the MLS was typically $\geq 80\%$, relative to that measured before the X-ray exposure. In addition, no free Mn^{2+} EPR signal was detected in any of these samples. This indicated that no significant radiation damage occurred during the data collection (approximately 6-8 hours).

IV.B.4. XANES Measurements.

Most of the manganese X-ray absorption K-edge spectra were collected at the wiggler beamline VII-3 at the Stanford Synchrotron Radiation Laboratory (SSRL) during dedicated operation of SPEAR (40 - 100 mA at 3.0 GeV); some were collected at the bending magnet beamline X-9B at the National Synchrotron Light Source

(NSLS) (100 -250 mA at 2.5 GeV). An unfocussed X-ray beam was used. A Si <220> double-crystal monochromator was used, with the second crystal detuned to 50% of the maximum flux to reduce the transmission of the harmonics. Typically the beam was narrowed to 11x1 mm by a slit. The sample was maintained at 10 ± 1 K in a liquid helium cryostat (Oxford Intruments, CF1204). A 13-element Ge solid-state detector (Canberra Intruments) was used as described in Chapter II.

Spectra were recorded from 6520 - 6580 eV, with a density of 5 points per eV and a dwelling time of 3 s per point. The beam intensity was monitored continuously, and the fluorescence signals were corrected for fluctuations in the incoming beam. Energy calibration and resolution were monitored by simultaneously measuring the absorption spectrum of $KMnO_4$, using its narrow pre-edge "white-line" at 6543.30 eV. The FWHM of this "white-line" was typically less than 1.7 eV.

IV.B.5. XANES Data Analysis.

Usually 16-20 scans were collected for each sample, and the individual detector traces were added. A linear or a Gaussian-tail background was fit to the signal from 6520 - 6535 eV (i.e. before the pre-edge), and subtracted from the data. The maximum of the absorption edge was then normalized to unity. The inflection point energy was determined from the zero-crossing point of the second derivative of the spectrum, which was generated by analytical differentiation of a third-order polynomial fit to the data over an interval of ± 3.0 eV on each side of a data point. The uncertainty in inflection point energy is estimated to be ± 0.05 eV for each individual sample.

IV. C. Results.

Three groups of the PSII-enriched membranes have been prepared and measured by EPR and XANES. They are denoted as Type-1_Xe, Type-1_Nd, and Type-2_Xe. Type-1 and Type-2, referring to BBY-type and KM-type membrane preparations respectively, are the two different protocols of PSII preparation used in this study (See Chapter II). Xe and Nd stand for the Xe-lamp and Nd-YAG laser, respectively.

IV.C.1. Synchronization of the S-State Advancement.

It is important that the PSII samples poised at various S-states be synchronized before the flashes, and be able to advance coherently after each flash. The basic requirement to fulfill this is to acquire enough flash intensity to saturate our PSII samples. First, we determined the flash-intensity dependence of the MLS amplitude induced by one flash from the Xe lamp. 95% of the MLS is produced when the flash intensity is 60% of the maximum intensity. Further reducing the flash intensity to 25% still yields 80% of the MLS (data not shown).

Moreover, we compare the MLS amplitude induced by one flash with that from an identical S_2 sample generated by the continuous illumination protocol (10 min at 195 K). The latter method is commonly used to generate a maximal amount of the S_2-state (Brudvig et al., 1983). Within the accuracy of the amplitude determination (sample-to-sample variation of ±10%), either one flash (from both the Xe-lamp or the Nd-YAG laser) or continuous illumination generates the same amount of MLS.

In addition, the PSII-enriched membranes have been given two pre-flashes to synchronize the PSII centers to the S_1 state, and PPBQ was added before the pre-flash treatment to decrease the recombination between the S_2 or S_3 states and Q_B^- (See IV. A. 3.). A verification of the Y_D^+-EPR spectra confirms our expectation that no significant recombination should occur after the first and second flashes in our samples. After the pre-flash treatment, the amplitude of the Y_D^+ EPR signal typically increases by 30-50%. This indicates that the application of the two pre-flashes decreases the amount of reduced Y_D present in the sample, thus minimizing the possibility of recombination between the higher S-states and Y_D. No Chl^+-signal is detected. The application of 0-5 flashes after the pre-flash treatment does not further increase the Y_D^+ EPR signal. Moreover, the same MLS amplitude is detected from the S_2 samples generated either from the low-temperature illumination procedure or by one single flash. These results further confirm that no significant amount of recombination occurs between the Y_D and S_2 state.

IV. C. 2. The Flash Dependence of the MLS.

The MLS amplitudes as a function of the flash number for Type-1_Nd and Type-2_Xe are graphed in Fig. IV-1. The MLS generated within each group are normalized to that of the one-flash sample. Samples which are given zero flashes after the pre-flash treatment exhibit no detectable MLS. This indicates that the length of the dark adaptation time after two pre-flashes (at least 60 min) was sufficient to have virtually all of the S_2 and S_3 states relax back to the S_1 state. In our experiments, the largest yield of the MLS comes after the first flash.

Table IV-1 lists the percentage of the MLS amplitude after 0-5 flashes in the three groups of samples. Again MLS amplitudes are normalized to the yield following the first flash. The MLS of Type-2 samples after two flashes decreases to 26% of the 1-flash value (Fig. IV-1b, solid trace), and almost disappears after three

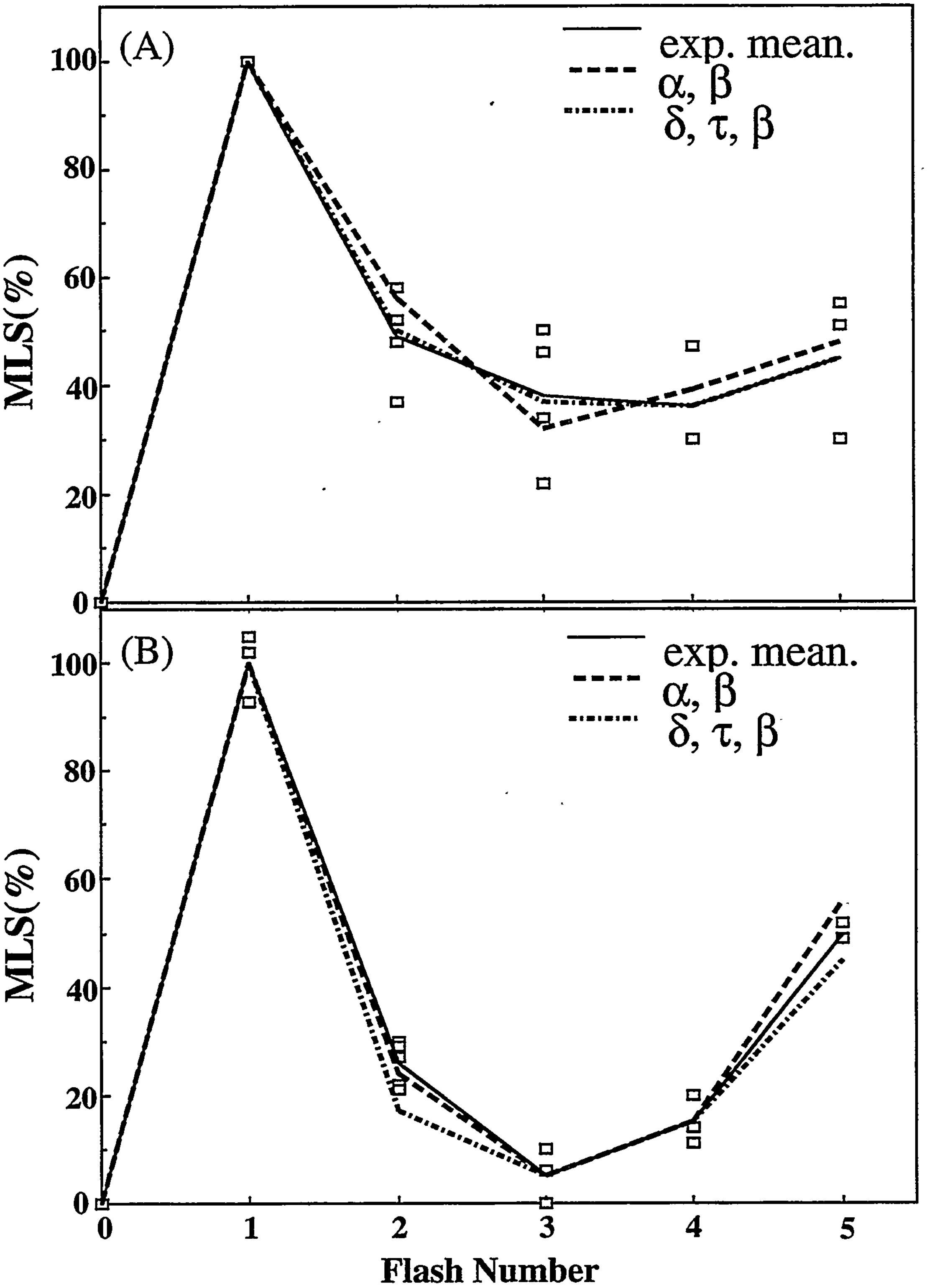

Fig. IV-1. Flash-induced EPR MLS oscillation patterns of PSII samples of (A) Type-1_Nd and (B) Type-2_Xe. Shown here are MLS of individual samples (open squares) and the average of 2-4 series (—). The MLS patterns are fitted to the traditional Kok model (----), or the extended Kok model (-.-.-). The MLS amplitudes are normalized to that of the first flash sample.

Table IV-1. The Flash Dependence of the Intensity of the MLS in Synchronized PSII-enriched Membranes. The samples were synchronized as described in the Materials and Methods section. Flash dependence of the MLS yields (shown in percentage) was obtained by normalizing the MLS calculated from all the samples in the same group (column) to that of the one-flash sample. Numbers were obtained from the average values of 2-4 identical series in each group of samples.

	Type-1_Xe (%)	Type-1_Nd (%)	Type-2_Xe (%)
0 Flash	0	0	0
1 Flash	100	100	100
2 Flash	49	51	26
3 Flash	38	37	5
4 Flash	36	28	15
5 Flash	45	52	50

flashes. The fourth flash then slightly increases the MLS. After five flashes, the MLS recovers up to 50% of the maximum value. The MLS amplitudes described above clearly show a pattern of period-of-four oscillation which peaks at the first and fifth flashes. This behavior corresponds well to the traditional Kok-model for the S-state advancement (Kok et al., 1970).

However, for Type-1 samples the behavior of the MLS amplitude is less straightforward. Although a period-of-four oscillation is still evident, the overall pattern is strongly damped. Following the second flash the PSII membranes still exhibit ~50% of the first-flash MLS (Fig. IV-1a, solid trace). The third and fourth flashes decrease and the fifth flash increases the MLS amplitude, all to a small extent. The mean value of the MLS percentages of 2-5 flash is higher. Note that this is most likely not a matter of damping of the oscillations by misses and double hits (see next section).

IV. C. 3. Modeling the S-State Advancements.

On the basis of the flash number dependence of the MLS amplitude (Fig. IV-1), the actual S-state distribution after each flash can be estimated using the traditional Kok model from the knowledge of the following three parameters: misses (α), double hits (β), and the initial (dark-adapted) distribution (σ) of the two stable states, S_0 and S_1. Because the PSII centers have been synchronized to almost 100% of $Y_D^+S_1$ state before the flashes, the ratio of the initial S_0/S_1 states σ is approximately 0. In addition, the contribution to misses due to loss of the S_2 and S_3 states by reduced Y_D after the first and second flashes is not significant (See section IV. A. 3).

Parameters α and β are obtained by fitting the flash-induced MLS-oscillation amplitudes (listed in Table IV-1) using the traditional Kok model. α and β from the

Table IV-2. Fits to the flash-induced MLS-oscillation patterns of PSII membranes, according to an extended Kok model.[a]

(a) Traditional Kok Model.

	α (%)	β (%)
Type-1_Xe	28	17
Type-1_Nd	30	12
Type-2_Xe	12	5

(b) Extended Kok Medol.

	δ (%)	τ (s)	γ[b] (%)	β (%)
Type-1_Xe	65	3.8	47	5
Type-1_Nd	69	4.0	51	0
Type-2_Xe	62	0.9	16	5

[a] Type-1 or Type-2 PSII membrane preparations, given Xenon flashes (Xe) or Nd-YAG laser flashes (Nd).

[b] $\gamma = \delta * \exp(-1.5/\tau)$; see text for details.

best fits for the three groups of samples are listed in Table IV-2a. The fitting results show that the traditional Kok model is suitable only for Type-2_Xe samples, whose MLS amplitudes can be fitted with reasonable values of α and β (0.12 and 0.05, respectively). For either Type-1_Xe or Type-1_Nd samples, however, α and β are unreasonably high (~0.30 and ~0.15, respectively). These high misses and double hits are not in agreement with the results of our saturation tests, (See Section IV. C. 1) and therefore are unlikely to happen in the samples.

The flash number dependence of the MLS amplitude computed on the basis of the traditional Kok model, using the best α and β parameters given above, is also shown in Fig. IV-1 (---- traces). As may be seen, the computed MLS pattern of Type-2_Xe samples agrees well with the experimental MLS trend using the traditional Kok model. However, the agreement for Type-1 samples is much worse. The fitting trace tends to underestimate the observed damping of the MLS oscillation.

To test wether slightly incomplete synchronization in PSII centers accounts for the MLS trends of the Type-1 samples (using the traditional Kok model), the flash dependence of the MLS amplitude is fitted again as described above with 0-10% of S_0 in the initial state. The resulting parameters α and β from the best fits are then used to compute the MLS trends, and are compared with experimental data. Fig. IV-2 shows the comparison of 0% S_0 with 10% S_0 together with the experimental MLS trends from Type-1_Xe samples. The MLS oscillation patterns for 0% S_0 and for 10% S_0 initial state are relatively similar compared with that of the experimental data. The values of α and β from the best fits of the MLS amplitudes with 10% S_0 in the initial state are close to those with 0% S_0 in the initial state (Fig. IV-2). Hence, the MLS trends cannot be explained by the presence of 10% S_0 in the initial state.

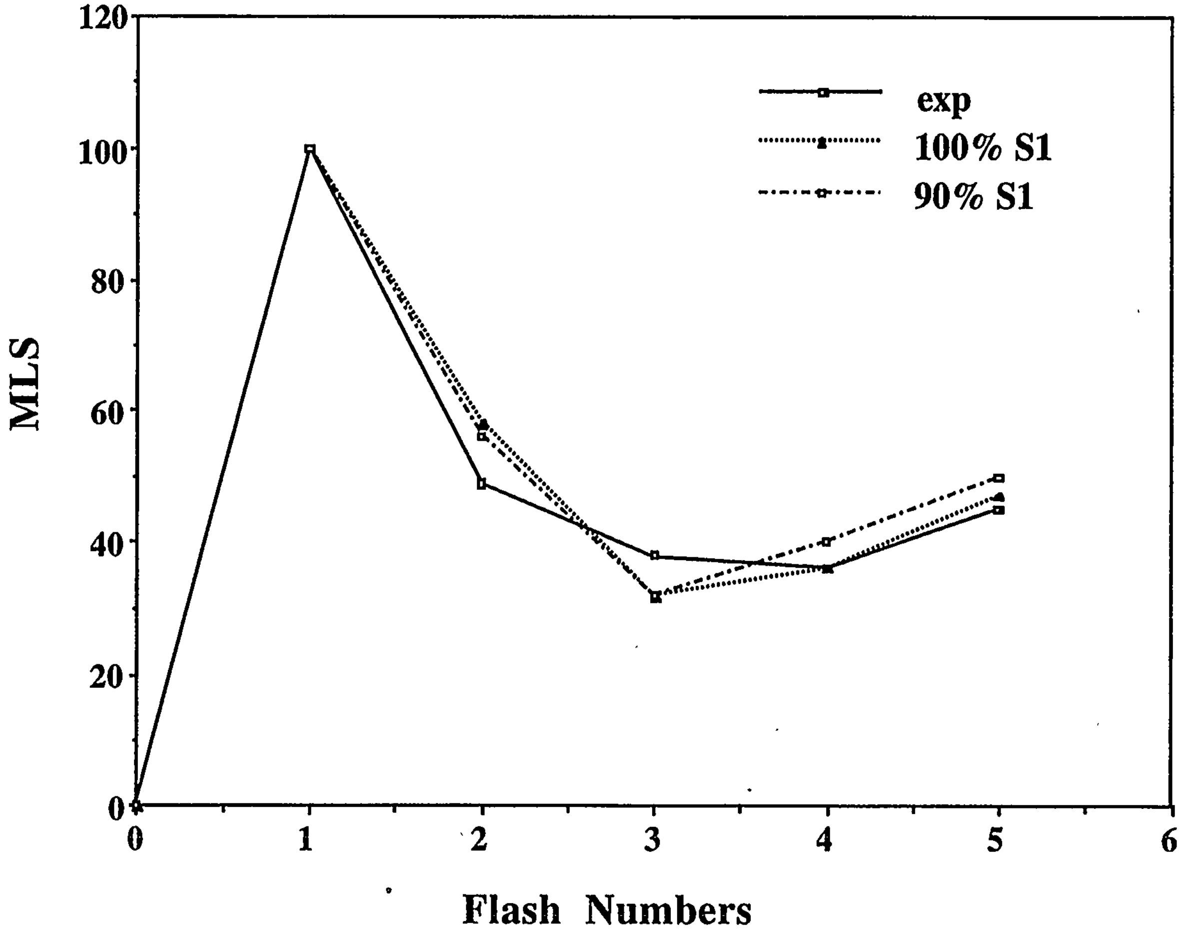

Fig. IV-2. Comparison of the experimental and computed MLS trends using parameters α and β obtained from the best fits using the traditional Kok model with 0% (·······) and 10% S_0 (· -· -·) present in the initial states. Parameters α and β are: for 0% S_0: α =0.28, β =0.17; for 10% S_0: α =0.25, β =0.16.

Therefore, it is clear that an extension of the traditional model may be necessary to describe the MLS trends of the Type-1 samples. As already pointed out, it seems as if the normal period-four oscillation is superimposed by an offset, from the second flash onwards. It is also rather clear that, as stated above, this cannot be explained by the traditional Kok model with high values for α and β, or by a slightly non-synchronized initial state. One possible origin for such an offset is an acceptor-side impairment, in which the re-oxidation of Q_A^- is retarded to an extent that a fraction of the PSII has not reopened in time for the next flash to fully allow the next S-state advancement. Such retardation might be related to detergent-induced changes at the Q_B binding site which result in a delay of Q_A^- oxidation by Q_B (or by PPBQ). Normally this electron transfer process takes place within 100-200 μs (Bowes & Crofts, 1980; Robinson & Crofts, 1983; Crofts & Wraight, 1983). Q_B site impairment has been proposed by Ono and coworkers (personal communication). This impairment may account for decrease of the electron transfer from 100-200 μs to the second time scale.

The behavior of the flash-dependent MLS observed in Type-1 samples can be well explained by the arguments proposed above. The first flash effectively turns over all the PSII centers, except the normal fraction (~10%) of misses. As discussed above, the dark adaptation time (at least 60 min) between the two pre-flashes and the following flashes is sufficient for Q_A^- in all the reaction centers to be reoxidized . However, starting from the second flash, a fraction (say, δ) of the PS II centers is still closed and therefore fails to follow the S-state advancement. In other words, δ of PSII centers stay in the S_2 state upon the second flash, because the Q_A^- in this fraction of reaction centers is not yet oxidized by PPBQ within 1.5 s, which is a typical interval time between the flashes.

Upon the third flash, that is 3.0 s after the first flash, a fraction of δ stranded in

S_2 after two flashes is able to advance to the S_3 state, because Q_A^- in this fraction is oxidized already. The rest of δ is still at the S_2 and will need more time to have their Q_A^- to be oxidized. On the other hand, another fraction of ~1-δ of the PSII centers, which was able to advance to the S_3 state upon the second flash, is now facing the same fate of not being able to advance because of the non-oxidized Q_A^- present in these centers. The scenario continues until enough time (and therefore enough flashes) passes, when all of the PSII centers have their Q_A^- reoxidized. Obviously, the outcome of all of these activities in the PSII centers is a much more scrambled S-state distribution after the second flash and a damped period-of-four MLS pattern, as observed in Type-1 membranes (Fig. IV-1a). The (time-dependent) fraction δ of centers stranded in S_2 will lead to a much damped MLS oscillation pattern..

The story described in the last paragraph can be considered as a non-traditional miss parameter that is zero for the first flash but becomes dependent on the time after the first flash. A modified Kok model (denoted as the extended Kok model) including the concept discussed above is then introduced to describe the MLS behavior of the Type-1 samples. In the extended Kok model, the traditional misses are described as a function of δ, where δ is the fraction of the PS II centers that exhibit slow Q_A^- reoxidation, with a pseudo first-order lifetime τ. The quantity γ ($\gamma=\delta*\exp(-\Delta t/\tau)$, Δt is the interval time between two consecutive flashes) describes the fraction of PSII centers which are still closed upon the next flash. Hence, γ can also be considered as a modified miss parameter, but which depends on flash numbers and S-states. Double hits β is still used in the extended Kok model because it depends only on the duration of the flashes.

Listed in Table IV-2(b) are the best values for the fit parameters (Q, τ, and β) using the extended Kok model to describe the MLS-oscillation patterns of the three groups of PSII samples. Also shown in Fig. IV-1 are the fitting results (- · - · - trace). Compared with that using the traditional Kok model, the MLS trace of Type-1_Nd samples are more accurately described by the extended Kok model. On the other hand, for Type-2 samples, the extended model does not improve the fit. In addition, the fit results (Table IV-2b) show that, as expected, the double hits β drops to zero when a ns Nd-YAG laser is used as the flash source. However, for the Xe-flashes, some double hits occur (5%).

A summary of the fit results shown in Table IV-2 is as follows. For PSII-enriched preparations with reasonably good MLS-oscillation patterns (i.e. Type-2 samples), the traditional Kok model gives an accurate description of the S-state advance. However, in the presence of a lag in Q_A^- reoxidation (possibly due to a modified Q_B site), the extended Kok model proposed is better. From these results, the S-State compositions for both types of samples given 0-5 flashes are calculated and are listed in Table IV-3.

Table IV-3 also displays the percentages of the S-states formed after a specific number of flashes. For Type-2 samples, the population of the S_2 state after one flash is 83%. After two flashes, 70% of the PSII centers are present at the S_3 state, 5% better than the percentage reported for the S_3* state (65%, Guiles et al., 1990b). Upon the third flash, 60% of the PSII centers are at the S_0 state. However, for Type-1 samples, the best fit shows only 49% of the PSII centers are able to advance to the S_3 state after two flashes due to the distortion of the Q_B site as mentioned above. This delay further results in a poorer percentage obtained for the S_0 state after the third flash. The outcome of these events is a much damped MLS oscillation trend as seen in experimental data.

Table IV-3. S-state Composition of Flash-Induced PSII Membranes, as Calculated from the Fits to the MLS-Oscillation Patterns.

	Type-1_Nd $\beta = 0.0$, $\delta = 0.69$, $\tau = 4.0$ s				Type-2_Xe $\alpha = 0.12$, $\beta = 0.05$			
Flash Number	S_0 (%)	S_1 (%)	S_2 (%)	S_3 (%)	S_0 (%)	S_1 (%)	S_2 (%)	S_3 (%)
0	0	100	0	0	0	100	0	0
1	0	0	100	0	0	12	83	5
2	0	0	51	49	8	2	20	70
3	36	0	38	26	60	11	4	25
4	10	32	28	29	28	52	12	7
5	15	4	52	29	10	30	46	14

IV. C. 4. Mn K-Edge Spectroscopy.

The XANES results measured from the three groups of samples (Type-1_Xe, Type-1_Nd and Type-2_Xe) are described in this section. Each group contains 2-4 complete series of samples (from 0 to 5 flashes).

We use the first inflection points rather than the "half-height energies" to characterize the edge positions of our samples. To determine the edge energies by the half-heights is less favorable because it is extremely sensitive to how the edge spectra are normalized, or where the "minimum" and "maximum" points of the spectra are selected. It is nearly impossible to ensure perfect normalization on all samples because the choice of the minimum and maximum points may not be unique due to the following two aspects. First, curved background is usually present in these dilute flash-induced samples. Incorrect pre-edge background removed certainly makes the determination of the minimum point unreliable. Second, the energy position of the edge maximum may differ among the S-statea if changes of edge structure are involved in the flash-induced transitions. This influences the determination of the maximum point of the edge. Both aspects mentioned above need to be considered carefully if half-height energies are chosen to represent the edge positions. Arbitrarily choosing the maximum and minimum points will possibly result in distortions of the XANES results.

IV. C. 4. 1. Flash-Induced Changes in Edge Energies.

The inflection point energies (I.P.E.) measured from the three groups of samples are listed in Table IV-4. Also shown in Fig. IV-3 are the I.P.E. as a function of the flash numbers measured in sample groups Type-1_Nd (a) and Type-2_Xe (b). The first flash shifts the edge energy from 6551.6 eV to 6553.5 eV, with a net positive

Table IV-4. The K-edge Inflection Point Energies upon Different Number of Flashes Measured on Synchronized PSII-enriched Membranes[a,b].

	Type-1_Xe (eV)	Type-1_Nd (eV)	Type-2_Xe (eV)
0 Flash	6551.95	6551.47	6551.78
1 Flash	6553.16	6553.44	6553.50
2 Flash	6553.42	6553.73	6553.66
3 Flash	6551.07	6550.46	6550.51
4 Flash	6551.90	6551.00	6551.00
5 Flash	6552.06	6551.41	6552.95

[a] The samples were synchronized as described in the Materials and Methods section.

[b] Numbers were obtained from the sample described in Table IV-1.

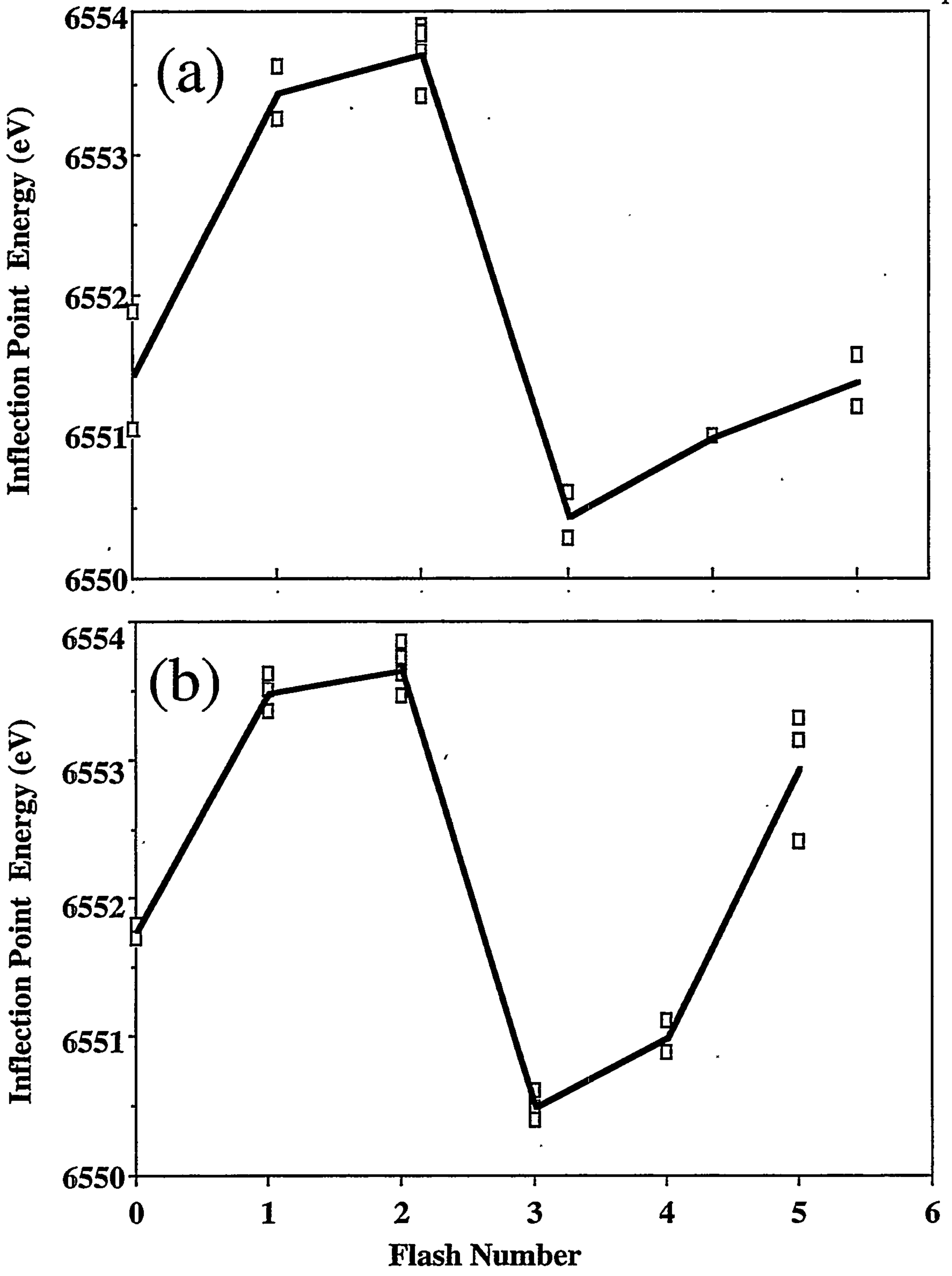

Fig. IV-3. Flash-induced inflection point energy (I.P.E.) as a function of the flash numbers measured in sample groups (a) Type-1_Nd, and (b) Type-2_Xe. Shown here are the edge energy from individual samples (open square) and the average of 2-4 series(—).

edge shift of 1.8±0.2 eV. Upon the second flash, the edge position shifted higher by only 0.2-0.3 eV in each of the three groups of samples. Applying the third flash shifts the edge energy downward to ~6550.5 eV, which is well below that of the zero-flash sample. The edge positions shift back to higher energy again after the fourth and fifth flashes. The much smaller shift upon the fifth flash from the Type-1 samples is due to the larger extent of the S-state dephasing as discussed in the previous sections.

The positive edge shift upon the first flash confirms the well-accepted concept that the Mn cluster is oxidized during the $S_1 \rightarrow S_2$ transition. The relatively small edge shift upon the second flash indicates that the edge position of the Mn cluster in the S_3 state is likely to be similar to that in the S_2 state. In addition, after three flashes the edge position is at much lower energy than that of the S_1 state. This is suggestive of a significantly lower edge energy for the S_0 state.

IV. C. 4. 2. Construction of the Pure S-state Edge Spectra.

The Mn K-edge XANES spectra of the "pure" S_0-S_3 states can be constructed by linear combination of the flash-induced XANES spectra. First, the parameters obtained from the best fits of either the traditional (α and β) or extended (δ, τ, and β) Kok model are used to calculate the S-state composition, as shown in Table IV-3. Then, the coefficients for performing linear combinations are acquired by inverse transformation of the matrices obtained in the last step. Note that there are only four unknown S-states (S_0-S_3) to be extracted, while six groups of the S-state composition are available (0-5 flashes). Ideally, any choice of four among these six relations should give us sufficient determination of the coefficients. In practice, we choose the four XANES spectra induced from 0-3 flashes to construct the matrix, because larger errors and more scrambling are expected in the XANES for higher flashes (4 and 5).

Fig. IV-4 illustrates the four "pure" S-states constructed according to the methods described above. We can further simulate the 4- and 5-flash XANES spectra using these "pure" XANES spectra of the S_0-S_3 states and the percentages of the S-state composition shown in Table IV.-3. A comparison of these simulated and experimental XANES spectra for 4- and 5-flash samples then serves to check the goodness of these "pure" spectra of the S_0-S_3 states. Fig. IV-5 displays a typical result of the goodness check; both of the 4- and 5-flash samples show good agreement within noise level. The averaged XANES spectra obtained by summing all of the three groups of samples are shown in Fig. IV-4.

The corresponding second derivatives of Fig. IV-4 are displayed in Fig. IV-6. A vertical dashed line is drawn at the inflection point energy (I.P.E.) of the S_1 state. Reproducible changes of features in the second derivatives are found in these S-states. Similar to the XANES for the thick samples described in Chapter III (Section III. C. 2.), feature X increases in the $S_1 \rightarrow S_2$ transition for the flash-induced samples (Fig. IV-6). This feature stays relatively unchanged with advance of the S_2 to S_3 state. However, feature X is missing in the S_0 state. In addition, compared with those of the S_1, S_2, and S_3 states, the second derivatives of the K-edge spectra (between 6545-6555 eV) in the S_0 state have a much narrower and taller shape. This shape is reminiscent of the presence of Mn(II) as based on the results from the synthetic Mn(II) model compounds (Yachandra et al., 1993).

The I.P.E.'s of these calculated pure S-state spectra obtained from the three groups of PSII samples are shown in Table IV-5. The edge energy of each S-state agrees reasonably well among all three groups of samples. This coherence again confirms that the extended Kok model accounts reasonably well for the rather damped and unusual MLS trends seen in the Type-1 samples. The average I.P.E.'s of the pure

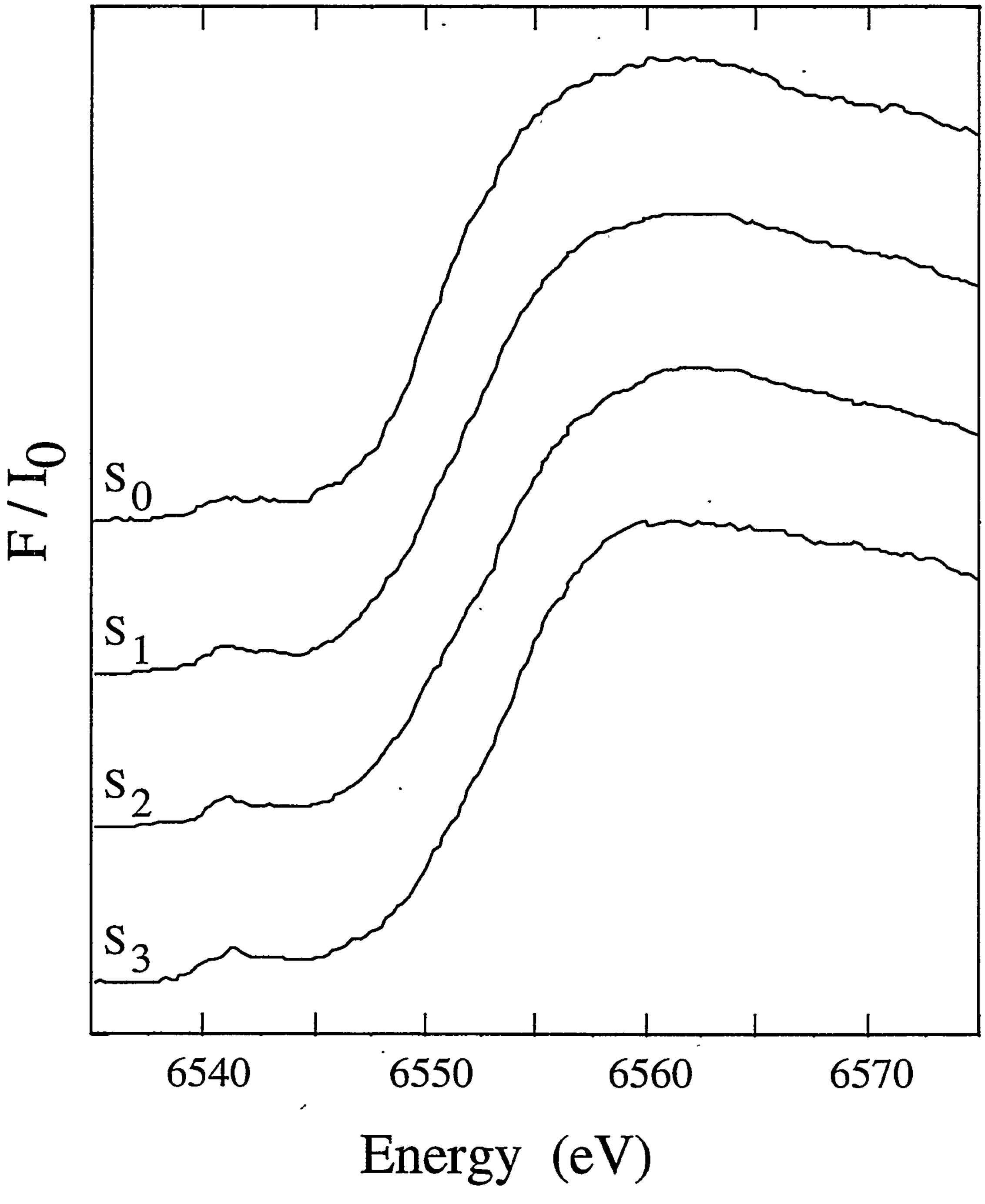

Fig. IV-4. Normalized Mn K-edge XANES spectra for the pure S-states of the Mn cluster of PSII, as computed from the flash-induced edge spectra of samples given 0-3 flashes. Shown are the averages of the S-state spectra extracted from three different groups of samples (Type-1_Xe, Type-1_Nd, and Type-2_Xe). Each group contains 2-4 sets of samples given 0-3 flashes. A linear scatter background is subtracted, and the spectra are normalized to unity at the energy of maximum absorption.

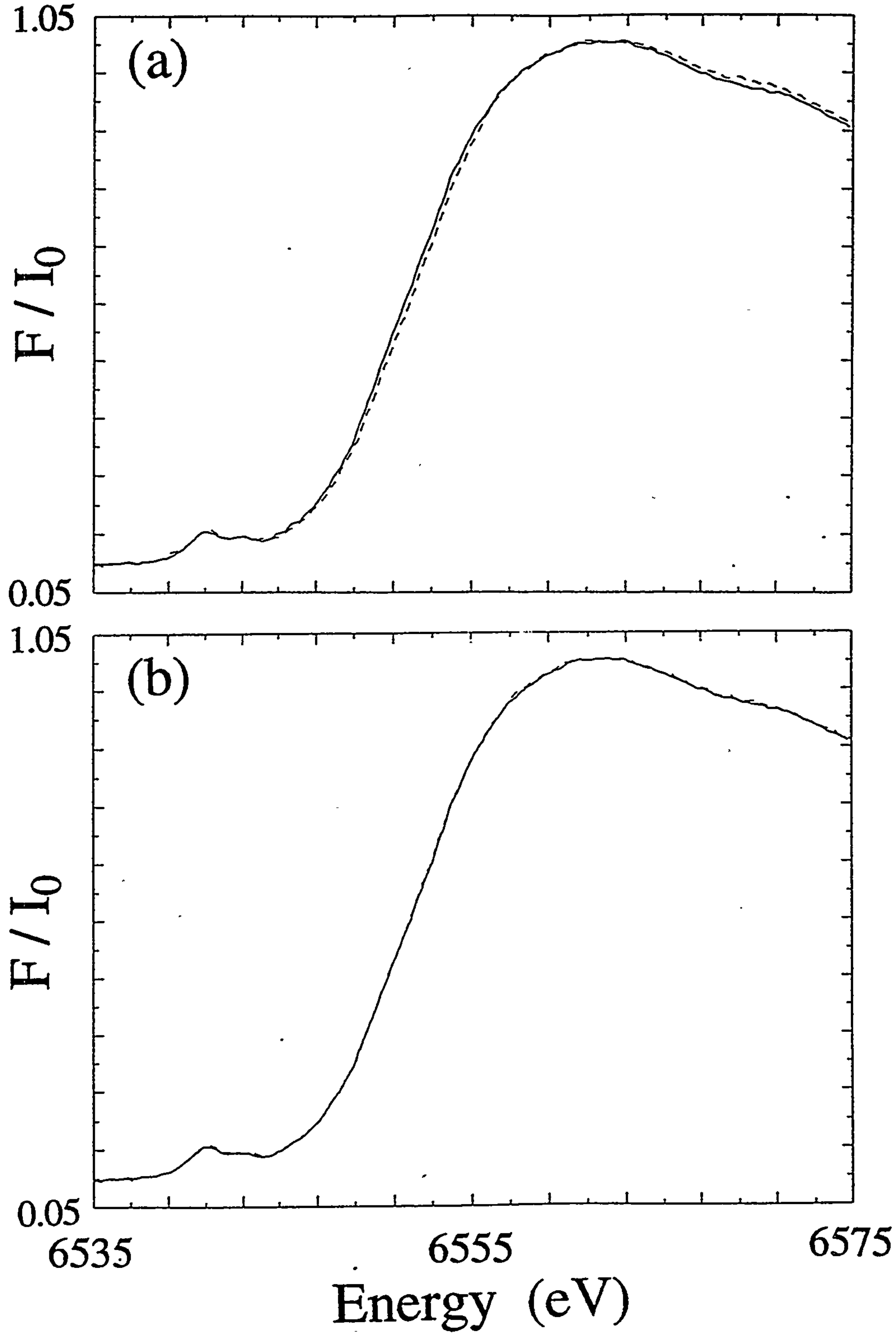

Fig. IV-5. Comparison of the simulated (----) and experimental (—) XANES spectra for (a) 4- and (b) 5-flash samples of the Type-1_Xe sample. See text for details.

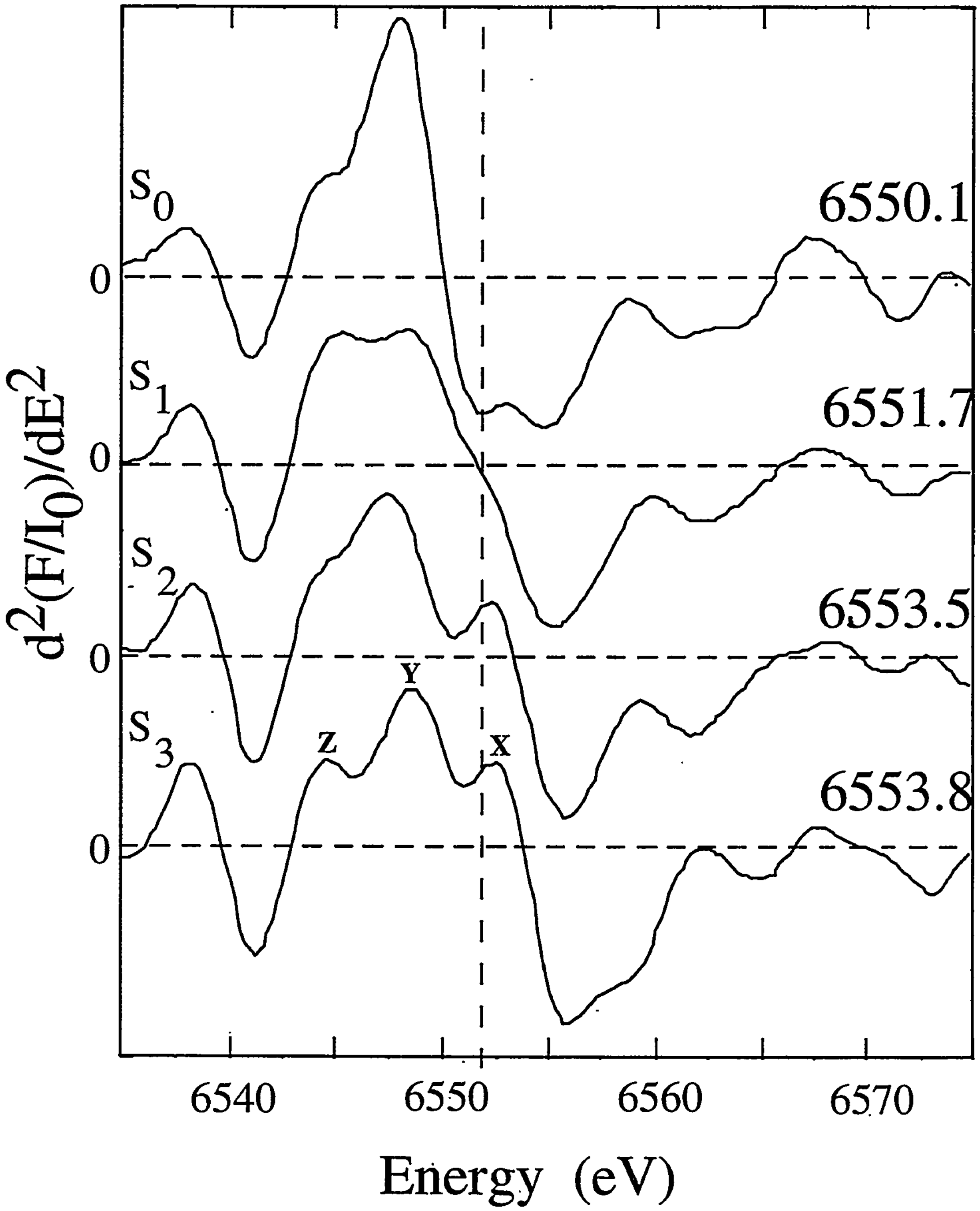

Fig. IV-6. Second derivatives of the averaged normalized pure S-state XANES spectra of the Mn cluster of PSII. For clarity a vertical dashed line is shown at the inflection point energy (I.P.E.) of the S_1 state. The numbers at the right are the I.P.E. in eV for each pure S-state.

Table IV-5. Inflection Point Energy (eV) for the Pure S-States of the Mn-Cluster, as Calculated from the Flash-Induced Edge Spectra.

Series	S_0	S_1	S_2	S_3
Type-1_Xe	6550.2	6552.0	6553.3	6553.9
Type-1_Nd	6549.9	6551.5	6553.7	6553.7
Type-2_Xe	6550.2	6551.7	6553.6	6553.9
Average	6550.1	6551.7	6553.5	6553.8

S_0, S_1, S_2, and S_3 states are 6550.1 eV, 6551.7 eV, 6553.5 eV and 6553.8 eV, respectively (Table IV-5 and Fig. IV-5). The positive shift of the edge position (1.8 eV) clearly supports Mn oxidation during the $S_1 \rightarrow S_2$ transition. Again, there is only a 0.3 eV edge-shift from the S_2 to S_3 state. This small shift suggests that there is likely no Mn oxidation occuring during the $S_2 \rightarrow S_3$ transition.

Due to a much improved signal-to-noise ratio in our Mn fluorescence detection, our XANES data are of sufficient quality to reveal clear feature changes in the pre-edge region among these pure S-states (Fig. IV-7). These pre-edge peaks occur at ~10 eV below the midpoint of the absorption edge. The absorption results from semiallowed 1*s* → 3*d* transitions, which are formally unallowed by dipole selection rules. These transitions generally become allowed when mixing occurs between 3*d* and 4*p* orbitals. Therefore, they are expected to yield information about the oxidation state and symmetry of the Mn complex. The overall shape of the pre-edge feature in the S_0 state is relatively broader and shorter than those of the other S-states. A shoulder at ~6543 eV appears during the $S_1 \rightarrow S_2$ transition, together with decrease of the intensity at the region marked with arrows. This feature disappears when the S_2 advances to the S_3 state, and the intensity of the region marked with arrows rises again. In addition, another shoulder at lower energy (~6538.5) also rises upon the formation of the S_3 state.

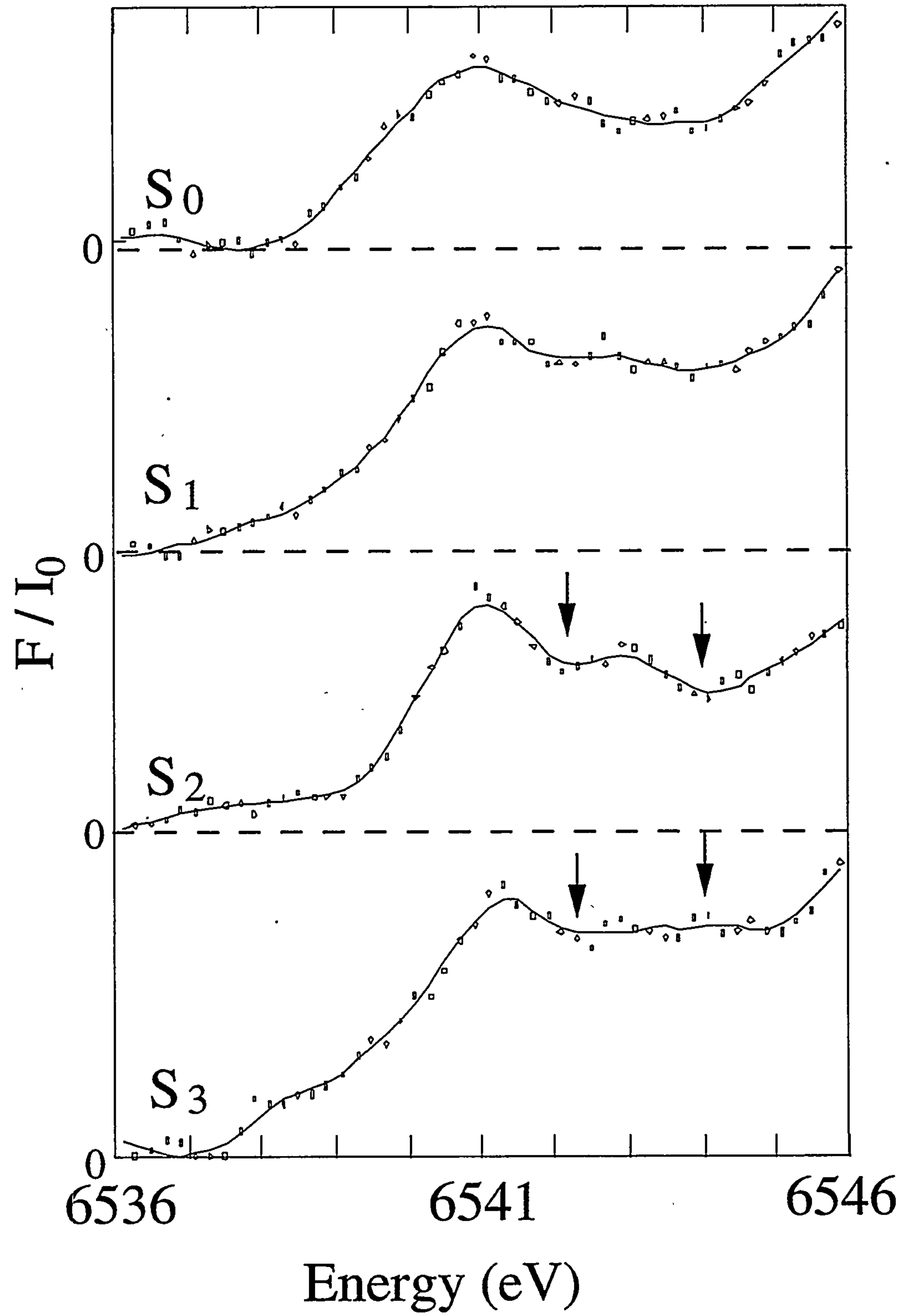

Fig. IV-7. The pre-edge feature of the pure S-states. Shown are the raw data points and a minimumly smoothed curve (solid line). Each spectrum is normalized to the maximum of the edge.

IV. D. Discussion.

IV. D. 1. The Redox State Assignment of the Mn Complex.

IV. D. 1. 1. The S_3 and S_0 States.

The S_3 state. The current XANES results from flash-induced S-state PSII samples indicate a very small edge shift during the $S_2 \rightarrow S_3$ transition. We conclude that, like those of the previous study on the S_3* state (Guiles et al., 1990b), these results do not support Mn oxidation during the $S_2 \rightarrow S_3$ transition. This conclusion is further supported by the following XANES results obtained from a series of Mn model compounds.

(1) A systematic study of the K-edges of synthetic Mn compounds (with N or O ligands) has been performed (Sauer et al., 1992). Among the many sets of bi-, tri, and tetranuclear Mn complexes with similar ligands and coordination environment, no single instance is found when a change in oxidation state of Mn is not accompanied by a 1-2 eV K-edge shift (Sauer et al., 1992). The small edge shift (0.3 eV) in the $S_2 \rightarrow S_3$ transition observed in the present work is only 17% corresponding to that of the $S_1 \rightarrow S_2$ transition. Therefore, the K-edge results from Mn model compounds further support the conclusion that no Mn oxidation occurs upon the formation of the S_3 state.

(2) The inflection point energy has been shown to be more sensitive to the bridging structure, rather than to the changes in the terminal ligands, after a careful comparison among multinuclear Mn complexes in similar oxidation states but with different coordination environments (Sauer et al., 1992). In several $Mn_2(III,IV)(\mu_2\text{-}O)_2$ compounds, the K-edge inflection point shifts by 0.4-0.6 eV on replacing a di-μ-oxo bridge with a mono-μ-oxo and μ-acetate bridges, with no change in the oxidation

state of the complex. Such ligand changes in the bridging position uniformly result in an increase in the Mn-Mn distance from 2.7 Å to ≥3 Å. The 0.3 eV edge shift observed in the $S_2 \rightarrow S_3$ transition from our samples may result from a similar effect . In the protein environment in which amino acid residues replace organic ligands, the extent of this effect could be modified (DeRose, 1990). In other words, a slightly smaller shift (0.3 eV) compared with that found in synthetic model compounds (0.4-0.6 eV) could result from a smaller increase of the Mn-Mn distance in the OEC, possibly due to a more constrained amino acid ligand environment on formation of the S_3 state. In fact, our preliminary S_3 EXAFS analyses show a much larger increased heterogeneity in the second shell (Mn--Mn) relative to that of the the S_2-g4 state (See Chapter III).

(3) In addition to the K-edge, the pre-edge region of a series of synthetic Mn(III) or Mn(IV) complexes with various nuclearity has also been studied (Sauer et al., 1988). In Mn(IV) complexes, the amplitudes of the pre-edge peaks are generally more pronounced relative to the trough (marked with arrows) in the region at higher energy just below the main peak, than the corresponding Mn(III) pre-edge amplitudes. However, in current work such an effect is not observed. Therefore, the pre-edge XANES results are consistent with the conclusion that no Mn oxidation during the $S_2 \rightarrow S_3$ transition.

The S_0 states. The current XANES results on the S_0 state are consistent with the earlier assignment (for the S_0* state) that one Mn(II) is present in the Mn cluster. This assignment also agrees with results from EPR and NMR relaxation measurements (Styring & Rutherford, 1988; Srinivasan & Sharp, 1986a,b).

IV. D. 1. 2. The Assignment of the Valence State in the Mn Complex.

The current study on the native S-state PSII samples prepared under physiological conditions confirms our earlier assignment of the Mn valence states in OEC. In the previous report, the valence states of the Mn complex were deduced after detailed analyses and comparison of the XANES and EXAFS spectra from the PSII (S_0*, S_1, S_2, S_3*) samples and a series of Mn model compounds (reviewed in Sauer et al., 1992). Our conclusion about the oxidation states of the Mn complex in the OEC at S_0-S_3 states are as follows:

S_0	II,III,IV,IV
S_1	III,III,IV,IV
S_2	III,IV,IV,IV
S_3	III,IV,IV,IV

The oxidation states of the S_3 and S_0 states shown above are in conflict with those published by Ono and coworkers (Ono et al., 1992), in which they reported that (a) a greater edge shift occurs during the $S_2 \rightarrow S_3$ transition (1.2 eV) than that of the $S_1 \rightarrow S_2$ transition (0.8 eV); and (b) the valence state of S_0 is (III,III,III,IV). The reason for this discrepancy is unclear at this stage. However, a comparison of the experiments performed between these two laboratories reveals several differences. Factors which may contribute to this disagreement are listed as follows:

(1) Samples. A small volume of PSII suspension (~15 µL, 4mg/mL) is mounted on a membrane filter in Ono's laboratory. By contrast, we use two types of sample cells (~50-120 µL) filled with PSII suspension with concentrations ranging from 4-6 mg/mL (higher concentration for smaller-volume of sample holders, see Chapter II). The signal-to-noise ratio in our samples is better. In addition, all of the S-state samples prepared in our laboratory are routinely examined and characterized

by EPR before and after the XAS experiments. So far, except the oxygen-yield measurement, MLS measurement is the most straightforward and reliable approach to characterize the S-state composition, and to monitor the quality of the PSII-enriched membranes. However, no EPR spectra have been reported from the samples prepared in Ono's group. Their samples have been characterized by the method of thermoluminecence (personal communication with Dr. T. Ono), but no thermoluminecence spectra have been reported either. Moreover, the complicated procedures required to deconvolute the thermoluminescence spectra to quantitate the composition of each S-state make this technique less reliable than the EPR (MLS) measurements (personal communication with Dr. A. W. Rutherford).

(2) Data collection. During data acquisition at the beamlines, the samples from Ono's group are kept under vacuum at a temperature of 80 K. The possible outcomes of partial lyophilization and orientation in the samples cannot be ignored. Partial orientation present in PSII samples could result in changes in edge positions and structures (Mukerji et al., 1994). This is because Mn absorption is anisotropic; the angle between the sample normal and the X-ray beam becomes important for oriented samples. In addition, lyophilization could cause some impairment in the S-state advance, as well as changes in the S-state composition as shown by Kawamoto and Asada (1990). In their study, lyophilized PSII membranes showed only 70% of the activity of oxygen evolution of the control PSII membranes. In addition, the OEC was reduced to "S_{-2}" state by lyophilization. Our samples, on the other hand, are kept in a He gas flow cryostat under atmospheric pressure at 10K. The PSII samples are reasonably stable at this condition. The EPR measurements after the X-ray experiments show that typically ≥ 80% of the MLS still maintains in our samples which have been exposed to the X-ray beam for 12-16 h.

(3) Data analyses. We use the I.P.E. to define the edge energies of the S-states. On the other hand, Ono's group reports the half-heights. As discussed above (Section IV.C.4.), improperly choosing the initial (0% edge) and final (100% edge) points may lead to incorrect results when half-heights are selected to represent the edge positions. This possibility is expected to be greater especially in samples with poor signal-to-noise ratio, as shown in the report (Ono et al., 1992). However, we believe that this factor is not the major contribution to the disagreement of the Mn valence state in the S_3 state. The half-heights measured from our S-state samples show hardly any shift (~0.1 eV) during the $S_2 \rightarrow S_3$ transition. For the $S_1 \rightarrow S_2$ transition, however, the edge shifts 1.1 eV upward.

IV. D. 2. What Is Oxidized During the $S_2 \rightarrow S_3$ Transition?

The current results indicate that upon the S_3-state formation, the oxidative equivalent stabilized on the donor side of PSII is stored on a redox active species other than the Mn cluster. To explain the disappearance of the MLS after this advance, a strong exchange interaction between the redox active species and the Mn cluster is postulated. The resulting spin system, with a value of the net spin equal to zero or an interger number (non-Kramers state), is hence EPR silent. To achieve this effect, the redox active species is necessary to reside close to the Mn cluster. This is because the magnitude of this exchange coupling decays rapidly as a function of the distance between paramagnetic centers (Coffman & Buettner, 1979). The redox active species could be either another intermediate donor or ligand(s) of the Mn complex.

Early in 1988, the Klein/Sauer group proposed aromatic ligands (histidine or tyrosine) to serve as the redox active species (Guiles, 1988). A scheme including a redox active species was further constructed to model the electron transfer during the

$S_2 \rightarrow S_3$ transition (Guiles, 1988). In the scheme, histidine was chosen to be the redox active species because the more basic side chain of histidine was thought to better facilitate the water oxidation and the formation of the peroxy bridge in the following water splittig step.

The recently discovered "S_3-state" EPR signal arising from treated PSII preparations supports the idea that a redox active species other than the Mn cluster becomes oxidized during the $S_2 \rightarrow S_3$ transition. These 13-16 mT-wide EPR signals are observed from Ca^{2+}-depleted (Boussac, et al., 1990; Tso et al., 1991; Hallahan et al., 1992), Cl^--depleted (Baumgarten et al., 1990; Boussac et al., 1992) and F^--inhibited (Baumgarten et al., 1990) PSII preparations which do not evolve oxygen. From now on I will refer to this EPR signal as the "S_3-type" EPR signal, because there are currently two assignments which are still under dispute (See below).

The identity of the species which generates this "S_3-type" EPR signal is obviously of great interest. One suggestion is that the "S_3-type" EPR signal is attributable to a modified "S_3" state (Boussac, et al., 1990; Baumgarten et al., 1990; Boussac et al., 1992). In this proposal, this EPR signal is thought to arise from an organic free-radical, on the basis of the spectral features and the microwave power saturation characteristics (Boussac et al., 1989). This free radical interacts magnetically with a faster relaxing paramagnet--the Mn complex--and therefore results in loss of the MLS upon the S_3 formation. By comparing the UV absorption spectra obtained from the modified "S_3" state and oxidized histidine, Boussac and coworkers conclude that histidine probably undergoes oxidation in the $S_2 \rightarrow S_3$ transition of the inhibited enzyme (Boussac et al., 1990)

The second interpretation for the "S_3-type" EPR signal is that this signal arises from the $S_2Y_Z^+$ state, which Hallahan and coworkers designate the "S_2-plus-radical" state (Hallahan et al., 1992). Their results show that the Y_Z^+ signal is formed under conditions which also generate the "S_3-type" EPR signal in Ca^{2+}-depleted PSII preparations. Hallahan and coworkers propose that a variety of treatments which affect calcium and chloride binding cause a stabilization of the S_2 state, and slow the reduction of Y_Z^+. Under this condition Y_Z^+ is trapped and is able to interact with the Mn cluster (probably) in the S_2 state; this finally results in the "S_3-type" EPR signal. Along with this interpretation, the real EPR signal in the S_3 state from untreated (functional) PSII preparations is thought to be EPR silent.

If we assume that the "S_3-type" EPR signal arises from histidine radical, an important question is whether histidine is oxidized in uninhibited PSII preparations upon $S_2 \rightarrow S_3$ transition. Electron spin echo envelope modulation (ESEEM) experiments have proven the presence of nitrogen coupling to the Mn (DeRose et al., 1991). A recent result further demonstrates that histidine is bound to the Mn cluster in the OEC (Tang et al., 1994). These ESEEM results support the conclusion that histidine is still oxidized in the functional PSII preparations during the $S_2 \rightarrow S_3$ transition. However, because the nature and magnitude of the magnetic interaction between the inhibited and functional PSII preparations are different, the S_3-EPR signal in the functional PSII membranes may become too broad to be detected.

IV. E. Conclusion.

The XAS technique has been applied to study the XANES from flash-induced S-state samples prepared under physiological conditions. The conclusions are summarized as follows:

(1) The pre-flash treatment oxidizes almost all of the reduced Y_D in the PSII

samples and synchronizes the PSII centers to $S_1Y_D^+$ state before a series of flashes start. This treatment greatly decreases the possibility of recombination between the S_2 and S_3 states with reduced Y_D. The PPBQ treatment further stabilizes the S_2 and S_3 states on a time scale of min (3.4-4 min) at room temperature.

(2) Type-1 (BBY-type, with a 30-min detergent extraction procedure during the PSII purification) PSII membranes may contain a impaired Q_B site and therefore result in much damped MLS trends as a function of flash number. An extended Kok model is necessary to model the MLS oscillations in Type-1 samples. In this model, the traditional miss parameter (α) is modified to be a time-dependent parameter. On the other hand, Type-2 membranes (KM-type, with a two-minute detergent extraction step) display normal MLS oscillation curves. The traditional Kok model is suitable to describe Type-2 samples. The best fits show that parameter β (double hits) is zero when a Nd-YAG laser is used as the flash source.

(3) The pure S-state XANES spectra obtained from both types of PSII preparations give similar inflection point energies and edge shapes. These results confirm that the extended Kok model is a reasonable approach to model the Type-1 samples.

(4) The energy of the Mn K-edge shifts only 0.3 eV upon the $S_2 \rightarrow S_3$ transition. This result confirms those of the previous XAS study on the S_3* state (Guiles et al., 1990b). Again the XANES results imply that no Mn oxidation occurs upon formation of the S_3 state. In addition, the pre-edge region shows similar peak amplitude between the S_2 and S_3 states. A detailed comparison with a series of Mn(III) and Mn(IV) synthetic compounds does not support the presence of Mn(IV) formation upon the $S_2 \rightarrow S_3$ transition.

(5) The oxidative equivalent stored on the donor side of the PSII during the $S_2 \rightarrow S_3$ transition may be stored in a histidine which ligates to the Mn cluster. This is supported by the results of the ESEEM studies on functional PSII samples, and by UV absorption spectroscopic results on inhibited PSII membranes. However, the other possible redox active species, tyrosine, cannot be ruled out at this point.

IV.F. Reference.

Babcock, G. T., & Sauer, K. (1973) *Biochim. Biophys. Acta 325,* 483

Baumgarten, M., Philo, J. S. & Dismukes, G. C. (1990) *Biochemistry 29*, 10814

Beck, W. F. & Brudvig, G. W. (1986) *Biochemistry 25*, 6479

Boussac, A., Maison-Peteri, B., Vernotte, C. & Étienne, A.-L. (1985) *Biochim. Biophys. Acta 808,* 225

Boussac, A., Zimmermann, J.-L. & Rutherford, A. W. (1989) *Biochemistry 28,* 8984

Boussac, A., Zimmermann, J.-L., Rutherford, A. W. & Lavergne, J. (1990) *Nature 347*, 303

Boussac, A., Sétif, P. & Rutherford, A. W. (1992) *Biochemistry 31*, 1224

Bowes, J. M. & Crofts, A. R. (1980) *Biochim. Biophys. Acta 590,* 373

Brudvig, G. W., Casey, J. L. & Sauer, K. (1983) *Biochim. Biophys. Acta 723,* 366

Coffman, R. E., & Buettner, G. R. (1979) *J. Phys. Chem. 83*, 2387

Crofts, A. R. & Wraight, C. A. (1983) *Biochim. Biophys. Acta 726,* 149

DeRose, V. J, Yachandra, V. K., McDermott, A. E., Britt, R. D. (1991) *Biochemistry 30*, 1335

DeRose, V. J. (1990) Ph.D. Thesis, University of California, Berkeley. Lawrence Berkeley Laboratory Report: LBL-30077

Dismukes, G. C., & Siderer, Y. (1981) *Proc. Natl. Acad. Sci. U.S.A. 78*, 274

Forbush, B., Kok, B. & McGloin, M. P. (1971) *Photochem. Photobiol. 14*, 307

Guiles, R. D., Yachandra, V. K., McDermott, A. E., Cole, J. L., Dexheimer, S. L., Britt, R. D., Sauer, K., & Klein, M. P. (1990a) *Biochemistry 29*, 486

Guiles, R. D., Zimmermann, J.-L., McDermott, A. E., Yachandra, V. K., Cole, J. L., Dexheimer, S. L., Britt, R. D., Wieghardt, K., Bossek, U., Sauer, K., & Klein, M. P. (1990b) *Biochemistry 29*, 471

Guiles, R. D. (1988) Ph.D. Thesis, University of California, Berkeley.

Lawrence Berkeley Laboratory Report: LBL-25186

Hallahan, B. J., Nugent, J. H. A., Warden, J. T. & Evans, M. C. W. (1992) *Biochemistry 31*, 4562

Joliot, P. Barbieri, G. & Chabaud, R. (1969) *Photochem. Photobiol. 10*, 309

Joliot, P. & Kok, B. (1975) in *Oxygen Evolution in Photosynthesis.* (Govindjee, ed.), pp. 387-412, Academic Press, New York.

Kawamoto, K. & Asada, K. (1990) in *Current Research in Photosynthesis, Vol. I,* (Baltscheffsky, M. ed.), pp. 889-892, Kluwer Academic Publishers, Netherlands.

Kok, B., Forbush, B. & McGloin, M. (1970) *Photochem. Photobiol. 11*, 457

Kusunoki, M., Ono, T., Noguchi, T., Inoue, Y. & Oyanagi, H. (1993) *Photosynthesis Research 38*,331

Lavergne, J. & Étienne, A.-L. (1981) in *Photosynthesis III* (Akoyunoglou, G., ed.), pp. 939-948, Balaban International Science Services, Philadelphia, PA.

Lozier, R. H., & Butler, W. L. (1973) *Photochem. Photobiol. 17*, 133

Messinger, J., Schröder & Renger, G. (1993) *Biochemistry 32*, 7658

Mukerji, I., Andrews, J. C., DeRose, V. J., Latimer, M. J., Yachandra, V. K., Sauer, K. & Klein, M. P. (1994) *Biochemistry 33*, 9712

Ono, T.-A., Noguchi, T., Inoue, Y., Kusunoki, M., Matsushita, T. & Oyanagi, H. (1992) *Science 258*, 1335

Petrouleas, V. & Diner, B. A. (1987) *Biochim. Biophys. Acta 893* , 126

Robinson, H. H. & Crofts, A. R. (1983) *FEBS Lett. 153,* 221

Roe, A. L., Schneider, D. J., Mayer, R. J., Pyrz, J. W., Widom, J. & Que, L. (1984) *J. Am. Chem. Soc. 106*, 1676

Rutherford, A. W., Crofts, A. R. & Inoue, Y. (1982) *Biochim. Biophys. Acta 682,* 457

Rutherford, A. W., Govindjee & Inoue, Y. (1984) *Proc. Natl. Acad. Sci. USA 81,* 1107

Sauer, K., Guiles, R. D., McDermott, A. E., Cole, J. L., Yachandra, V. K., Zimmermann, J.-L., Klein, M. P., Dexheimer, S. L. & Britt, R. D. (1988) *Chemica Scripta 28A*, 87

Sauer, K., Yachandra, V. K., Britt, R. D., & Klein, M. P. (1992) in *Manganese Redox Enzymes* (Pecoraro, V. L., Ed.) pp. 141-175, VCH Publishers, New York.

Srinivasan, A. N. & Sharp, R. R. (1986a) *Biochim. Biophys. Acta 850,* 211

Srinivasan, A. N. & Sharp, R. R. (1986b) *Biochim. Biophys. Acta 851,* 329

Styring, S. & Rutherford, A. W. (1987) *Biochemistry* 26, 2401

Styring, S. & Rutherford, A. W. (1988) *Biochemistry* 27, 4915

Tang, X. S., Diner, B. A., Larsen, B. S., Gilchrist, M. L., Lorigan, G. A. & Britt, R. D. (1994) *Proc. Natl. Acad. Sci. 91*, 704

Tso, J., Sivaraja, M. & Dismukes, G. C. (1991) *Biochemistry 30*, 4734

Vass, I. & Styring, S. (1991) *Biochemistry 30*, 830

Velthuys, B. R., & Visser, J. W. M. (1975) *FEBS Lett. 55*, 109

Vermaas, W. E. J., Renger, G., & Dohnt, G. (1984) *Biochim. Biophys. Acta 764*, 194

Weiss, C., Kenneth, J., Solnit, T., & Von Gutfeld, R. J. (1971) *Biochim. Biophys. Acta 253*, 298

Yachandra, V. K., DeRose, V. J., Latimer, M. J., Mukerji, I., Sauer, K., & Klein, M. P. (1993) *Science 260*, 675

Zimmermann, J.-L., & Rutherford, A. W. (1986) *Biochemistry 25* , 4609

Chapter V. Conclusions and Future Work.

V. A. Summary.

This thesis is part of the research to which our group has been devoted for more than a decade. The overall objective of this research is to understand the detailed process of how the OEC in plants and cyanobacteria stores oxidative equivalents during the S-state transitions, and to elucidate eventually the mechanism for water splitting. The more immediate goals of our research are to reveal the structure of the Mn cluster in OEC. Knowledge of the Mn structure is obviously required for us to further resolve the mechanism of water oxidation. A summary of the structural information of the Mn cluster obtained from the previous chapters will be described in this section.

V. A. 1. The Strucural Correlation between the Two S_2 States.

The first question I set out to answer was: what are the structural correlations between the two EPR signals (the MLS and $g \approx 4.1$) from the S_2 state? Previous EXAFS and XANES studies on the dark-adapted S_1 and cryogenically trapped S_2 states lead us to the conclusion that the overall structure of these two states are very similar. On the basis of the model we proposed (Fig. I-4), this conclusion means that for both the S_1 and S_2 states, the Mn-Mn distance in the two di-μ-oxo bridged dimers is approximately the same (~2.7 Å), and the Mn-Mn distance between these two dimers is ~3.3 Å (Yachandra et al., 1993). According to these results, we would expect the structure of the S_2-g4 state also to be similar to that of the S_1 and S_2 states. However, the outcome is rather surprising.

The structure of the S_2-g4 samples is distinct from that of the S_1 and S_2 states. One of the di-μ-oxo bridged dimers is perturbed, and the Mn-Mn distance increases from 2.72 Å to 2.85 Å. By a comparison with the results from synthetic, multinuclear Mn model coumpounds, this 0.13 Å increase of distance can be correlated to the oxidation of one Mn(III) to Mn(IV) in the Mn cluster of OEC (Wieghardt, 1989). The unexpected results lead to another question. Because both the S_2-MLS and S_2-g4 states arise from an one-electron oxidation of Mn(III) to Mn(IV) upon the $S_1 \rightarrow S_2$ transition, then, why does the S_2-MLS state not have an elongated Mn-Mn distance in one of its Mn dimers?

A model has been proposed to reply to this question as well as to account for these two types of S_2 EPR signals (Fig.III-8). In this model, a temperature- and ligand-dependent structural change is assumed to occur between the S_2-g4 and S_2-MLS samples. The g≈4 signal arises from a "trapped" S_2-g4 state after illuminating the S_1 samples at 140 K, a temperature which is assumed to be too low for a structural change of the Mn cluster to occur. However, by raising the illumination temperature to 200 K for the $S_1 \rightarrow S_2$ transition, the Mn cluster is then allowed to undergo a structural rearrangement. The resulting S_2-MLS state has a Mn-Mn distance of ~2.7 Å for both of the di-μ-oxo Mn dimers. Along with this temperature-dependent structural rearrangement, a (proposed) critical ligand site occupied by an OH^-/H_2O ligand in the S_2-g4 state is replaced by a Cl^- ligand in the S_2-MLS state.

This model is reasonable in three aspects. First, it explains the recovery of the MLS at the expense of the g≈4 signal when the S_2-g4 samples are annealed at 200 K in the dark. Second, the involvement of ligand exchanges (between OH^-/H_2O and Cl^-) in this model explains the possible cause of structural changes to produce these two EPR signals. That is, the modification of the molecular arrangement due to an exchange of a critical ligand to Mn atoms is enough to modulate the exchange coupling and further to vary the ground spin state of the Mn cluster in the OEC. This assumption is reasonable because the S_2-MLS and S_2-g4 signals are thought to arise from different spin state, based on previous EPR studies (Britt et al., 1989; Haddy et al., 1992). The MLS originates from the $S=1/2$ ground state, while the g≈4 signal is thought to arise from the middle Kramers doublet of a near rhombic S=5/2 state. Moreover, as seen from the studies of inorganic compounds, changes as small as protonation of the bridging oxygen are effective in switching the Mn compound from antiferromagnetic to ferromagnetic (Hagen et al., 1989).

Third, this model is reasonable because, in addition to this native S_2-g4 samples, PSII preparations treated with ammonia or fluoride also display a longer distance in one of the Mn-Mn dimers (Dau et al., submitted; DeRose et al., submitted). Both ammonia and fluoride are known to compete with a chloride binding site (Yocum, 1992). Cl^- is required for the formation of the MLS, as observed in experiments of Cl^--depleted S_2-g4 samples where the g≈4 signal was replaced by the MLS upon adding Cl^- in the dark at 0° C (Ono et al., 1986). Thererfore, a Cl^- ligand occupying the critical ligand site is a reasonable assumption for this model.

V. A. 2. The Valence States of the Mn Cluster in Different S-States.

The second important question is: what are the oxidation states of the Mn cluster in each S-state? From here more related questions arise: when samples are prepared under physiological conditions, are the results similar to those prepared at the cryogenic temperature? Also is the Mn complex the sole site to accumulate the oxidizing equivalents in the Kok scheme?

The most straightforward way to prepare all of the different S-state samples is to use saturating, single-turnover flashes. The main problem for XAS experiments on flash-induced S-states is because the XAS technique is concentration-limited. In other words, to saturate all of the PSII reaction centers, the chlorophyll concentration needs to be dilute. As a consequence, the Mn concentration is approximately an order of magnitude more dilute than the normal concentration (~1mM) used for XAS. However, now it is possible to work with this dilute samples using the recently developed 13-element Ge detector. Even though the XAS measurements on the native (flash-induced) S-states were not available, our group used special protocols to prepare PSII samples in the S_0* and S_3* states which are generated by low-temperature continuous illumination (Guiles et al., 1990a,b).

The results of these studies are summarized below. For the $S_0^* \rightarrow S_1$ transition, the edge shifts upward with a value of ~1 eV, and both of the XANES and EXAFS of the S_0^* sample support a Mn(II) present in the S_0* state. The small magnitude of the edge energy shift from $S_2 \rightarrow S_3^*$ is unexpected, because both the XANES and EXAFS results show no Mn oxidation during this transition. This implies that the Mn cluster is not the sole site to accumulate oxidative equivalents during the S-state advance! Several alternative redox active species have been proposed; among them are amino acid ligands including histidine and tyrosine (Guiles, 1988). In addition, UV absorption results for a modified "S_3" state from Ca^{2+}-depleted PSII preparations support the conclusion that a histidine oxidizes in the modified S_3 state. Recent ESEEM evidence of a histidine ligating to the Mn cluster further supports the possibility that histidine is the alternative oxidative species during the $S_2 \rightarrow S_3$ advance.

We decided to apply XAS to flash-induced S-states to test whether Mn becomes oxidized during the $S_2 \rightarrow S_3$ transition in native samples prepared under physiological conditions. We started with the BBY-type of PSII preparations which included a 30-min detergent extraction step in the protocol (denoted Type-1 in Chapter IV.). Type-1 samples displayed damped MLS oscillation trends, and were later presumed to have an impaired Q_B site possibly due to a long exposure time with the detergent. An extended Kok model which incorporated a time-dependent miss parameter and a traditional double hit (β) successfully described these MLS trends. A second type of PSII preparation named the KM-protocol was also used because of its much shorter detergent step (Type-2 samples in Chapter IV.). Type-2 samples, as expected, displayed much bigger MLS oscillation`` which could be described by the traditional Kok model with conventional parameters α and β.

Although the MLS trends and subsequently the S-state composition after each flash are different between Type-1 and Type-2 samples, the pure S-state XANES spectra constructed from both types of samples are surprisingly similar. This similarity further verifies the use of the extended Kok model for Type-1 samples. The inflection point energies, the pre-edge feature, and the second derivatives obtained from both types of samples, with good reproducibility and signal-to-noise ratio, do not support the conclusion that Mn oxidation occurs in the $S_2 \rightarrow S_3$ transition. The distinct shape of the second derivative XANES spectra in the S_0 state supports a Mn(II) present in this state. The XANES results from the native S-states confirm those obtained from the S_0* and S_3* states.

V. B. Suggested Future Directions.

V. B. 1. Orientation Study of the S_2-g4 State.

The first part of this thesis is directed to obtain structural information about the S_2-g4 state of the Mn cluster. The model we proposed for the S_2-g4 state can be further extended by applying the XAS technique to examine oriented S_2-g4 samples.

More information about the angles between specific absorber-backscatterer vectors and the membrane normal can be obtained by applying the XAS technique to oriented samples. If several internuclear distances are identical, only an "average angle" can be determined, as can be seen in the studies on the native S_1 and S_2 states (George et al., 1989; George et al., 1993; Mukerji et al., 1994). In the native S_1 and S_2 states, the two components of the 2.72 Å vector are oriented at an average angle of 60 ± 7° to the membrane normal. The average angle of the 3.3 Å vector is 43 ± 10° with respect to the membrane normal (Mukerji et al., 1994).

However, due to the distance heterogeneity in the second shell (arising from the two Mn-Mn vectors in the di-μ-oxo bridged dimanganese unit, see Fig. III-8), the two Mn-Mn vectors at 2.72 Å and 2.85 Å become distinguishable in the oriented S_2-g4 samples. In other words, the orientation of each vector with respective to the membrane normal can be uniquely determined. The resulting information can be used to refine the geometrical arrangement of the model in Fig. III-8. This knowledge will then be useful to deduce the possible pathway during the structural changes between the S_2-MLS and S_2-g4 states.

In addition, the non-unique fitting results of the third shell (~3.3 A) in the S_2-g4 samples may also be clarified if one of the sub-shells is oriented in a preferred angle relative to the other sub-shell. If this is the case, we can magnify and examine one vector at a particular orientation, where the second vector contributes much less. Similarly the second vector can be studied at another orientation where the first one is less preferred.

In fact, the oriented ammonia-treated PSII samples have been studied by this technique. The ammonia-treated PSII membranes also show an increased heterogeneity in the second shell. The angles between the membrane normal and the Mn-Mn vectors are determined to be 55 ± 4° and 67 ± 3°, for the two sub-shells with Mn-Mn distance of 2.72 Å and 2.87 Å, respectively (Dau et al., submitted).

V. B. 2. EXAFS Study on the Flash-Induced S-States.

A series of critical questions remain. Where, when, and how does water-splitting happen? None of these questions can be answered without a detailed understanding of the structure of the Mn cluster in each of the S-states. To extend our knowledge for the structure of the Mn cluster, a logical approach is to study the flash-induced S_0 and S_3 states by the EXAFS technique.

Several results from independent spectroscopic studies on the $S_2 \rightarrow S_3$ transition have revealed that the Mn cluster may not be the only site to accumulate the oxidative equivalents in the Kok cycle (See Chapter I and results in Chapter IV). The reason for this is not understood. The S_3 state is currently the closest state to water splitting, because so far the transient S_4 state has not been trapped. Presumably the S_3 state is where the OEC starts to prepare for water splitting, perhaps by formation of a peroxo group by two water molecules. On the other hand, the S_0 state is the state immediately after oxygen evolution. Hence, the S_0 state is at a stage that is just recovering from a presumably big structural change due to oxygen evolving. A detailed EXAFS analysis on these S-states will shed some light on the changes of ligand environment and the arrangement within the Mn cluster during the water splitting step.

The assignment of a Mn(II) present in the S_0* state is supported by both the XANES and EXAFS studies on the PSII samples. The EXAFS results show that there is a significant change in the structure of the complex during the S_0* to S_1 transition (Sauer et al., 1992). The second derivative K-edge spectra of the flash-induced, native

S_0 state in the current study also supports the presence of Mn(II) (See Chapter IV). This assignment will be further verified by the EXAFS analyses.

Experiments are already in progress to collect the EXAFS from the S_0 and S_3 states. A comparison of these spectra to those of the S_1 and S_2 states should address some of the questions mentioned above.

V. B. 3. Parallel Polarization EPR Study of the S_3 state.

The current results indicate that, upon the S_3-state formation, the oxidative equivalent stabilized on the donor side of PSII is stored on a redox active species other than the Mn cluster. To explain the disappearance of the MLS after this advance, a strong exchange interaction between the redox active species and the Mn cluster is assumed to result in a spin system with a net spin value equal to zero or an interger number (non-Kramers state). The resulting spin system is silent to conventional EPR detection (perpendicular mode).

An alternative method to detect this non-Kramers spin system is to apply an unconventional EPR technique--parallel polarization EPR--to the S_3 state. This technique is sensitive to formally forbidden transitions in high spin states, and therefore is suitable to pursue possible signals in the S_3 state. The parallel polarization EPR technique has been applied to detect PSII samples poised at the S_1 state, which is also EPR silent in the conventional perpendicular mode (Dexheimer & Klein, 1992). A new EPR signal is detected in the S_1 state by this method, and the property of this signal is consistent with an $S=1$ spin state of an exchange-coupled Mn cluster that corresponds to the reduced form of that at the S_2-MLS state.

V. B. 4. Characterization of the Pre-Edge Features in the S-States.

To serve as models for non-heme iron proteins, a distinctive pre-edge feature in the K-edge spectra of a series of high-spin ferric complexes has been studied (Roe et al., 1984). The results indicate that the intensity of this feature varies inversely with the coordination number. Within the group of the same coordination number, the peak intensity tends to increase as the complex becomes more distorted or has lower symmetry. The pre-edge information has aided in the interpretation of the EXAFS for non-heme iron protein systems including iron-transferrin-carbonate and thioglycolate complexes (Roe et al., 1984)

As mentioned in Chapter IV, our current XANES are of sufficient quality to reveal clear feature changes in the pre-edge region of the S-states. The pre-edge region of a series of synthetic Mn(III) or Mn(IV) complexes with various nuclearity (monomers to trimers) has been studied (Sauer et al., 1988). A comparison between these synthetic model compounds and the PSII preparations from spinach or *Synechococcus* at the pre-edge region showed that some features of the S_1 and S_2 state spectra can be associated with Mn(III) or Mn(IV), respectively. However, due to a limited choice of synthetic Mn complexes available at that time, there was insufficient information to carry out as detailed an analysis as had been done for the iron complexes. Since then, many Mn complexes have been synthesized. Therefore, a systematic re-examination of all of the inorganic Mn complexes (as suggested by Dr. V. Yachandra) is necessary before the pre-edge features in the Mn cluster of OEC (or other Mn-containing protein systems) can be further interpreted. Knowledge of the Mn pre-edge feature will definitely provide a powerful tool to examine the symmetry and oxidation state of the various S-states.

V. C. References.

Britt, R. D., Zimmermann, J.-L., Sauer, K. & Klein, M. P. (1989) *J. Am. Chem. Soc. 111*, 3522

Dexheimer, S. L. & Klein, M. P. (1992) *J. Am. Chem. Soc. 114*, 2821

George, G. N., Prince, R. C. & Cramer, S. P. (1989) *Science 243*, 789

George, G. N., Cramer, S. P., Frey, T. G., & Prince, R. C. (1993) *Biochim. Biophys. Acta 1142*, 240

Guiles, R. D., Yachandra, V. K., McDermott, A. E., Cole, J. L., Dexheimer, S. L., Britt, R. D., Sauer, K., & Klein, M. P. (1990a) *Biochemistry 29*, 486

Guiles, R. D., Zimmermann, J.-L., McDermott, A. E., Yachandra, V. K., Cole, J. L., Dexheimer, S. L., Britt, R. D., Wieghardt, K., Bossek, U., Sauer, K., & Klein, M. P. (1990b) *Biochemistry 29*, 471

Guiles, R. D. (1988) Ph.D. Thesis, University of California, Berkeley. Lawrence Berkeley Laboratory Report: LBL-25186

Haddy, A., Dunham, W. R., Sands, R. H. & Aasa, R. (1992) *Biochim. Biophys. Acta 1099*, 25

Mukerji, I., Andrews, J. C., DeRose, V. J., Latimer, M. J., Yachandra, V. K., Sauer, K. & Klein, M. P. (1994) *Biochemistry 33*, 9712

Ono, T.-A, Zimmermann, J.-L., Inoue, Y., & Rutherford, A. W. (1986) *Biochim. Biophys. Acta 851*, 193

Roe, A. L., Schneider, D. J., Mayer, R. J., Pyrz, J. W., Widom, J. & Que, L. (1984) *J. Am. Chem. Soc. 106*, 1676

Sauer, K., Guiles, R. D., McDermott, A. E., Cole, J. L., Yachandra, V. K., Zimmermann, J.-L., Klein, M. P., Dexheimer, S. L. & Britt, R. D. (1988) *Chemica Scripta 28A*, 87

Wieghardt, K. (1989) *Angew. Chem. Int. Ed. Engl. 28*, 1153

Yachandra, V. K., DeRose, V. J., Latimer, M. J., Mukerji, I., Sauer, K., & Klein, M. P. (1993) *Science 260*, 675

Yocum, C. F. (1992) in *Manganese Redox Enzymes* (Pecoraro, V. L., Ed.) pp. 71-83, VCH Publishers, New York.